DEVELOPMENT AND APPLICATION OF ELECTRON SPIN RESONANCE (ESR) SPECTROSCOPY TO STUDY INTERACTIONS IN BIOMEMBRANES

A Dissertation

Presented to the Faculty of the Graduate School

of Cornell University

In Partial Fulfillment of the Requirements for the Degree of

Doctor of Philosophy

by

Siddarth Chandrasekaran

August 2017

DEVELOPMENT AND APPLICATION OF ELECTRON SPIN RESONANCE (ESR) SPECTROSCOPY TO STUDY INTERACTIONS IN BIOMEMBRANES

Siddarth Chandrasekaran, Ph. D.

Cornell University 2017

Electron Spin Resonance (ESR) spectroscopy has been extensively used to study membrane dynamics and structure. ESR has been shown to be sensitive to a wide range of molecular motions (10^5 to 10^{12} s^{-1}). The use of multi-frequency ESR has helped analyze the complex modes of motions typically observed for spin probes attached to biomolecules. Further, the use of pulsed two dimensional ESR techniques (e.g. 2D-ELDOR) has increased the sensitivity to detect molecular motions and has helped to better resolve spectral features. The use of 2D-ELDOR at high frequencies has been particularly challenging due to relatively short dead times required (T_2 minimum ~4 ns). We have developed a 95 GHz high power spectrometer which can be operated at room temperatures to study 'lossy" aqueous samples. We have used this technique to study the partitioning of TEMPO into DMPC. We show that 95 GHz 2D-ELDOR can resolve the spectra of TEMPO in water and the lipid phase. Further, for the first time, we have observed the exchange dynamics of TEMPO between these phases and estimate it to have an exchange rate of 0.5 μs^{-1}. We have then used multi-frequency ESR to study the formation of nanoscopic, co-existing L_o & L_d domains in ternary lipid mixtures. We find that formation of nanodomains does not affect the phase behavior, but indicates the presence of a transition "boundary" region that has intermediate order between the L_o & L_d domains. We further observe that crosslinking of biotinylated gramicidin in these nanodomains, affects the phase behavior by reducing the ordering in the system, but

does not change the phase behavior in the macrodomain region. We have also studied the effect of cholesterol depletion in plasma membrane vesicles obtained from RBL cells, and observe that this increases the fraction of the L_d phase in the system. Finally we have used pulsed dipolar ESR to study the crosslinked aggregates of IgE, and have determined that inter IgE-IgE distances to be about 3 - 4 nm. All these results show the ability of ESR to address a wide range of questions related to membrane biophysics.

BIOGRAPHICAL SKETCH

Siddarth Chandrasekaran was born in April, 1988 at Hyderabad, India. As a child, he was inspired by his mom, a chemist in one of India's premier national labs, to pursue the search for knowledge. He completed his undergraduate degree in chemistry at Loyola College (University of Madras), India in 2008. At Loyola, he and his friends discussed chemistry at length over many a cups of tea; it is here that he discovered a passion for research in chemistry. In 2008, he was awarded the Erasmus Mundus fellowship to pursue a Master's degree in "Advanced Spectroscopy in Chemistry". He chose to spend a year at the University of Lille-1, France and a year at the University of Leipzig, Germany. His master's thesis titled "Fourier Transform time-resolved EPR study of the radical intermediates formed during the photo oxidation of valine and histidine" was carried out in the lab of Prof. Bernd Abel (Leipzig, Germany). At Lille, he was first exposed to EPR spectroscopy in the lab of Hervé Vezin and was greatly excited by the prospects of being an EPR spectroscopist. This led him to seek out an internship in the lab of Prof. Jack Freed at Cornell in the summer of 2009. He later returned to Cornell in Fall 2010 to carry out his PhD on the development and application of ESR to study biomembranes under the supervision of Prof. Jack H. Freed. In addition to his academic pursuits, Siddarth has been involved in multiple student leadership roles throughout his collegiate career. He also has enjoyed teaching many different courses at Cornell and was a fellow at the Cornell Center for Teaching Excellence.

TO THE MANY INSPIRATIONS IN MY LIFE

And

FOR THE PURSUIT OF KNOWLEDGE

ACKNOWLEDGMENTS

I would like to thank Prof. Jack H. Freed for all his support and guidance throughout my graduate career at Cornell. He provided vital feedback at critical junctures of the PhD program. His knowledge and scientific vision is truly inspirational and has helped me develop a better understanding of the field of magnetic resonance spectroscopy. In his group, I have experienced the many flavors of inter-disciplinary research from organic synthesis to biochemistry to theory to ESR instrumentation. In the Freed group, I am also grateful to Dr. Boris Dzikovski for his mentorship through the course of the graduate program. Boris was present to answer any or all silly questions I had about the field of membrane biophysics. Boris has also provided deep insights about sample preparation, data collection and processing that has made my life as a PhD student a lot easier.

I would like to thank Prof. Jerry Feigenson and Prof. Barbara Baird for being supportive committee members and wonderful collaborators. They have provided valuable input to my projects and my dissertation. I have enjoyed working with individuals of both their groups (especially Dr. Dave Holowka). Further, I would like to thank Prof. Brian Crane for being a valuable mentor and helping me deal with many a difficult situation. I would like to also thank Prof. Greg Ezra for being a great teacher; he was very instrumental in helping me become more comfortable with the language of physical chemistry. He has also inspired me to be a better teacher and communicator.

I thank the very many members of the Freed group, past and present, who have aided with the ESR measurements and sample preparation. In particular, I am thankful to Curt Dunnam and Dr. John Franck for all the help with all the high field ESR measurements. John was greatly helpful in developing the right type of data analysis methods for 2D-ESR. I thank Dr. Petr Borbat for the PDS measurements and Madhur Srivastava for

performing the wavelet denoising. I would like to thank the other members – Dr. Jozef Moscicki, Dr. Keith Earle, Dr. Zhichun Liang for all the help with instrumentation and simulation of the 95 GHz spectra. I would like to thank Aritro Sinha Roy for all his support in settling down in the Freed group and for being a big brother figure in the group. I thank Dr. Alex Lai, Dr. Timothee Chauvire, and Dr. Galina Petkova for their help and friendship. I would also like to thank my favorite "undergrad" Shu Wang for being a wonderful coworker and helping with the nanodomains project in collaboration with Prof. Feigenson's lab. I thank Binoy Jhaveri for assistance with the biotinylated gramicidin synthesis and sample preparation for this project. I also thank Joanne Trutko and Art Samplanski of the Freed group for all the administrative support over the years. I would also like to thank Pat Hine and all the chemistry administrative staff who made the entire graduate school experience pleasurable.

This PhD would not have been possible without the support of my many friends at Cornell and Ithaca. From my peers in the department, I am thankful of Devin, Dan, Dipanjan and Luke for making the chemistry experience memorable. I would like to thank Poornima, Madhur, Aritro, Aadhar, Ravi, Sriram, Sreejith, Sanket, Mehreen, Aravind, Sri Nivas, Aman, Sachin, Skand, Gourab (Master), Prashanth for their friendship and joyous times playing many board and card games. These board games kept me sane and grounded through the course of my PhD. A special thank you to Anoop, who spent a lot of his free time teaching me all the mathematical tools I needed, I will be forever indebted to him for this. Finally, I would like to thank my family (mom, dad, brother, grandparents) who have always supported me in all my pursuits. Last but not the least, I would like to thank Nidhi (a fellow Cornelian), my wife and best friend, who has made my graduate school experience even more enjoyable.

TABLE OF CONTENTS

LIST OF FIGURES

LIST OF TABLES

LIST OF ABBREVIATIONS

16PC	1-Palmitoyl-2-stearoyl-(16-doxyl)-sn-glycero-3-phosphocholine
BBS	Borate buffered saline
bis-MTS-P	3,4-Bis-(methanethiosulfonylmethyl)-2,2,5,5-tetramethyl-2,5-dihydro-1H-pyrrol-1-yloxy radical
cw	Continuous wave, typical usage is cw-ESR
DOPC	1,2-Dioleoyl-sn-glycero-3-phosphocholine
DSPC	1,2-Distearoyl-sn-glycero-3-phosphocholine
ELDOR	Electron-electron double resonance
ESR	Electron spin resonance spectroscopy
FcεRI	Transmembrane receptor for the Fc region of immunoglobulin E
HB	Homogeneous broadening
IB	Inhomogeneous broadening
IgE	Immunoglobulin E
MOMD	Microscopic Order with Macroscopic Disorder Model
PBS	Phosphate buffered saline
PDS	Pulsed Dipolar Spectroscopy
POPC	1-Palmitoyl-2-oleoyl-sn-glycero-3-phosphocholine
SECSY	Spin-echo correlation spectroscopy
SLE	Stochastic Louiville Equation
SRLS	Slowly Relaxing Local Structure Model

CHAPTER 1 : INTRODUCTION

Electron Spin resonance (ESR) spectroscopy is a magnetic resonance technique that is used to probe electronic spin states. Generally, in the absence of an external magnetic field these spin states are degenerate, while in the presence of a magnetic field this spin state degeneracy is removed and we observe energy level splitting. This difference in energy levels between spin states is directly dependent on the magnetic field applied and is given by the following expression for a free electron, $\Delta E = h\nu = g_e\beta_e B_0$, g_e is the g-factor of the electron, βe is the Bohr magneton and B_0 is the magnitude of the external magnetic field applied. A majority of the molecules in nature are diamagnetic and are not ESR active, this is advantageous as ESR spectra have little background signal. ESR spectroscopy is optimal to study unpaired electrons in radicals or metal ions. In this dissertation, we will focus only on free radicals belonging to the nitroxide family that are derivatives of the ESR spin label molecule – TEMPO (2,2,6,6-Tetramethylpiperidin-1-yl) oxyl. ESR has been extensively used to study the structure and dynamics of biomolecules such as proteins, DNA and lipids.[1]The first and major part of this chapter will focus on the application of ESR to study molecular motions in biomembranes, while the second part will briefly introduce the application of pulsed dipolar spectroscopy to study structure in biological systems.

1.1. ESR and Molecular Motions

ESR is extremely sensitive to a wide range of molecular motions as shown in Figure 1-1. To understand this let us observe the spin Hamiltonian ($\widehat{H}(t)$), which can be separated into the following components[2]

$$\widehat{H}(t) = \widehat{H_0} + \widehat{H_1}(\Omega) + \hat{\epsilon}(t) \qquad \text{1-I}$$

where H_0 is the orientation independent part that includes the electronic and nuclear Zeeman terms and the electron-nuclear hyperfine interaction. ε(t) is the radiation term that induces the ESR transitions. The orientation dependent part is expressed as

$$\widehat{H_1}(\Omega) = \sum_{l,m,m',\mu} \hat{A}^{(l.m)}_{\mu,LF}\, \mathfrak{D}^{l}_{m,m'}(\Omega_{LM})\, F^{(l,m')^*}_{\mu,MF} \qquad \text{1-II}$$

Where $\hat{A}^{(l.m)}_{\mu,LF}$ are the irreducible components of the spin tensors defined in the lab frame, $\mathfrak{D}^{l}_{m,m'}(\Omega_{LM})$ are the Wigner rotation elements that transform the matrix elements between the molecular frame and the lab frame, and $F^{(l,m')^*}_{\mu,MF}$ are the irreducible tensor coefficients of the magnetic interactions (i.e, g-tensor or hyperfine tensor) that are defined in the molecular frame.

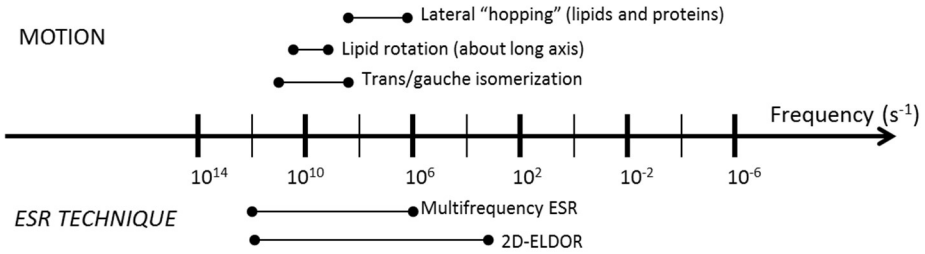

Figure 1-1: The motional rates accessed by ESR and the corresponding lipid motions. Figure is modified from Dzikovski et al.(2008)[3]

When the molecular motion is completely frozen, then we observe all the different orientations; this is called the rigid limit spectrum (or powder average spectrum). In the other extreme case, the fast motional limit, all the different orientations are spanned in the time scale of the measurement, so we observe an average of all of them; this leads to narrow ESR lines whose positions are defined by the isotropic g-factor (where $g_{iso} = \frac{(g_{xx}+g_{yy}+g_{zz})}{3}$) and A-tensor ($A_{iso} = \frac{(A_{xx}+A_{yy}+A_{zz})}{3}$) values. In the case of nitroxide probes like TEMPO, the g_{iso} values are around 2.0058-2.0062, representing an **N-O** centered radical.

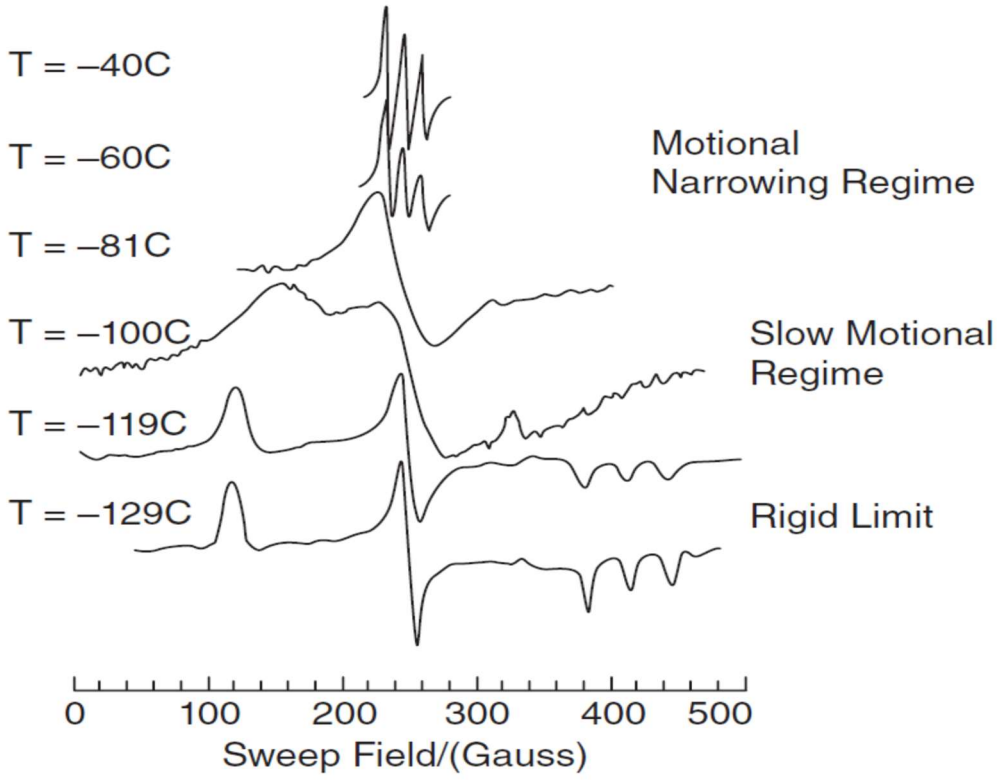

Figure 1-2: cw-ESR spectra of PD-TEMPONE in toluene (m.p.: -95℃) at 250 GHz at different temperatures. The spectra are motional narrowed at -40 ℃, - 60 ℃ as indicated by the three narrow lines and in the rigid limit at -119 ℃ and -129℃. Figure is modified from Misra et al. (2011)[4]

Both the rigid limit as well as the fast motional case are easiest to interpret. In reality, the most relevant molecular motion range for biomolecules is in the intermediate to slow motional limit where the spectral line shapes are extremely dependent on the rates of motion as well as the ordering in the system. Therefore, these slow motional spectra allow for the extraction of molecular dynamical parameters. The different motional regimes as well as the spectra can be seen in Figure 1-2.

1.1.1. Slow motions and the Stochastic Liouville Equation

The complex line shapes in the slow motional range are difficult to interpret and can be understood by solving the Stochastic Liouville equation (SLE). Freed and coworkers have first applied the SLE to calculate the ESR line shapes.[5] The SLE couples the quantum mechanical spin operator to the classical diffusion operator ($\boldsymbol{\Gamma_\Omega}$).

$$\frac{\partial \hat{\rho}(\Omega, t)}{\partial t} = -i\left[\hat{H}, \hat{\rho}(\Omega, t)\right] - \Gamma_\Omega \hat{\rho}(\Omega, t) \qquad \text{1-III}$$

where $\hat{\rho}\{\Omega, t)$ is the density operator that describes the sub-ensembles of spins at the orientation given by Euler angles (Ω). Note this representation of $\hat{\rho}$ contains the probability distribution, **P(Ω, t)**, for the orientation. The standard quantum spin density operator can be obtained by averaging over all the orientations, $\hat{\rho}(t) = \int \hat{\rho}(\Omega, t) d\Omega$, and the probability distribution for each orientation can be obtained by taking a trace over each orientation, $P(\Omega, t) = Tr[\hat{\rho}(\Omega, t)]$.[2,6]

1.1.2.SLE in Anisotropic media

The diffusion of spin probes attached to biomolecules such as proteins or lipids is typically anisotropic. In these cases, equilibrium distribution ($P_{eq}(\Omega)$) can be given by the orientational potential energy, U(Ω), such that

$$P_{eq}(\Omega) = \frac{e^{-\frac{U(\Omega)}{k_b T}}}{\int e^{-\frac{U(\Omega)}{k_b T}} d\Omega} \qquad \text{1-IV}$$

where k_B is the Boltzmann constant and T is the temperature. The diffusion operator then has the form:

$$\hat{\Gamma}_\Omega = \left[\nabla_\Omega - \frac{\nabla_\Omega}{k_b T}\right] \cdot \boldsymbol{R} \cdot \left[\nabla_\Omega - \frac{\nabla_\Omega}{k_b T}\right] \qquad \text{1-V}$$

This is the symmetrized form of the diffusion operator where R is the rotation diffusion tensor, with more details available in reference.[6] The orientational potential can be expressed as

$$U(\Omega) = -k_B T \sum_{L,K} c^L_{M,K} \mathfrak{D}^L_{MK}(\Omega) \qquad \text{1-VI}$$

Where $\mathfrak{D}^L_{MK}(\Omega)$ are the Wigner rotation elements and $c^L_{M,K}$ are the corresponding coefficients. The ordering in the system can then be expressed as

$$\boldsymbol{S_0} = \langle D^{(2)}_{0,0} \rangle = \langle \frac{1}{2}(3\cos^2\theta - 1) \rangle \quad \text{1-VII}$$

and

$$\boldsymbol{S_2} = \langle D^{(2)}_{0,2} + D^{(2)}_{0,-2} \rangle = \langle \sqrt{\frac{3}{2}} \sin^2\theta \; cos\; 2\phi \rangle \quad \text{1-VIII}$$

The description is still simplistic, as probes attached to biomolecules have complex motional modes. For the example of a spin label attached to a protein, we can describe the following motional modes: (1) the global tumbling of the protein in solution, (2) the side chain fluctuations of the residues around an average orientation, and (3) a rapid reorientation of the spin probe with respect to the sidechain (as typically the probes are attached to the proteins by a flexible linker). More details of protein dynamics have been reviewed by Liang and Freed.[7]

However, not all the modes can be completely separated; in most cases, we can only observe a composite of motions. In general, we can define global/director motion (macroscopic) and composite of internal motions (microscopic). If the macroscopic motion is very slow then it appears frozen out (or rigid), then we can define only the microscopic order & diffusion and average over all the random macroscopic orientations. This is known as the Microscopic Order Macroscopic Disorder (MOMD) model.[8] If there is slow reorientation or tumbling of the macroscopic system, then we can specifically introduce the global motion and calculate the ESR spectra using the Slowly Relaxing Local Structure (SRLS) model.[9]

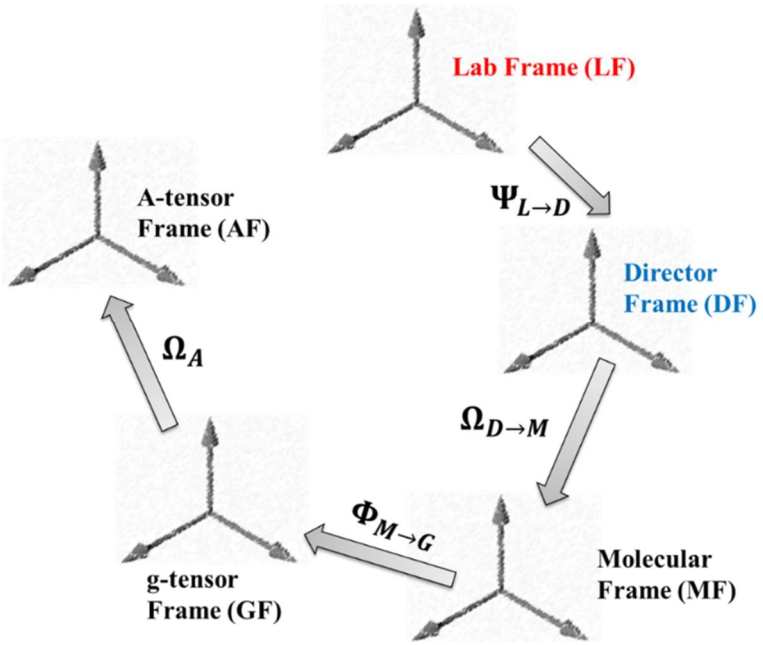

Figure 1-3: Different frames of reference used to study the dynamic and structural properties of our system. The molecular frame is fixed with respect to the molecule while the experiments are carried out in the lab frame.

This can be better understood in terms of the various frames of reference (Figure 1-3) for the experiment: (1) The Lab Frame (LF) is defined with respect to the external magnetic field i.e., the direction of the magnetic field is along the z-axis, (2) the director frame (DF), which is obtained from the LF by a set of transformation by the Euler Angles $\Psi_{L\to D}$, (3) the molecular frame (MF) is fixed with respect to the molecule and obtained by the transformation $\Omega_{D\to M}$. In MOMD, the $\Psi_{L\to D}$ Euler angles are "frozen," i.e., time-independent and usually randomly oriented. In SRLS, they are time-dependent due to the slower motion of the larger body.

For spin labeled lipid molecules, the reference frames can be defined as the following: (1) the laboratory frame (X_L, Y_L, Z_L), (2) the local director frame (X_d, Y_d, Z_d) representing the bilayer-orienting potential frame (Figure 1-4); (3) the molecular frame (X_R, Y_R, Z_R) in which the rotational diffusion tensor of the spin-label is diagonal; and (4) the

magnetic tensor frame (X_m, Y_m, Z_m) in which the g and hyperfine (A) tensors are diagonal (typically for nitroxide molecules, the principal axes for the g-tensor and A-tensor frames are almost parallel[6]). The rotation parameters obtained from the fit ($R_{\|}$ and $R_{\perp}$) are the principal values of an axially symmetric rotational diffusion tensor for the nitroxide molecule attached to the acyl chain of the lipid molecule. The order parameter, S_0 , is a measure of the alignment of the molecular axis (Z_R) with respect to the local director axis (Z_d), while S_2 is the extent of preferential alignment of the other molecular axis (X_R vs Y_R) with respect to the director axis (Z_d).[10]

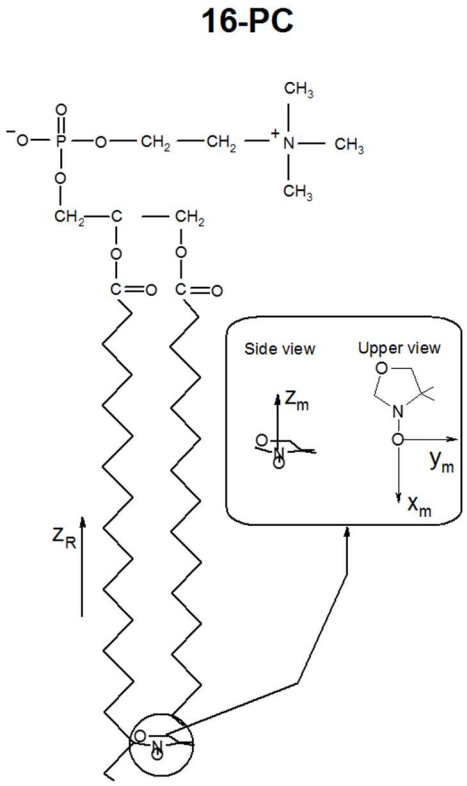

Figure 1-4: The orientation of the spin label in the lipid membranes along with the orientation of the molecular frame (Z_R). Figure is modified from Costa-Filho et al. (2003).[11]

1.1.2.1. Multifrequency study: Separating global motion from local motion

A multifrequency approach, using low and high frequency ESR (HF-ESR) is essential to achieve decomposition of the complex dynamic (global vs local) modes affecting the spin label at each site. High frequency ESR provides greater g-tensor resolution, because the electron spin Zeeman interaction term becomes dominant in the Hamiltonian at very high frequencies (~200 GHz); whereas, the A-tensor components can be more precisely measured from ESR spectra at low frequencies (~9 GHz). As the orientation-dependent part of the spin-Hamiltonian ($H_1(\Omega)$), c.f. Equation 1-II) increases in magnitude with increasing frequency, HF-ESR spectra appears to collect a "faster snapshot" of the dynamics. ESR at higher frequencies are therefore more sensitive to faster dynamics but loses sensitivity to slower motional dynamics, i.e., generally the slow overall tumbling (or global) motion is almost completely frozen out. While, low frequency ESR offers a "slower snapshot" of motion where the faster internal motions are partially or entirely averaged out. So low frequency ESR has increased sensitivity to the slower motional rates. Therefore, multifrequency ESR spectroscopy enables one to separate various motional modes in a biomolecule (protein/lipid) according to their time scales (Figure 1-5).

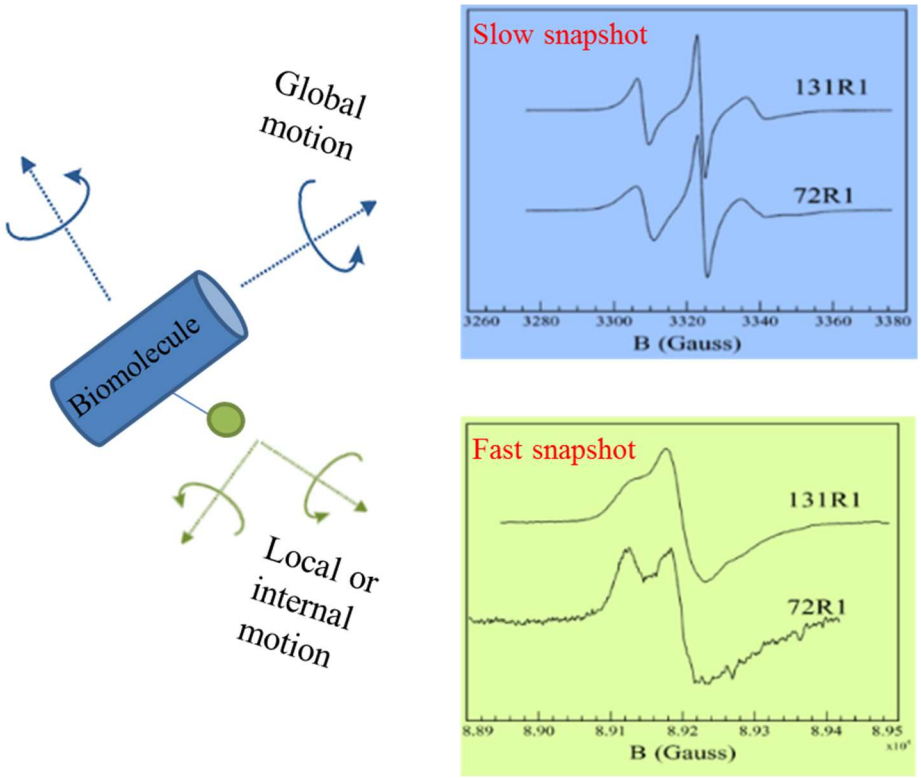

Figure 1-5: A schematic showing the ESR spectral change with frequency. 9 GHz Spectroscopy (top right) is sensitive to both global and local motion while 250 GHz Spectroscopy (bottom right) is only sensitive to the faster local motion (with the global motion is frozen out).[6,12,13]

For example, multifrequency ESR was used to understand the complex dynamics of T4 Lysozyme spin labeled at various residues.[14] In this study, cw-ESR spectra were measured at four different frequencies (9, 95, 170 and 240 GHz). At 240 GHz, the slow overall tumbling of the protein was completely frozen out and only sensitive to the fast internal modes. At 9 GHz, the ESR spectra were sensitive to the slow global dynamics. The SRLS model was used to simultaneously fit the multifrequency data to obtain both the global dynamics as well as the fast internal motions of spin-labeled T4-Lyzosyme. Lou and coworkers have also used two frequencies (9 & 250 GHz cw-ESR) to study the

dynamics of lipid membranes. This study also used the SRLS model to identify the rates of global motion.[15]

1.1.2.2. Two Dimensional Electron Spin Resonance

Pulsed ESR techniques especially two-dimensional techniques such as two-dimensional electron-electron resonance (2D-ELDOR) improves the spectral resolution by providing an additional spectral dimension. 2D-ELDOR studies decouple the homogeneous broadening (HB) from the inhomogeneous broadening (IB) thereby providing varied information in the different spectral dimensions. HB provides insight into molecular motions while IB provides information about the local structure and ordering. 2D-ELDOR spectra also contain cross-peaks that reports on the translational diffusion of the spin probes, nuclear spin relaxation, as well as exchange processes.[6] The specifics of the 2D-ELDOR technique are covered in Chapter 2.

1.2. Membranes: Phase Behavior and ESR

1.2.1. Membrane Phase Behavior

Cell membranes, made up of lipid and protein molecules, act as a hydrophobic barrier (~30Å) that protects the cell. One of the functions of the cell membrane is to act as a semipermeable barrier that can selectively allow/transport specific ions and organic molecules (addressed further in Chapter 2). In addition to this, the cell membrane has many other physiological roles such as signaling and adhesion (addressed in Chapters 4

and 5). To achieve this varied functionality and specificity it is vital for the cell membrane to have a high level of organization. Singer and Nicholson, first proposed the fluid mosaic model (1972) for the organization of the cell.[16] This model describes the membrane as a two dimensional mosaic containing lipids, proteins and other components (e.g. carbohydrates, cholesterol), where all the components have fluid-like mobility. This enhanced mobility of the lipid membrane allows the membrane components to interact with each other. This model even though relatively simple explains a large number of membrane functions. However other studies suggested that protein and lipid motions are restricted to smaller sub regions or domains (popularly referred to as rafts) of the cell membrane, leading to the conclusion that the membrane is compartmentalized.[17] Numerous studies have now shown the presence of coexisting liquid ordered (L_o) and liquid disordered (L_d) domains in cell membranes.[18–23] However questions remain about the size and stability of these domains. The current understanding is that these domains are submicroscopic (or nanoscopic). Further, it is still not clear if these domains are in thermodynamic equilibrium or in a kinetic non-equilibrium phase.[24–27]

Table 1-1: The translational diffusion rates and the order parameter for the different phases [3]

Phase	**Translational Diffusion (D_T)**	**Order Parameters (S*)**
Liquid Disordered (L_d) or crystalline (L_α)	10^{-8} cm^2/s	0.0-0.2
Liquid Ordered (L_o)	10^{-8} cm^2/s	0.2-0.9
Gel (P_β, L_β)	10^{-11} cm^2/s	0.2-0.9

**measured by NMR*

The nature and composition of these ordered and disordered domains are quite different. Both these phases have similar fluidity (i.e., translational diffusion rates) but the L_o phase has significantly higher order than the disordered phase (c.f. Table 1-1). The lipid constituents of these phases are also different; the ordered phase generally has higher amounts of high melting lipids (e.g. sphingolipids) and cholesterol while the disordered phase is made up of predominantly low melting lipids. Cholesterol plays a major role in the formation of an ordered phase, as it occupies the space between two phosphocholine or sphingomyelin molecules.[28] The effect of cholesterol depletion on membrane phase behavior is discussed further in Chapter 4. Figure 1-6 below shows the different phases and their corresponding motion/order parameters. The gel phase (L_β), which is not generally found in natural biological membranes, has significantly slower motional rates and higher order.

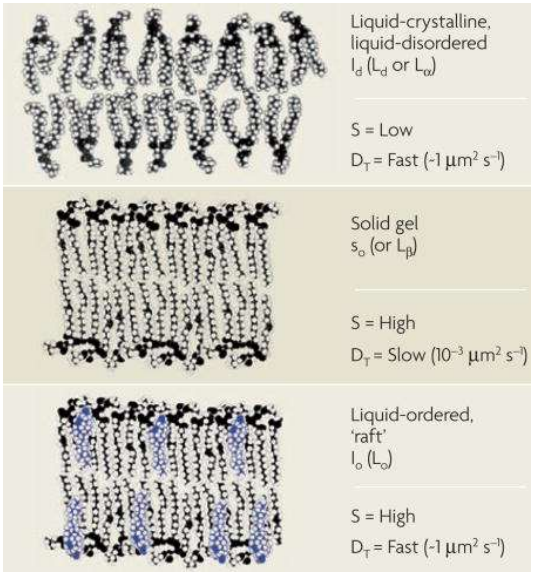

Figure 1-6: The different phases in the lipid membranes and their associated motional/order parameters. Figure is modified from van Meer et al. (2008)[29]

Natural membranes have more than 1000 lipid constituents and consist of two leaflets, (i) the inner (towards the cytoplasm) and (ii) the outer (exposed to the cell exterior) leaflet. Natural membranes are asymmetric with the outer leaflets richer in phosphatidylcholines (PC), cholesterol (Chol) and sphingolipids while the inner leaflets consist mainly of phosphatidylethanolamine (PE), phosphatidylserine (PS) and phosphatidylinositol (PI).[29] These natural membranes are extremely complex and therefore difficult to study. This has led to the development of model systems made up of select lipid and protein constituents where the specific phase behavior (of the membrane) can be carefully controlled to exhibit phase behavior to similar natural membranes. This allows for developing studies for looking at specific interactions, such as the phase behavior changes due to lipid-lipid and lipid-protein interactions. It is important to note that a large number of model membrane studies have focused on using symmetric bilayers, as these are relatively easy to prepare.

As mentioned earlier, high melting lipids and cholesterol prefer the ordered phase while the low melting lipids prefer the disordered phase. This allows for development of a model membrane system consisting of three classes of lipid, (a) high melting (high T_m) lipid, (b) low melting (low T_m) lipid, and (c) cholesterol. Figure 1-7 shows the phase diagram for one such system, DPPC/DLPC/Chol, where DPPC is high melting lipid while DLPC is the low melting lipid. Recent studies have extended it to study the phase behavior of ternary lipid mixtures and is discussed further in Chapter 3.

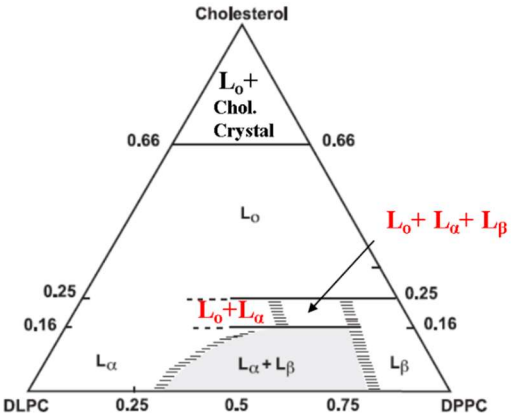

Figure 1-7: Ternary phase diagram for DPPC/DLPC/Chol at 24 ℃. [10,30] *L_α corresponds to the L_d phase and L_β corresponds to the gel phase. High DLPC concentration and low cholesterol concentration (bottom left), the L_α phase is observed while high DPPC and cholesterol concentrations the L_o phase is observed. Figure is modified from Feigenson et al. (2001)*[30].

1.2.1.1. Protein and Lipid interactions in the Membrane

The interactions of lipids with proteins have been of major interest for the biomedical community as it plays a vital role in many cellular functions.[31–34] Two major types of proteins interact with cellular membranes: (a) peripheral and (b) integral membrane proteins. The peripheral membrane proteins interact only temporarily with the cell membranes. Typically, these proteins are bound to the polar head groups of the lipid molecules and/or interact with the integral membrane proteins. Integral membrane proteins (IMP) are directly embedded in the lipid membrane such that their hydrophobic residues are buried in the lipid bilayer. IMP's like FcεRI (discussed further in Chapter 4) act as surface receptors for cellular signaling processes. Although much is known about the lipid phase behavior, few studies address the interface of lipids and proteins especially the role of boundary lipids (in close proximity to the proteins) versus the bulk

lipids.[33,35] Further, the effect of protein-protein interactions leading to changes in membrane phase behavior are also poorly understood.

1.2.2. ESR studies

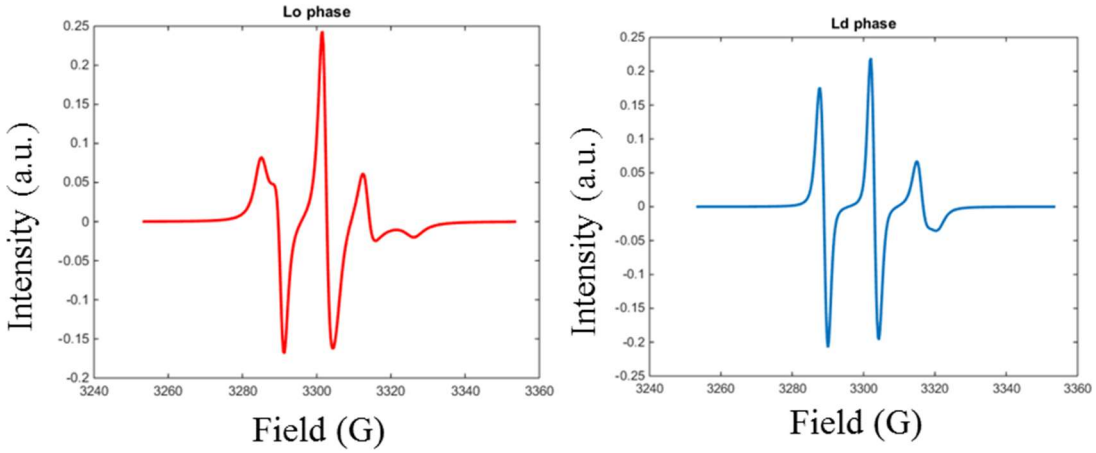

Figure 1-8: The cw-ESR spectra of 16-PC in the L_o phase (left) and the L_d phase (right) observed at 9 GHz. This shows the sensitivity of low frequency ESR to distinguish between these two phases.

Electron spin resonance (ESR) spectroscopy is an important technique to probe membrane phase behavior.[1,3,6,36–39] ESR offers unique insights into membrane behavior, as the timescale of spin labeled ESR is comparable to the lipid diffusion rate in fluid lipid bilayers[3] (c.f. Figure 1-1). Further, ESR is sensitive to the extent of ordering in the membrane. Figure 1-8 shows the differences in the L_o and L_d spectra as observed by 9 GHz cw-ESR. The differences in L_o and L_d spectra are better resolved at higher frequencies (also addressed in Chapter 3) and using 2D-ELDOR spectroscopy (Figure 1-9).[39,40] ESR typically utilizes spin labeled lipids that are membrane constituent phospholipids labeled at different positions with a small nitroxide moiety. These spin

labels (e.g. 5-PC, 16-PC, cholestane) can help monitor membrane properties at different immersion depths.

Model membranes have been studied extensively using both multifrequency cw-ESR as well as two-dimensional ESR spectroscopy. These studies have helped elucidate the hydration and the molecular interaction in the cell membranes.[41] Further, the permeability of small molecules (oxygen[42,43] and other small molecules[44,45]), polarity profiles,[46,47] electrostatics and membrane-ion interactions[48,49] have also been observed. ESR studies on ternary lipid mixtures have also helped understand the phase behavior of coexisting L_o and L_d domains and have been a vital step in making these model membrane studies more physiologically relevant.[10,19,50–52] The importance of cholesterol in the formation of the liquid ordered phase has also been studied.[11,28] Cw-ESR[53,54] as well as 2D-ELDOR[33] spectroscopy have been used to characterize the boundary lipids in the near vicinity of the transmembrane peptide, gramicidin A′ (GA). It has been shown that these boundary lipids have greater order and slower motional rates than the bulk lipids. Further, ESR has been used to probe the interactions of fusion peptides with cell membranes. These studies showed that the membrane ordering increased throughout the membrane due to the fusion process. Furthermore, this ordering was dependent on the cholesterol concentration with greater ordering effects seen in cholesterol rich membrane.[55,56] The ordering effects on a membrane is enhanced when the fusion peptides interact with the viral transmembrane domain.[57]

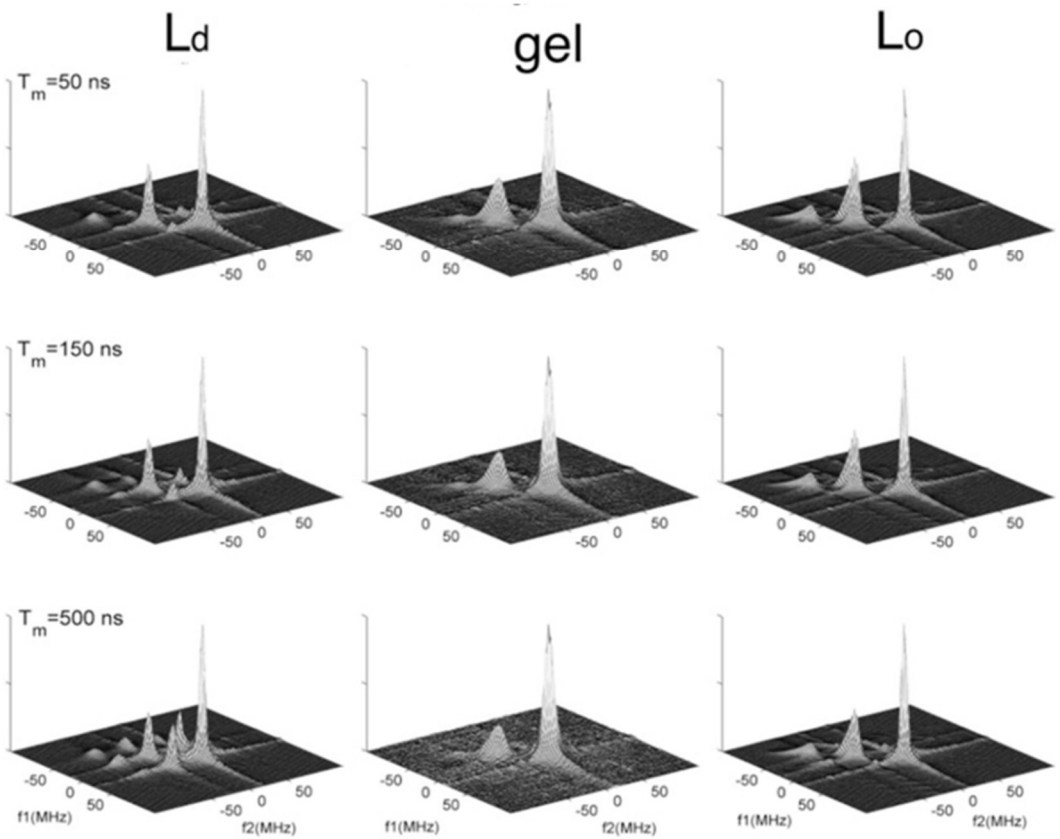

Figure 1-9: 2D-ELDOR experimental spectra of 16-PC molecule in (a) L_d (Liquid Disordered), (b) L_o (Liquid Ordered), and (c) gel phases in the magnitude mode with three different mixing times. Figure modified from Chiang et al (2007).[40]

Cw-ESR has been used to study plasma membrane vesicles (PMV's)[41] and live cells[19] to show coexisting L_o and L_d domains. The studies showed that these natural membranes exhibited predominately L_o phase behavior. Further, 2D-ELDOR spectroscopy was used to study the crosslinking of IgE- FcεRI receptors in PMVs and it was shown that crosslinking of these receptors lead to an increase in the L_d behavior of the cell membrane.[20] These studies show the utility of using ESR spectroscopy to study biological membranes especially to probe the lipid and protein interactions.

1.3. Pulsed Dipolar ESR and Distance Measurements

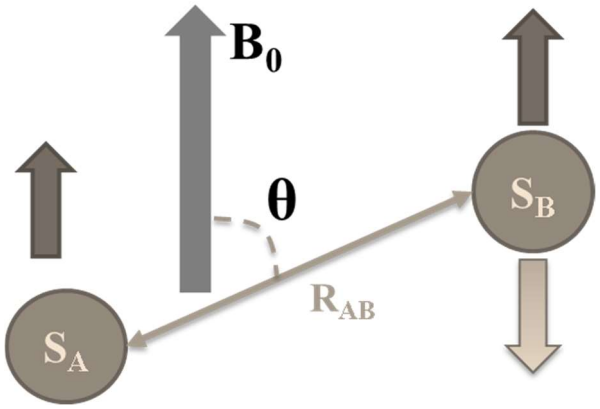

Figure 1-10: The electron spin dipole-dipole interaction between two spins (S_A and S_B) connected through space by the vector (R_{AB}). In DEER, the A-spins (S_A) are probed while the B-spins (S_B) are inverted by the pump pulses.

Pulsed dipolar ESR spectroscopy (PDS) has become a helpful tool for the measurement of nanometer range distances in biological systems.[58–61] Currently, PDS has been used to study 10-100 Å distances in a range of biological macromolecules (e.g. membrane proteins, RNA, DNA). PDS utilizes the weak dipolar interactions between two spin probes (**S_A; S_B**) attached to a biomolecule to identify distance distributions between the biomolecules. Two spin probes can interact weakly through dipolar interactions (long range) or strongly through Heisenberg spin exchange (short range). These spin exchange interactions can be used to study translational dynamics in the fluid state as will be seen in Chapter 2. In the frozen state, the dipolar interactions can be used to identify distance distributions.[1] The electron spin dipole-dipole interactions can be expressed as (in angular frequency units):[62]

$$\mathcal{H}_{\mathrm{dd}} \cong \omega_{\mathrm{d}}(3\,cos^2\,\theta - 1)\left[S_{1z}S_{2z} - \frac{1}{4}(S_1^+S_2^- + S_1^-S_2^+)\right] \qquad \text{1-IX}$$

where $\omega_d = 2\pi\nu_d = \frac{\gamma_e^2\hbar}{r^3}$, ħ is the reduced Planck's constant, γ_e is the gyromagnetic ratio of the electronic spin, r is the distance between the dipoles (R_{AB} in Figure 1-10), and θ is angle between the main magnetic field (B_0) and the vector $\overrightarrow{R_{AB}}$. $S_{1z}S_{2z}$ is known as the secular term while $S_1^{\pm}S_2^{\mp}$ is known as the pseudo secular term. Typically, for distances (R_{12}) greater than 20Å the pseudo secular terms are not too important for interacting nitroxides. For these larger distances and weaker dipolar couplings, pulsed dipolar ESR spectroscopy techniques became very important to obtain accurate distance information.

Pulsed Dipolar ESR spectroscopy is based on detecting spin echoes wherein the specific dipolar and exchange interactions can be separated out from other interactions such as spin relaxation by a utilizing an appropriate pulse sequence along with corresponding phase cycling. For more details refer to the reviews about Pulse Dipolar Spectroscopy by Borbat and Freed.[60,62] One commonly used PDS technique is the four-pulse double electron-electron resonance (four-pulse DEER[63,64]) and is discussed in detail below. There are two other important PDS techniques, (a) six-pulse Double Quantum Coherence[65,66] and (b) five-pulse DEER[67], that are not discussed here.

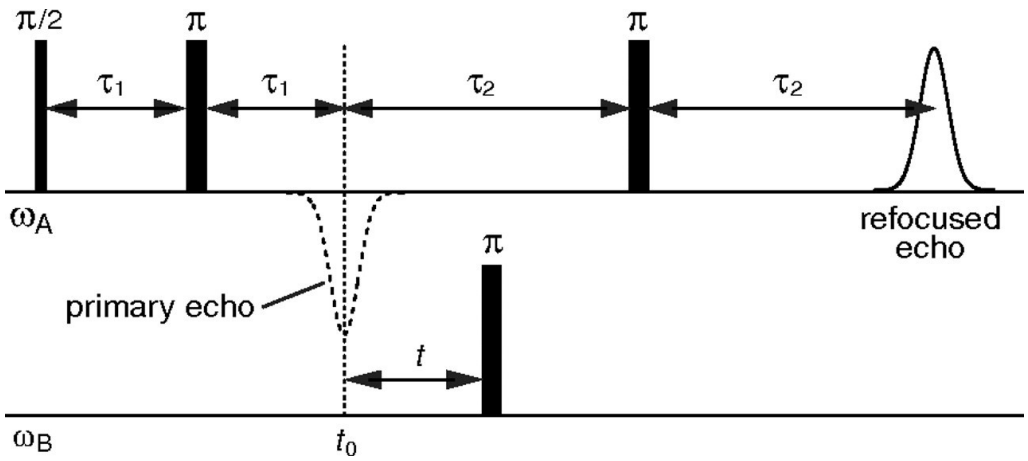

Figure 1-11: The four pulse DEER pulse sequence , the pulses acting on spins-A (at frequency ω_A) are the probe pulses while pulses acting on spins-B (at frequency ω_B) are the pump pulses. DEER is often also referred to as PELDOR.[59]

In the four-pulse DEER sequence (Figure 1-11), the first two pulses acting on the A-spins at a resonant frequency of ω_a lead to the formation of the primary echo. The third pumping pulse at a variable time (t) acting on B-spins at a resonant frequency of ω_b (sufficiently different from ω_a) leads to the inversion of the B-spins. Finally, a fourth pulse acting on A-spins (resonant frequency, ω_a) leads to the formation of the refocused echo. In a typical experiment, the times τ_1 and τ_2 are held constant while the time (t) is varied. The inversion of the B-spins by the third pulse inverts the coupling of the B spins to the A spins; this manifests itself as a modulation of the refocused echo amplitude:

$$V(t) = V_0\left[1 - p\left(1 - \nu(\omega_d t)\right)\right] \qquad \text{1-X}$$

Where V(t) is the echo amplitude after application of pump pulses at time t, V_0 is the echo amplitude in the absence of the pump pulse and p is the probability of B-spin flip. This expression is obtained by averaging over all the different orientations of the R_{12}.

The PDS time domain data (V(t)) obtained are then processed to obtain the distance distribution. The details of the data processing is discussed in detail below.

1.3.1. PDS data processing

The DEER data obtained in the time domain contains a background signal that is removed by linearly fitting the last few points of the data in a log plot. The pulsed dipolar distance distribution can then be obtained from the time domain data in a variety of ways. The relationship between the time domain data V(t) and the distance distribution P(r) can be expressed by the Fredholm integral equation of the first kind:

$$V(t) = V_0 \int_0^\infty P(r)\, K(r,t) dr \qquad \text{1-XI}$$

where K(r,t) is known as the kernel and for an isotropic sample is expressed as

$$K(r,t) = \int_0^1 \cos[\omega_d t\ (1 - 3u^2)]\, du \qquad \text{1-XII}$$

As can be seen in Equation 1-XI, the distance distribution can be easily obtained by inversion of Equation 1-XI. One common approach for the inverse reconstruction is the Tikhonov Regularization (TIKR) method[68,69] which gives a relatively stable solution for P(r). The TIKR based P(r) is typically further refined by the maximum entropy method(MEM).[70] The details of TIKR and MEM are not addressed here and are discussed in detail by Chiang et al.[68,70] The TIKR+MEM has been a valuable tool to extract pulsed dipolar distance distributions from the time domain data. However, it has been observed that this method for reconstruction is not artifact free[71] and tends to

exhibit oscillatory behavior in regions of high noise. Hence a new method based on Singular Value Decomposition was developed by Srivastava and Freed[72] and has been utilized in Chapter 4. Figure 1-12 summarizes the entire process of PDS data collection and processing to obtain the distance distribution.

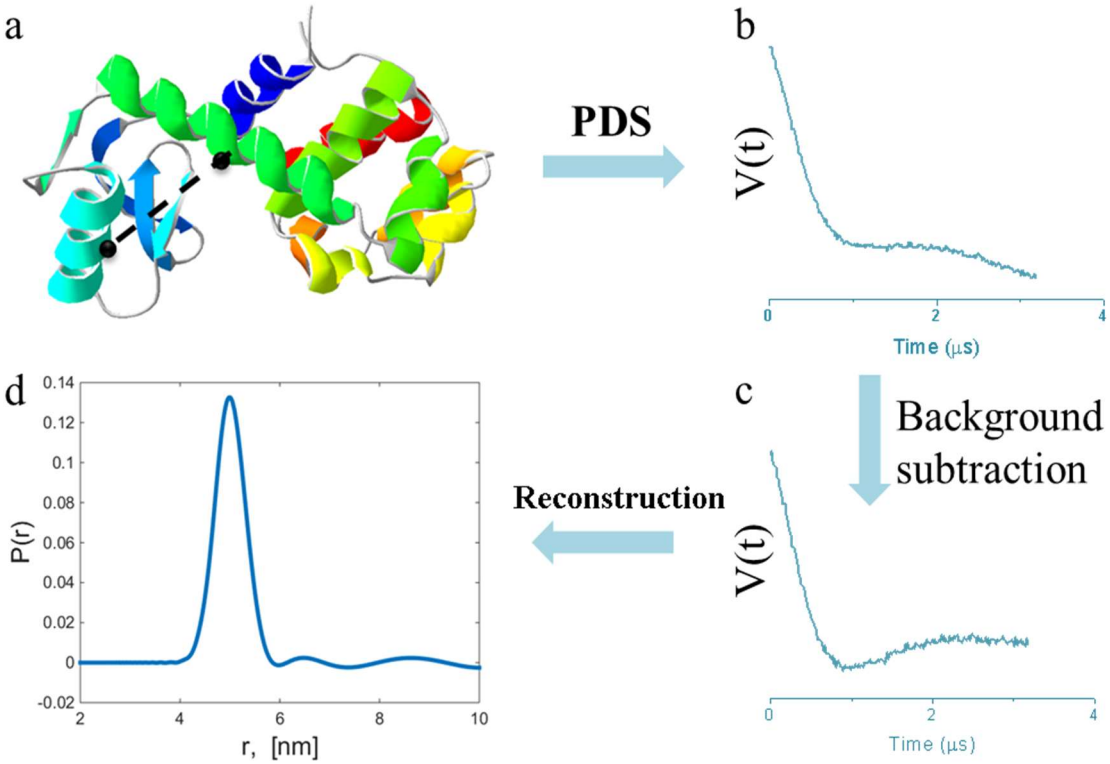

Figure 1-12: Pulsed Dipolar Spectroscopy from proteins to distance distributions. (a) T4 Lysozyme along with the two spin labels marked as two dark circles; (b) and (c) are model time domain PDS signal before and after background subtraction; (d) model PDS distance distribution that is typically obtained after reconstruction.

1.3.2. Biological applications and site-directed spin-labeling

As most biomolecules do not contain a paramagnetic species, the development of site directed spin labeling has enabled the introduction of a spin probes at specific locations in the protein. A common method is the spin labeling of cysteine residues[73] by MTSL

or (1-Oxyl-2,2,5,5-tetramethylpyrroline-3- methyl)methanethiosulfonate. MTSL is a highly reactive thiol specific spin label and binds strongly to the thiol group on the cysteine side chain. This spin labeling technique therefore has made it relatively easy to attach the spin probes to specific sites on the protein by site-directed mutagenesis. Further, as the two protein sites (between which the distance is measured) can be labeled by the same spin label (MTSL), spin labeling of proteins is relatively easy for PDS measurements.

PDS is extremely useful in the measurement of long-range distances (10-100 Å) that are typically not accessible by other technique. This is especially the case for large biomolecules or multiprotein complexes, as they cannot be measured by X-ray crystallography or NMR but are accessible to PDS. For example in the case of bacterial chemotaxis the coupling of *CheA Histidine Kinase* and the *Coupling Protein CheW* plays a vital role. These CheA-CheW complex formed is much too large to be studied by NMR, therefore PDS was used to obtain the structure of the complex formed.[61,74] The PDS distance distributions can be used to determine the stability of large protein complexes formed as broader distance distributions typically correlate to more flexible sidechain/residues. This was used to show that the HAMP domain of the bacterial chemoreceptors is more destabilized when the receptor kinases are in the ON-state.[75] One big advantage of PDS is that it can be studied in a variety of environments, such as dilute buffers, lipid vesicles[76], nano-discs[77] or even in the native membranes.[78] Further, PDS requires only a small amount of sample 20-40 µl of micromolar to sub-micromolar concentrations. In conclusion, PDS is an important technique that can be used to study long-range distances in the proteins and large macromolecules. We will be using PDS

to study the aggregation of immunoglobulin-E (IgE) by trivalent antigen to observe inter IgE distances in Chapter 4.

CHAPTER 2 : INSIGHTS INTO NITROXIDE SPIN LABEL PARTITIONING INTO LIPID MEMBRANES BY 95GHZ 2D-ELDOR AT ROOM TEMPERATURES

2.1. Introduction

Biological membranes containing over 1000 native lipid species exhibit complex phase behavior that is not always easy to characterize.[3,29] Model membranes composed of fewer components, e.g. one to four lipids and cholesterol helped to obtain crucial insights into dynamics and structure of biological membranes.[15,39,40,52,79,80] Membrane systems have been successfully studied using cw-ESR spectroscopy[10,18,19,81] among other techniques. The emergence of high power pulse ESR spectrometers with their ability to selectively detect or cancel out specific interactions help substantially to increase spectral resolution. Currently, most high power pulse spectrometers for room temperature liquid samples operate at lower ESR frequencies of 9/17 GHz.[20,33,39] At lower frequencies (9 GHz), the ESR spectrum is dominated by the hyperfine interaction while at high frequencies the ESR spectrum is dominated by the g-tensor anisotropy. High-frequency ESR (HF-ESR) spectroscopy, g-resolved ESR spectroscopy, can provide a further increase in spectral resolution. Therefore, high-power spectrometers operating at higher frequencies (95GHz or greater) at biologically relevant temperatures can provide further insights into membrane dynamics and structure.[6,82,83] Further, the HF-ESR's great sensitivity to g-tensor anisotropies provides greater orientational resolution for molecular dynamics studies. In addition, since HF-ESR provides a "faster

snapshot" of molecular motion compared to lower frequencies,[7,82,84] using multiple ESR frequencies gives insights into complex motional modes typical in biomolecules.[13,14] In this study, we show how High Field pulse ESR, in particular the two-dimensional electron-electron double resonance (2D- ELDOR) technique, can provide unique insights into the behavior of biological membranes.[85–90]

2.1.1.Two-dimensional ESR spectroscopy: 2D-ELDOR

Two-dimensional techniques in their various forms have gained widespread use in magnetic resonance spectroscopy. For example, the most common technique used in NMR, COSY (Correlation Spectroscopy), involves the use of a two-pulse sequence ($\frac{\pi}{2} - t_1 - \frac{\pi}{2} - t_2$). This convenient NMR technique, allowing successful separation of the scalar interactions has not been widely used in ESR. Two-dimensional Electron-Electron Double Resonance (2D-ELDOR) that incorporates a third $\frac{\pi}{2}$ pulse, analogous to 2D-Exchange NMR is extremely useful in ESR as it helps to understand the magnetization transfer between the different hyperfine lines of the ESR spectra.

This technique involves three $\frac{\pi}{2}$ pulses ($\frac{\pi}{2} - t_1 - \frac{\pi}{2} - T_m - \frac{\pi}{2} - t_2$) as shown in Figure 2-1. The periods after the first & second pulses are known as the evolution (t_1) and mixing (T_m) stages respectively. The data is collected during the detection time (t_2); a standard 2D-ELDOR measurement involves stepping out the evolution (t_1) period and recording the signal during the detection time (t_2) while holding the mixing time constant (T_m). Experimental data collection cannot be commenced immediately after

the third pulse; this time delay after the third pulse is known as the *'dead time'* of the spectrometer. The dead time can be attributed to instrumental factors. Our recent developments that can help alleviate the dead time limitations will be discussed elsewhere.[91]

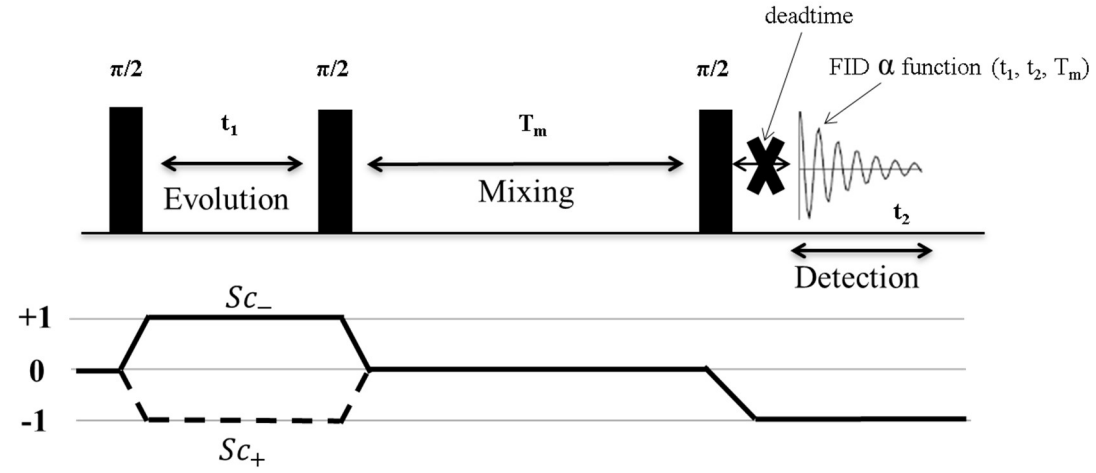

Figure 2-1: A standard three pulse two-dimensional Electron-Electron Double Resonance (2D-ELDOR) experiment along with the coherence pathway. All the spectra shown in this study corresponds to the Sc- pathway.

The advantage of using pulsed ESR, in particular, two-dimensional techniques is not only in increasing resolution but also in separating the different spin interactions using varied pulse sequences and phase cycling methods. In a standard 2D-ELDOR experiment auto-peaks are observed along the diagonal ($f_1 = f_2$) while cross peaks are observed off the diagonal. The auto-peaks are sensitive to the motional dynamics while the cross peaks being mixing time-dependent give us additional information about dynamic effects of inter-spin interactions such as spin exchange and electron nuclear dipolar (END) interaction.[10,81,90] 2D-ELDOR auto peaks have been used to study the phase behavior of membrane systems e.g. DPPC/Chol system,[40] the boundary lipids

surrounding the transmembrane peptide Gramicidin-A, and the crosslinking of IgE-FcεRI receptors on the cell membrane surface.[10,20,33] The off-diagonal peaks (cross peaks) in 2D-ELDOR spectra measure the rate of magnetization transfer by spin relaxation or exchange processes during the mixing time (T_m) period. Their intensity and ratio are affected by Heisenberg Exchange (HE) and Electron-Nuclear Dipolar (END) interactions,[85,87] which is discussed in detail later.

Further, the 2D-ELDOR analysis can be used to measure the relaxation rates (T_1 and T_2), a great advantage over cw-ESR based methods such as cw-saturation. The T_1 information can be obtained by carrying out a series of 2D-ELDOR experiments by varying the mixing time and observing the change in integrated intensity with the mixing time (T_m). Further, the 2D-ELDOR line shape analysis can give information about the T_2 relaxation times.

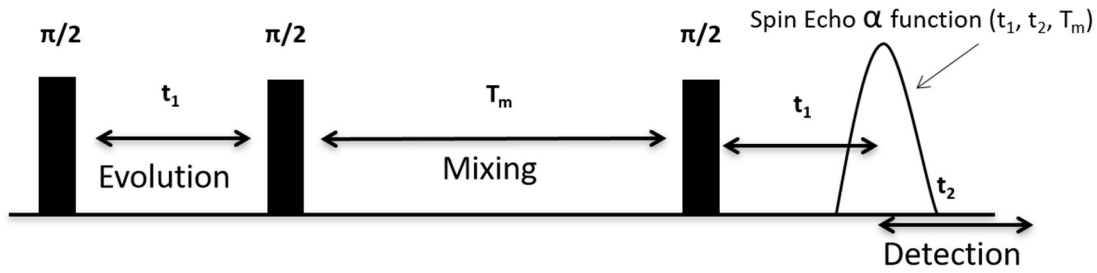

Figure 2-2: The three pulse 2D-ELDOR experiment in the Spin Echo Correlation Spectroscopy (SECSY) mode. Note, the only difference between the standard and SECSY modes is that the data accumulation starts only after time t_1 of the third pulse.

To obtain the T_2 information, first the phase distortions introduced to the 2D-ELDOR spectra by experimental artifacts (dead time and pulse imperfections) need to be corrected. Second, it becomes important to isolate only the homogenously broadened

(HB) part of the 2D-ELDOR spectra. A slice of the 2D-ELDOR spectrum along the diagonal (f_1=f_2) gives us an approximation of the cw-ESR spectrum that is largely inhomogenously broadened (IB), while in the perpendicular direction to the diagonal the linewidths of the auto peaks are reduced by an echo-like cancellation to give the homogenously broadened line shapes (HB), directly providing the T_2 information. For this purpose it is very convenient to observe 2D-ELDOR spectra in the SECSY mode (Figure 2-2), where the IB is observed along the f_2 dimension and HB along the f_1 dimension.[90,92,93] The SECSY mode is obtained by performing a shearing transformation of the 2D-ELDOR data set, i.e., replacing t_2 by (t_1+ t_2). This transformation causes the auto peaks to align parallel to the f_2 axis as seen in Figure 2-3.

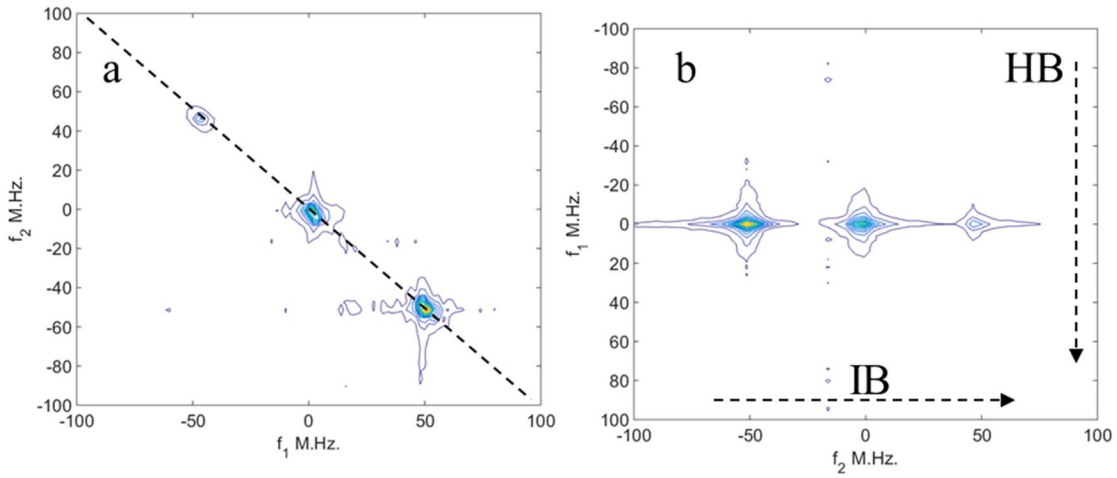

Figure 2-3: The 95 GHz 2D-ELDOR spectrum of 0.5mM TEMPO in water at 17 °C, and Tm = 50 ns. (a) Standard 2D-ELDOR experiment (b) 2D-ELDOR experiment displayed in the SECSY mode.

2.2.Features of 2D-ELDOR spectroscopy

2.2.1.Spin-Lattice Relaxation (T1)

In a standard three-pulse 2D-ELDOR experiment, during the mixing time (T_m) i.e., the time between the second and third π/2 pulse, the spins aligned along the negative z-axis are considered. Phase cycling is used to extract the coherence pathway for spins that reside along the negative z-axis between the second and third pulses. Hence, during that time, the spin-lattice relaxation (reported by T_1) is the primary source of relaxation. The decay of the 2D-ELDOR signal (Figure 2-4) with respect to the mixing times has a time constant corresponding to the spin-lattice relaxation (T_1) time.[88]

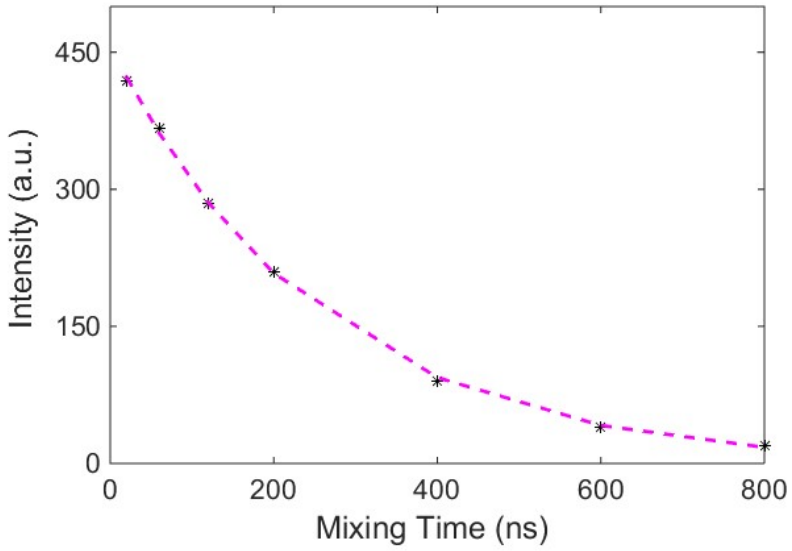

Figure 2-4: T_1 measurements by 2D-ELDOR spectroscopy. The rate of decay of signal intensity with the mixing time (T_m) gives us direct information about the T_1 relaxation rates.

2.2.2.Pure Absorption 2D-ELDOR spectra and Spin-Spin Relaxation (T_2)

As stated earlier, the 2D-ELDOR experiment is subject to phase distortions that need to be avoided or corrected. An approach commonly used is to present the data in the magnitude mode, where the phase distortions are not relevant at the sacrifice of spectral resolution; this leads to the reporting of the T_2* (the effective spin dephasing time) from the line widths. As the T_2* values are shorter than T_2, the magnitude mode spectra are typically broader. However, the most rigorous approach is to correct for these phase distortions in order to observe the pure absorption 2D-ELDOR spectra. In the pure absorption spectra, the line widths directly reflect the T_2 relaxation times. To extract the T_2 values from the 2D-ELDOR spectrum, the signal is observed in the SECSY mode where the IB and the HB linewidths are clearly separated. As noted earlier, the HB is displayed along the f_1 axis while the IB is shown along the f_2 axis. The full width at half maximum ($\omega_{\frac{1}{2}}$) along the f_1 axis, gives us information about the T_2 relaxation times, as they are related to each other by Equation 2-I.

$$T_2 = \frac{2}{\omega_{\frac{1}{2}}} = \frac{1}{\pi * \nu_{\frac{1}{2}}} \qquad \text{2-I}$$

The T_2 and the FWHM are inversely related, i.e. the broader the ESR line (corresponding to larger FWHM), the smaller is the T_2 relaxation time.

2.2.3.Cross peaks and Exchange

In 2D-ELDOR in addition to the auto peaks, important dynamical information can be obtained from the development of cross peaks (off diagonal). There are many different

relaxation pathways that are responsible for cross peak development. In a three-pulse 2D-ELDOR experiment, during the evolution time (t_1 after the first pulse) spins are allowed to precess at their natural frequencies in the transverse plane. During the mixing time (T_m) after the second pulse, half the spins are allowed to exchange/interact in the longitudinal plane (i.e., aligned along the z-axis) leading to the development of the cross peaks. The spins are then transferred into the transverse plane by the third pulse and the spins are detected during the detection period (t_2).[94] Spins that precess at the same frequencies during both the evolution and detection period lead to the development of auto peaks along the diagonal. However, electron spins that either exchange or engage in nuclear spin flips during the mixing time can yield different resonant frequencies in the evolution and detection periods, leading to the development of cross peaks. Therefore, the intensities of the cross peaks are directly dependent on the mixing time, i.e., the larger the mixing time the greater is the intensity of the cross peaks relative to the auto-peaks. There is, however, a natural limitation on the maximum mixing time that can be used in a 2D-ELDOR experiment, which is dependent on the T_1 of the sample, e.g. after $T_m \approx 3\text{-}5 \times T_1$ the signal decays by a factor of 20-150 and often becomes too weak to be analyzed. In the case of nitroxides, cross peaks typically develop by cross relaxation or "mixing" between the different nuclear spin states during the mixing-time period (Figure 2-5and Figure 2-15 in the supplement). In this study, we address three different cross peak development mechanisms – (a) Heisenberg Exchange (HE), (b) Electron-Nuclear Dipolar Interaction (END), and (c) Chemical or Physical Exchange between phases.

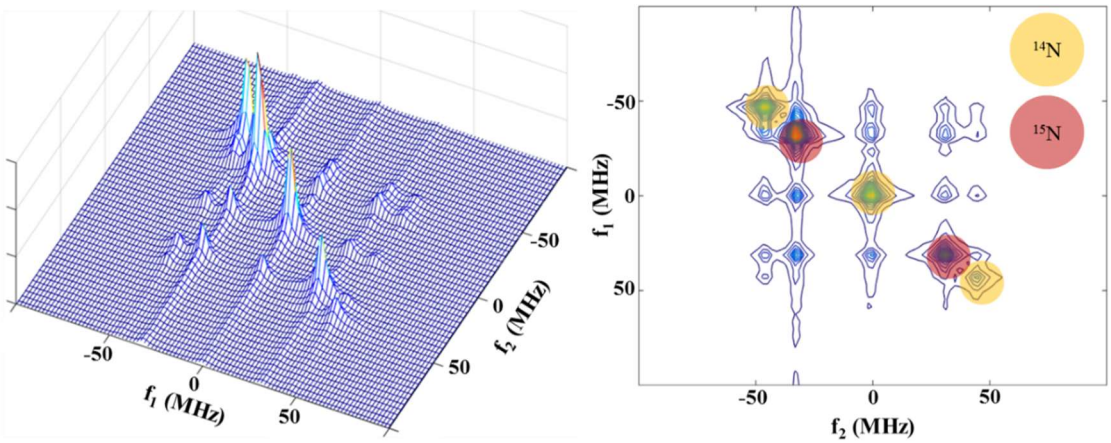

Figure 2-5: The 95GHz 2D-ELDOR spectra of ^{15}N-TEMPONE and ^{14}N-TEMPONE in water at 17°C at T_m = 400 ns. Cross peaks observed between the (^{15}N-^{14}N)TEMPONE is solely due to Heisenberg Exchange, while the cross peaks observed between ^{14}N-^{14}N TEMPONE and ^{15}N-^{15}N TEMPONE is due to both Heisenberg Exchange and END interactions. However, in this concentration limit, the Heisenberg Exchange dominates the END interactions. Note: ^{14}N, I=1(three peaks due to hyperfine interaction) while ^{15}N, I=1/2 (two peaks due to hyperfine interaction).

2.2.3.1.Mechanisms for developing cross peaks in 2D-ELDOR spectroscopy:

Heisenberg Exchange (HE) [87,95]**:** Heisenberg Exchange is a form of spin-spin exchange ($J\boldsymbol{S_1}.\boldsymbol{S_2}$, where S_1 and S_2 are the exchanging electron spins) arising due to collisions between the spin bearing molecules. In the case of nitroxides, any successful Heisenberg exchange has a 2/3 probability of a change in nuclear spin state. This is easily understood by the fact that each collision leads to scrambling of all the nuclear spin states, so the $m_I = 0, \pm 1$ states result with equal (1/3) probability. Therefore, in a 2D-ELDOR experiment, this leads to cross peaks of equal intensity as the selection rules are $\Delta m_I = \pm 0, 1, 2$; $m_{S_T} = m_{s_1} + m_{s_2}$($m_s$ is the electron spin quantum number) in the case of a ^{14}N-O. The Heisenberg exchange rate in the case of negligible nuclear spin relaxation can determined by the ratio of the auto peaks and cross peaks.[85] The effects of Heisenberg Exchange that lead to the development of cross peaks can be simulated

with our suite of non-linear least squares fitting programs.[92,96] Heisenberg Exchange also manifests itself in the form of line broadening (Heisenberg Uncertainty lifetime broadening) of the cw-ESR spectra due to the collision of radical pairs. Note, the difference between Heisenberg Exchange Broadening and Collisional broadening by paramagnetic relaxants such as nickel and oxygen (discussed further) as Heisenberg Exchange is between identical spins. Additionally, in a 2D-ELDOR experiment, Heisenberg Exchange will lead to the development of cross peaks while other collisional broadening will not lead to cross peaks. Finally, Heisenberg Exchange (HE) is both concentration and temperature dependent as is any bi-molecular reaction even though no activation energy is involved in Heisenberg Exchange.[97]

Electron-Nuclear Dipolar Interaction (END): The END interaction is due to the intramolecular hyperfine tensor interactions that couple the electronic and nuclear spin states (i.e.$A\,S_zI_{\pm}$) and is therefore largely independent of ESR frequency. The END mechanism leads to relaxation or mixing between the different nuclear spin states. In the case of the ^{14}N-O (nitroxide) the END mechanism, cross peaks arise due to the following transitions: $\Delta m_I = \pm 1$, $\Delta m_S = 0$. There is a possibility that $\Delta m_I = \pm 2$ cross peaks are also observed but they much weaker since they involve a two-step nuclear relaxation process.[85,98] The END mechanism is concentration independent but depends on the viscosity of the solution,[98] and hence is the dominant mechanism for cross peak development at low concentrations and temperature. Similar to HE rates, the END interaction rates (nuclear spin-flip rate, W_N) can be directly obtained by performing global fits of 2D-ELDOR experiments at different mixing times. Gorcester et al.[85] have

derived simple expressions for measuring the END interaction rates by comparing the ratios of the cross peaks to the auto peaks. END and HE can be easily differentiated by these two features; first, the $\Delta m_I = \pm 1$ and $\Delta m_I = \pm 2$ cross peaks have the same intensity for Heisenberg Exchange, while the $\Delta m_I = \pm 1$ peak is largely observed in the case of the END mechanism (Figure 2-15 in the supplementary section). Also their line-broadening effects are somewhat different. Furthermore, these two mechanisms have differing temperature dependence, END decreases with increase in temperature while HE increases.

Chemical and Physical Exchange[99]: Another mechanism that can lead to cross peak development is exchange. In this pathway, the spin label/probe is capable of occupying two or more sites having different g & A-tensors properties. During the mixing time of a 2D-ELDOR experiment, the spin label exchanges between the different sites at a fast enough rate that distinct cross peaks develop between the two sites which have different resonant frequencies. In 2D-ELDOR, we can observe exchange dynamics in a timescale range[3] of atleast 0.1-10 μs^{-1}, limited by the T_1 times of the nitroxides. Note, as there is no change in electronic or nuclear spin states during exchange the following selection rules apply for exchange: $\Delta m_I = 0$, $\Delta m_S = 0$. An example of exchange is proteins that have two conformational states such that the probes experience different environments. In the case of TEMPO partitioning between the lipid and aqueous phases, we have a change in environment from lipid to water than can manifest itself in cross peaks due to exchange. For two equally populated spin states, the relative intensities of the auto and

cross peaks are related to the mixing time (T_m) and exchange rate (r_{ex}) by the following equation:[100]

$$e^{-\frac{T_m}{2*r_{ex}}} = \frac{1-a(T_m)}{1+a(T_m)} \quad \text{where} \quad a(T_m) = \frac{Intensity\ of\ Cross\ Peaks}{Average\ of\ Intensitie\ \ of\ Auto\ Peaks}$$

The more complicated case of different population ratios is discussed later.

2.3.Experimental

2.3.1.Sample preparation

The solutions of 6-8 mg of DMPC in $CHCl_3$ were initially dried under a flow of gaseous N_2, followed by an overnight evacuation to completely remove the organic solvents. To this lipid, a 0.8 mM or 2 mM solution of TEMPO in water was added and hydrated at 50℃ for 30 min with occasional vortexing to prepare multilamellar vesicles (MLV's). Samples were transferred to a centrifuge tube and pelleted using a tabletop centrifuge for 25mins. The water phase above the lipid layer was carefully removed and the sample was deoxygenated using multiple freeze-thaw-pump cycles. This removal of water largely eliminates the bulk water phase but does not remove the interbilayer water, so the lipid bilayer remains fully hydrated. Under argon atmosphere in a glove box the samples were transferred into a concave well (etched with hydrofluoric acid) in one quartz plate, covered with another quartz plate of smaller diameter and sealed using a UV hardening Norland epoxy glue.[101] Air-saturated samples were prepared in the same way outside the glove box; for oxygen-saturated samples, we used an inflatable glove bag filled with oxygen and oxygen-saturated solutions.

2.3.2.Instrumentation

This study was carried out using the ACERT 95 GHz high-power pulse spectrometer that was designed for aqueous samples at physiological temperatures.[6,82,83] The details of this custom spectrometer have been described earlier.[6,83] In short, this spectrometer is based on a quasioptical set-up that has fairly low power (~90mW) transmitter-receiver (transceiver) that can be amplified by a ~1.2 kW extended interaction klystron (EIK) amplifier to generate a few nanosecond $\pi/2$ pulses. It uses a Fabry-Pérot resonator, with a variable mesh assembly. Wire grid polarizers are used to obtain isolation between the transmitted and reflected signals (after interaction with the sample). Built in phase shifters allow for control of the phase of the incident pulse. This spectrometer can also operate in the CW mode by bypassing the EIK and using the 90 Watt microwave radiation generated by the transceiver. Recent improvements to the 95 GHz spectrometer have provided a major step in enabling these experiment and are described in more detail later (c.f. 2.7.1).

2.3.3.ESR measurements

The continuous wave ESR & 2D-ELDOR measurements were performed on the home-built 95GHz pulsed & cw- ESR spectrometer,[6,83] with recent upgrades allowing for shorter dead time and more precise pulse shaping. The 2D-ELDOR measurements were collected with 64 (or 128) - 4ns t_1 steps and 1024 – 1 ns t_2 steps and a 32 step phase cycle was used.[93] The duration of the $\pi/2$ pulses for the 2D-ELDOR sequence, before each experiment, was determined from a plot of FID intensity vs. pulse length (Rabi

oscillations). A typical value of 5ns corresponds to a B1 of ~18G which gives good spectral coverage for a nitroxide radical in the fast motional regime (c.f. 2.7.2). The measurements were carried out using a spectrometer dead time of ~30ns.[6] The data collected from the spectrometer was processed using MATLAB® with custom data processing functions. The 2D-ELDOR data was directly obtained by 2D-Fourier Transform (2D-FT) of the time domain data, while in the case of the SECSY mode, a shearing transform ($t_2 \rightarrow t_1+t_2$) was applied in the time domain before the 2D-FT.

2.3.4.Nonlinear Least-Squares Analysis

The simulations of the 2D-ELDOR spectra in the frequency domain were performed using the nonlinear least squares fitting program (NLSPMC and NLSPMC.ri) which are available at http://acert.cornell.edu/index_files/acert_resources.php. In the case of the NLSPMC (magnitude mode) program, only the absolute magnitude of the complex frequency domain data was input to perform the fitting, while for the NLSPMC.ri (full $Sc\_$ mode) program, both the real and imaginary parts of the frequency domain data were input to perform the fitting. The fitting parameters and procedure for the magnitude and full $Sc\_$ mode have been described in detail earlier.[92,96] This simulation program helps us to obtain the ordering and motional parameters by performing a nonlinear least-squares fit of the two dimensional spectra to the motional models based on the Stochastic-Liouville equation.[90,92,96,102] The hyperfine (hf) and g tensors needed for the fits were obtained from references[83,103] and modified slightly to obtain optimal fits. The primary motional parameters obtained are the rotational diffusion constants, $R_\perp$ and $R_\parallel$,

which corresponds to the principal values of an axially symmetric rotational diffusion tensor. In some cases, the motional parameter $\bar{R}$ is used instead; it is defined as $\bar{R} = \left(R_{\parallel}^{\frac{1}{3}} \times R_{\perp}^{\frac{2}{3}}\right)$ along with the ratio of the rotational rates $N = \frac{R_{\parallel}}{R_{\perp}}$. The fitting procedure can also yield the ordering parameters (S_0 and S_2) but these parameters are not important for this study as the motion of the small TEMPO molecule is nearly isotropic in both the lipid (L_α) and the water phases and hardly affected by an orienting potential. In addition to motional and ordering parameters, the full Sc- fit also provides the phase corrections parameters (b1, b2, and a2) which are needed to correct for experimental artefacts (such as the dead time or pulse imperfections).[92] The phase correction factors help us to not only obtain "better" fit parameters but also help us obtain the pure absorption 2D-ELDOR spectrum, which is valuable to obtain accurate T_2 relaxation times.

2.3.5.Phase correction and extraction of pure absorption spectrum

The simplest way to obtain the pure absorption spectra is to set the phase factor values to zero, i.e., a2, b1, b2 = 0 and simulate the time domain spectra using the accurate motional and magnetic parameters.[92] The time domain data is then double Fourier transformed (with only the real parts of the taken into consideration at each step) to obtain the frequency domain data as shown in Equation 2-II.

$$\boldsymbol{Sc_{-}^{abs}(\omega_1, T_m, \omega_2) = Re\left[FT_{t_2}\left\{Re\left[FT_{t_1}\left\{Sc_{-}^{SECSY\ \backslash ELDOR}(t_1, T_m, t_2)\right\}\right]\right\}\right]} \quad \text{2-II}$$

2.4.Partitioning between lipid and water

In this study, we report the advantages of using high-frequency pulsed ESR technique to study membrane systems. We have analyzed in detail the ESR spectra of the spin probe (2,2,6,6-Tetramethylpiperidin-1-yl) oxyl (TEMPO) that partitions between water and lipid phases (Figure 2-6). We show how using 95 GHz ESR spectroscopy with enhanced g-resolution helps to provide insights into this system.[6,104] We use the lipid (DMPC - 1,2-dimyristoyl-sn-glycero-3-phosphocholine), with the gel to L_α phase transition close to room temperature (24.7 ℃). More precisely DMPC undergoes a phase pretransition from the L_β tilted gel phase to the P_β ripple gel phase around 14 ℃. DMPC then further undergoes a phase transition from the P_β ripple gel to L_α phase at close to 25 ℃.[105] Recent developments for our 95GHz 2D-ELDOR spectrometer enabled studying this membrane system in detail. The partitioning of TEMPO and other similar probes into membrane systems has been previously studied by cw-ESR spectroscopy.[45,104,106–108] Small nitroxide probes such as TEMPO partition between the aqueous and hydrophobic phases. ESR can detect TEMPO in both the aqueous phase and the hydrophobic core of lipid bilayers. The partition coefficient for TEMPO between lipid (L_α) and water phase is ~10-12 while for the lipid (P_β) – water phase is ~2-3,[104] which shows that TEMPO partitions favorably into the lipid phase (L_α and P_β) when compared to the water phase. Different values of the g-factor and A-tensor of TEMPO in the two different phases allows for good separation of the corresponding ESR signals.

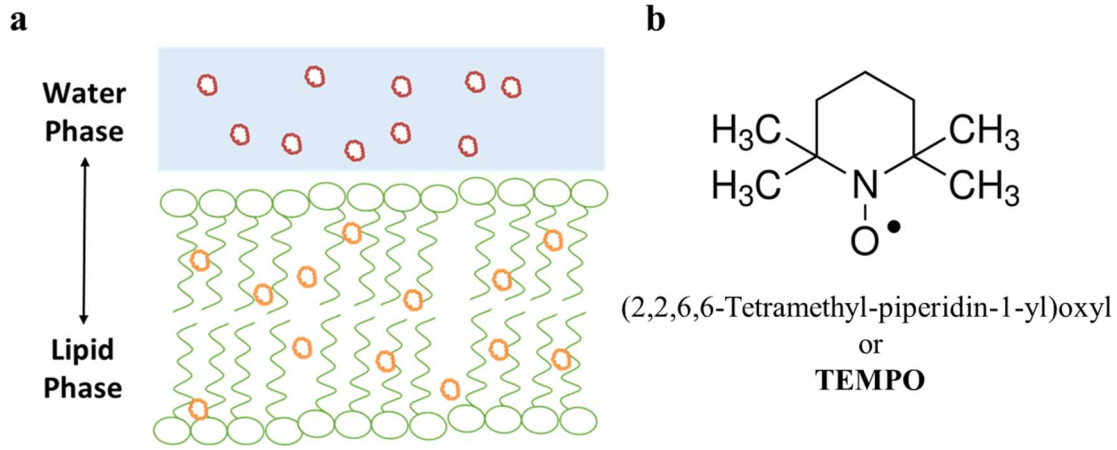

Figure 2-6: (a) A schematic depicting our system, where the spin label (TEMPO) is partitioning between the lipid and water phases, (b) the primary spin label used in the study (TEMPO).

2.5.Results

2.5.1.Lipid and Water phase at 95GHz

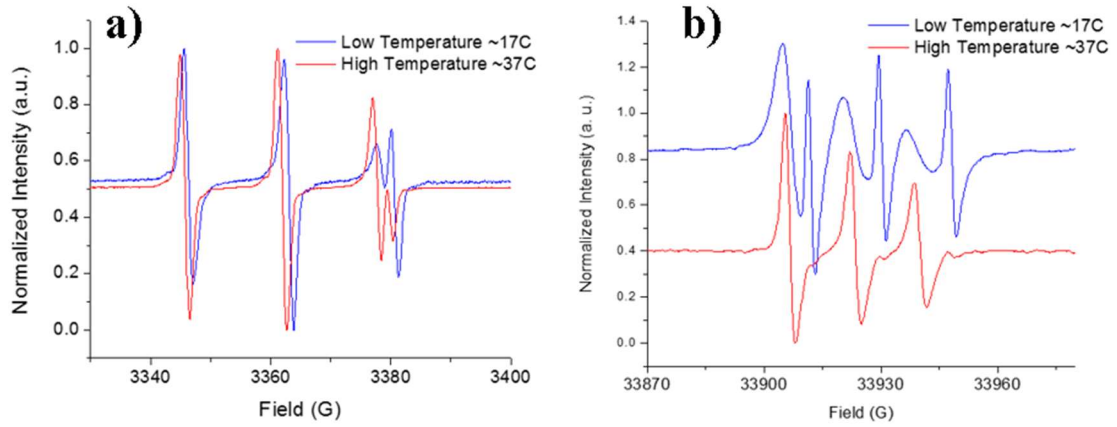

Figure 2-7: The cw-ESR spectra of TEMPO partitioning between the water and lipid phases (L_α at 37 ℃ and P_β at 17 ℃). (a) 9 GHz cw-ESR; (b) 95 GHz cw-ESR (lipid phase – broad, water phase – narrow). At 95GHz, the central peaks of the lipid and water phase are separated by around ~6.96 G (or Δv ~19.5 MHz).

TEMPO easily partitions into the lipid phase, with most spins located there as seen from cw-ESR spectra. In the lipid phase, the motions of the spin label molecules are

significantly restricted due to the steric and motional effects of the lipid environment. This causes a broader spectrum of the spin label in the lipid phase compared to the water phase. The extent of broadening depends on the temperature and the phase state (gel vs L_α) of the lipid phases. At X-band, two components from water and lipid (gel and L_α) phases are seen in the ESR spectrum but are not well resolved. High Field (95GHz) cw-ESR spectroscopy helps us to better resolve these two components owing to the differences in their respective g-factors; however, it is still difficult to obtain the spectra of each of these two phases separately (Figure 2-7). Using high field two dimensional-ESR techniques (HF-2D-ESR); i.e., 2D-ELDOR techniques we are able to completely resolve the lipid (broad) and water (narrow) phase components (Figure 2-8), thus combining the advantages of two-dimensional ESR with high field (g-resolved) ESR spectroscopy.

Although a number of nitroxide derivatives can partition between the lipid and water phases, the most appropriate choice for our experiments was TEMPO having three spectral lines; the different local polarity in the two different phases causes a field shift between them, with higher average g-factor value g_{iso} and lower hyperfine splitting constant A_{iso} for the lipid-embedded nitroxide. In 2D-ELDOR, these two signals are clearly observed at temperatures above 25 °C, which corresponds to TEMPO in the L_α phase of the DMPC bilayer and the water phase. Below 25 °C, though, only a signal from TEMPO molecules located in the water phase is detected.

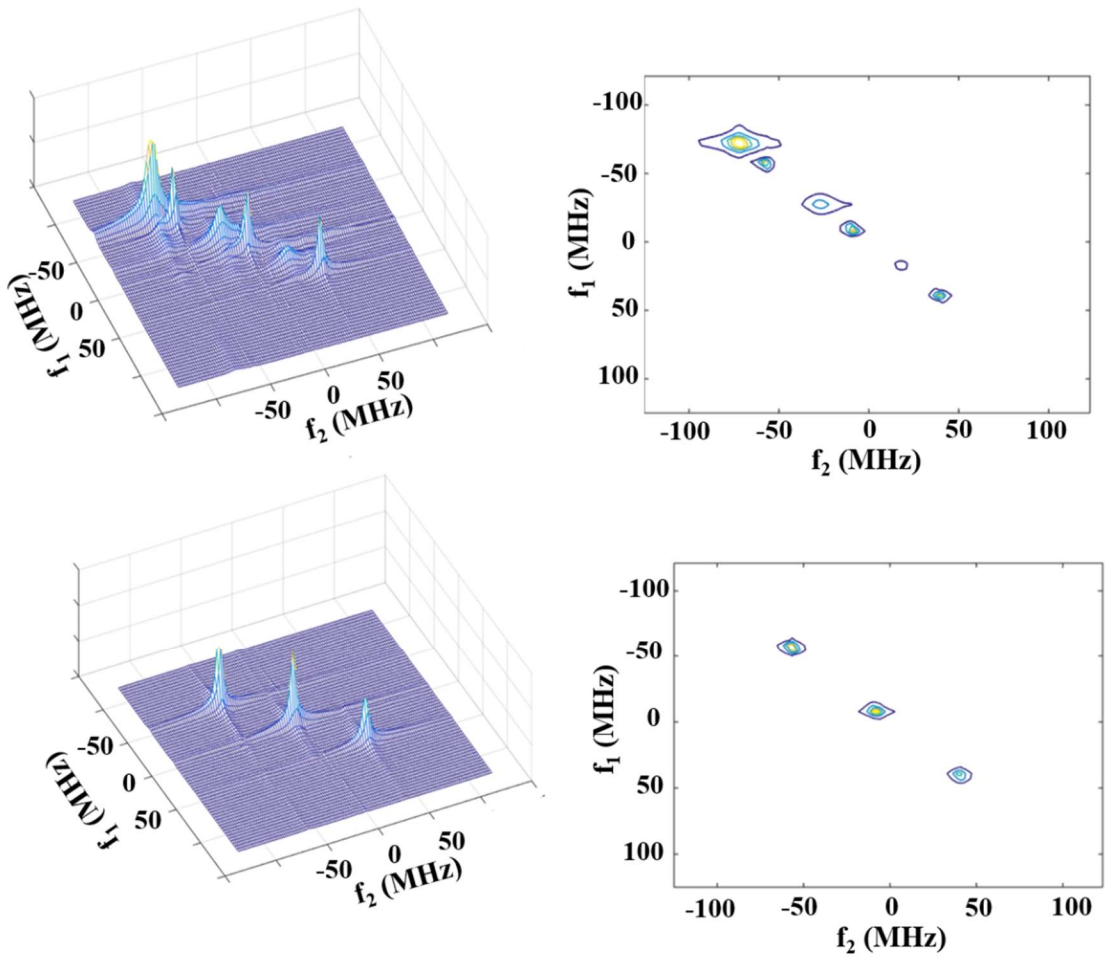

Figure 2-8: The 2D-ELDOR spectra of TEMPO partitioning in between the water and lipid phase. Top: 95GHz 2D-ELDOR at 37℃, T_m=50 ns and Bottom: 95GHz 2D-ELDOR at 17℃, T_m=50 ns. The plots on the left are two-dimensional mesh plots while those on the right are the corresponding contour plots. The contour plot (top-right) shows that the water and lipid phase peaks are well resolved by 2D-ELDOR at 95 GHz.

Increasing the temperature from 10 to 37℃ causes two abrupt changes in the ESR spectrum. First, at ~14℃ a conspicuous drop in the intensity of the water phase signal occurs. This temperature approximately corresponds to the L_β- P_β pretransition for the DMPC. In addition, the T_1 relaxation time of the water signal increases from 176 ns to 375 ns and cross-peaks between the hyperfine components of TEMPO substantially reduce (c.f. Figure 2-9). All these changes are indicative of a decrease in the

concentration of TEMPO in the water phase. At this temperature, the spin label molecules located in the gel (lipid, P_β) phase cannot be detected by 2D-ELDOR spectroscopy because of the current dead-time limitations, as the signal from the P_β decay before it can be collected by the receiver. The first change indicates an increase in TEMPO partitioning in the lipid phase upon L_β – P_β pretransition.[105]

The second abrupt change occurs at the main phase transition (25°C) and manifests itself as the emergence of the intense signal of TEMPO in the L_α phase. The intensities of these L_α phase peaks is consistent with the fact that TEMPO preferentially partitions into the lipid bilayer. This is also indicated by the emergence of cross peaks in the lipid phase (Figure 2-9). Because of the restricted motion of TEMPO molecules in this more viscous and ordered environment, one can see line broadening and a substantial difference of the intensity of the lines corresponding to different hyperfine components vs. TEMPO in water.

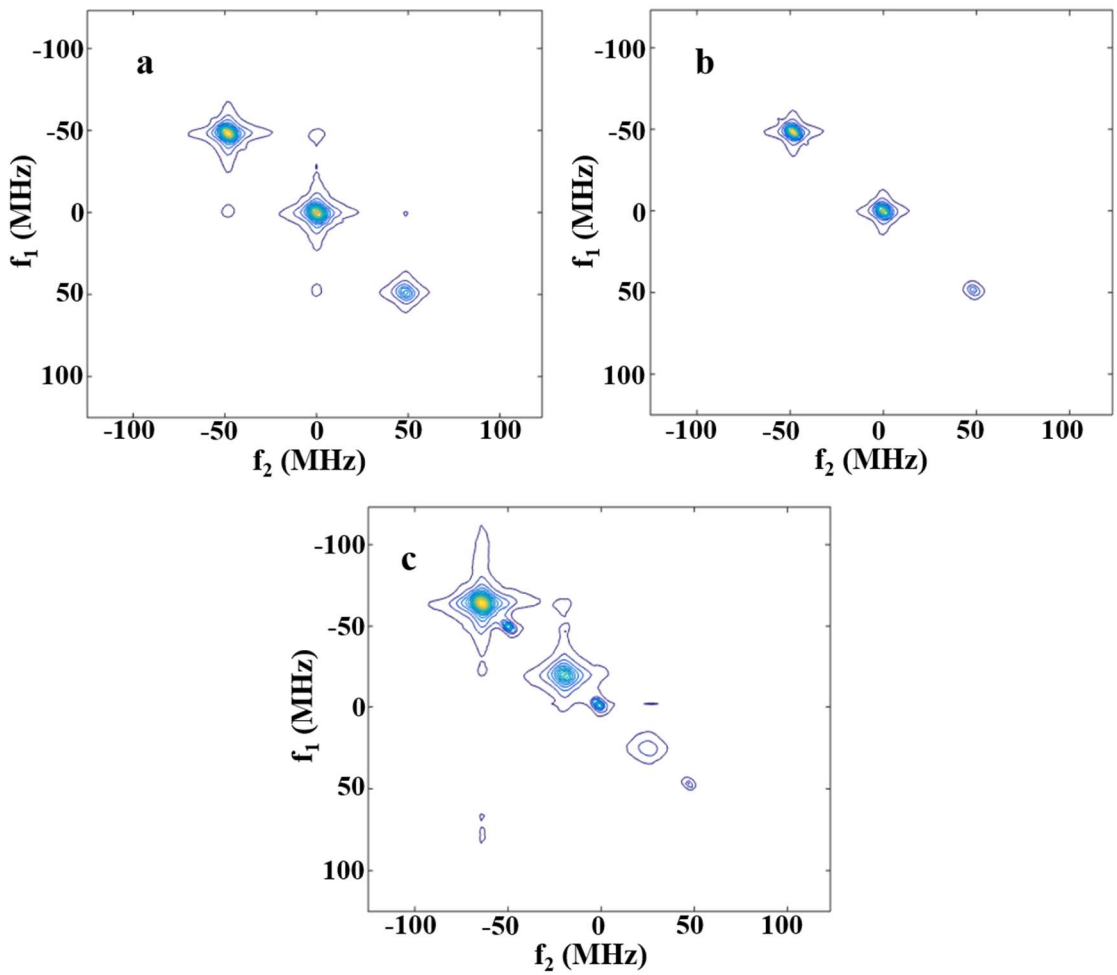

Figure 2-9: The 2D-ELDOR (contour) plots for the partitioning of 0.8mM TEMPO between water and DMPC measured with a mixing time (T_m) of 100 ns. The different plots represent three different temperature values (a) T = 12℃ (b) T = 17℃ (c) T = 37℃. Below the phase, pretransition (<14 ℃), cross peaks are observed for the water phase peaks while at 17℃ these cross peaks are negligible. Further at 37℃, cross peaks can be observed between the broader lipid phase peaks. This indicates that there is a significant drop in concentration of TEMPO in the water phase at the phase pretransition temperature of DMPC (~14 ℃).

2.5.2.Motional Analysis

The two components of the spin label partitioning between the water and lipid phase were simulated using the full $Sc\_$ routine[92,96] developed at ACERT to obtain the dynamical parameters of the systems (Figure 2-10 and Figure 2-11). The results of the

simulation are summarized in Table 2-1. They indicate that the rotational motion of the spin label is reduced by a factor of 3 in the lipid (L_α) phase ($1.2x10^{10}$ s^{-1}) when compared to the water phase (3.3×10^{10} s^{-1}). Similar rotational diffusion rates have been obtained from cw-ESR measurements. Cw-ESR also estimates that the motion of the TEMPO in the gel (P_β) phase is about an order of magnitude slower than in the L_α phase. In our simulations, we were also able to obtain the rates for the Heisenberg Exchange and the Electron-Nuclear Dipolar (END) mechanism. The END rate ($2W_n$) was $0.4x10^6$ s^{-1} in the water phase and $0.3x10^6$ s^{-1} in the lipid phase obtained from the development of cross peaks; these values are consistent with earlier observed rates for similar probes in the smectic phase of the liquid crystal S2.[85] The Heisenberg Exchange rate is proportional to the collision rate of TEMPO molecules, which is dependent on the concentration and the translational diffusion rate ($W_{ex} \propto c_{TEMPO} \times D_{TEMPO}$). At lower concentrations at 37 °C, the Heisenberg Exchange rate observed is negligible, i.e. the exchange rate is not significant enough to affect the development of cross peaks in 2D-ELDOR. At ~0.8mM TEMPO in water phase, the Heisenberg Exchange rate measured was ~$0.8x10^6$ s^{-1} for both the water and lipid phases. As the concentration of the spin label in the lipid phase is about an order of magnitude more than the spin label in the water phase,[104] it can be readily determined that the translational diffusion (D_T) of the TEMPO molecule is about an order of magnitude slower in the lipid phase. It is interesting to note that $R_{bar}^{TEMPO}(water) \sim 3 \times R_{bar}^{TEMPO}(lipid)$while $D_T^{TEMPO}(water) \sim 10 \times D_T^{TEMPO}(lipid)$. The anisotropic membrane environment can explain this difference in the rotational and the translational behaviors. For isotropic motion, both the rotational and translational diffusion (D_T) are dependent mainly on the viscosity. If the TEMPO

motion in both the phases (water and lipid) were isotropic then we would expect the R_{bar} ratios to be similar to the D_T ratios. However, for anisotropic media like fluid membranes, these ratios are dependent on the molecular size, orientation and viscosity.[109] TEMPO is a relatively small molecule that occupies the interstitial sites between the lipid molecules and its rotational diffusion is not very restricted while the translation diffusion is restricted to plane of the lipid membrane such that the lipid molecules interfere with the motion and accounts for the slower D_T. Other estimates for similarly sized molecules like ibuprofen also show that the translational diffusion is about 10 times slower in membranes than in water.[110]

A MOMD test fit of the lipid phase (L_α) spectra was carried out using a small amount of ordering, but this did not improve the Full Sc- fit, hence only an isotropic fit is carried out in this study. The rotational motion of TEMPO in the water and the lipid phase does not change with the addition of nickel and oxygen and only depends on the temperature (see below).

Table 2-1: Full Sc- Simulation parameters for the spin label TEMPO in the different phases. As the motion of the spin label is virtually isotropic the ratio of the motional rates, N=1.

Simulation Parameters	Water Phase	Lipid Phase
Concentration	2mM	18±2mM
Temperature	17 °C	37 °C
G-tensor	g_{xx}= 2.0087 g_{yy}= 2.0056 g_{zz} =2.00224	g_{xx}= 2.0099 g_{yy}= 2.0056 g_{zz} =2.00224
A-tensor	a_{xx}= 7.20 G a_{yy}= 7.10 G a_{zz}= 37.4 G	a_{xx}= 5.65 G a_{yy}= 5.65 G a_{zz}= 35.25 G
R_{bar}	3.3 x 10^{10} s^{-1}	1.2 x 10^{10} s^{-1}
$2W_n$ (END Rate)	0.4x10^6 s^{-1}	0.3x10^6 s^{-1}
W_{ex}	0.8x10^6 s^{-1}	0.8x10^6 s^{-1}
$T_{2,edi}$	200 ns	83 ns
Δ_g	0.52 G	0.80 G

Note 1: The spin label concentration in the lipid phase is estimated based on the partition coefficient between the lipid and water phases.

Note 2: The g-tensor and A-tensor values reported were obtained from the reference – Dzikovski and Freed (2012).[47]

Note 3: $T_{2,edi}$: The residual T_2 refers to the broadening independent term of the rotational modulation and g-tensor terms. The residual T_2 that induces additional homogeneous broadening due to processes such as spin rotational relaxation are also reported. These residual T_2 values observed are consistent with values obtained earlier for a similar spin label amido-TEMPO in water/glycerol solutions.[83]

Note 4: The full Sc- phase factors are typically in the following range: b1 and b2 ~ 0-6 ns, and a2 ~ -2 to 2 radians, these values are in a similar range to previously reported values.[92]

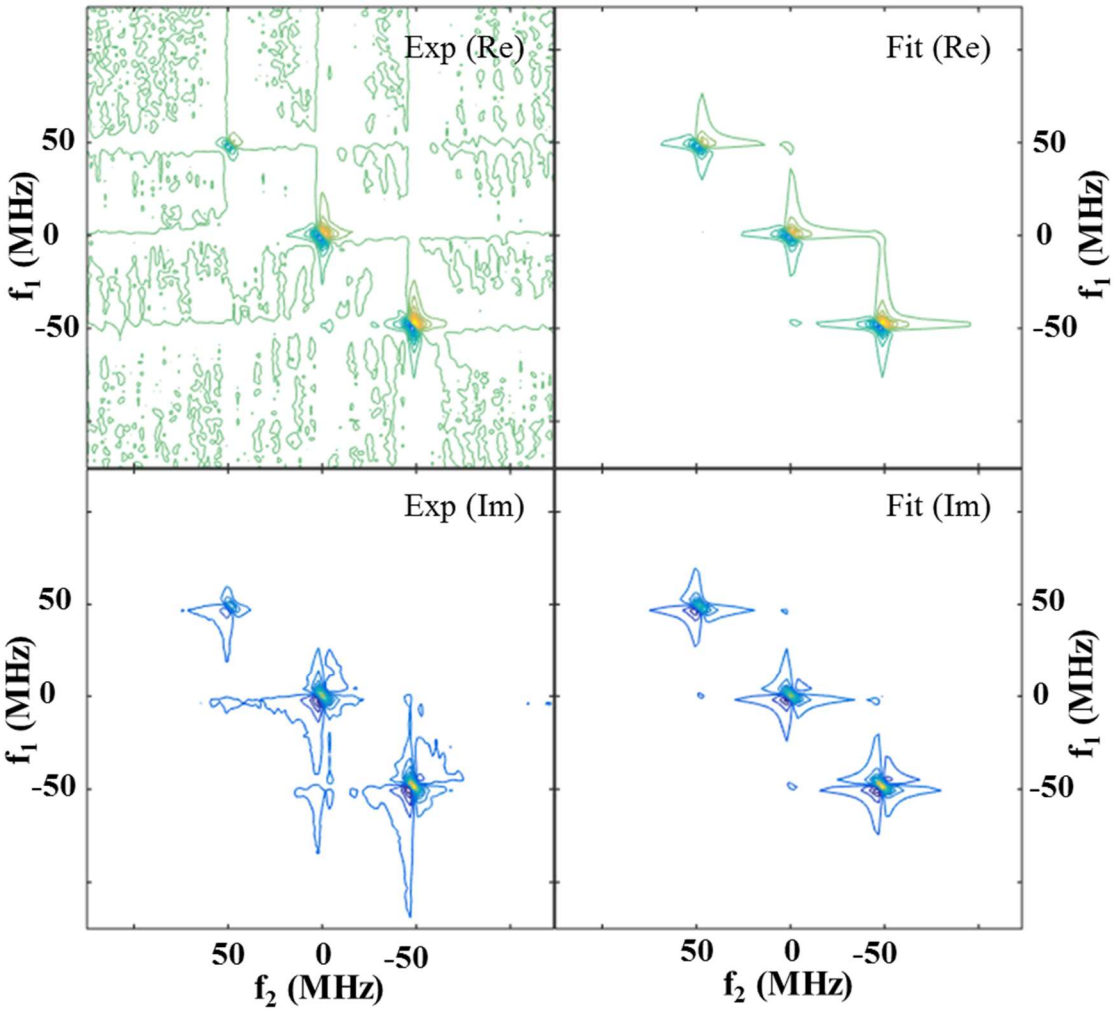

Figure 2-10: The experimental (Exp) and simulated (Fit) 2D-ELDOR spectrum of TEMPO in the water phase at 17℃, T_m = 20ns. Both the real (Re) and Imaginary (Im) parts of the spectrum are shown.

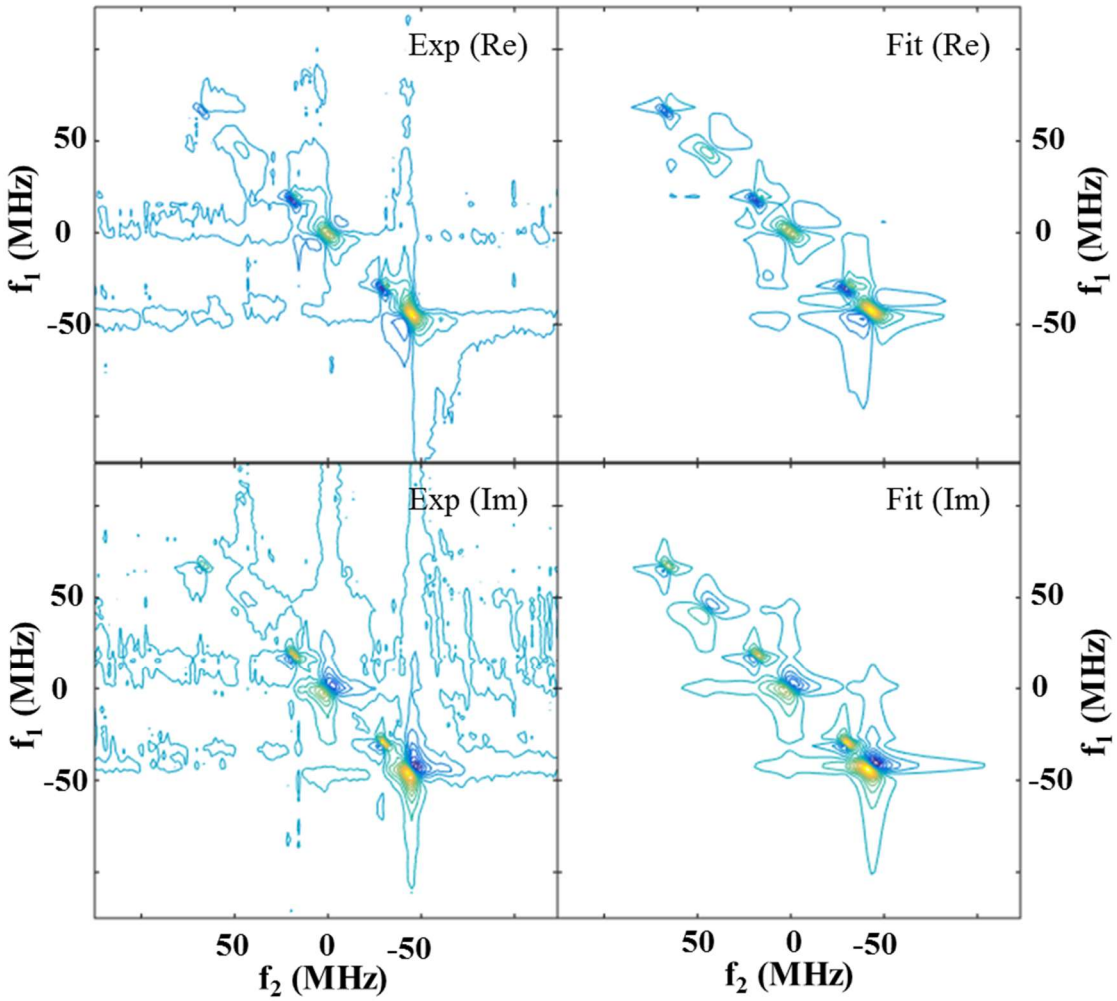

Figure 2-11: The experimental (Exp) and simulated (Fit) 2D-ELDOR spectrum of TEMPO in the lipid and water phase at 37℃, T_m = 20ns. Both the real (Re) and Imaginary (Im) parts of the spectrum are shown.

2.5.3.Lipid partitioning: Dynamic Equilibrium & Exchange

For a system of exchange between two phases, it is possible to introduce a two-state model, defined by the following parameters, the Larmor frequency (ω_1, ω_2) of the species in each of the phases, the population in each of the phases (p_1, p_2), and the rate constants (k_1, k_2) for the interconversion of the species. These rate constants are for the

forward and backward phase changes (k_1, k_2). They give us how fast the system responds to change (see expression below). Previous ESR and other studies have found the partition coefficient of similar systems[45,104,111] (molecular partitioning between the two phases) but none of these methods yield the rate of molecular exchange (defined by the sum of the rate constants), $k_{ex} = k_1 + k_2$.

$$\underset{\omega_1}{\underset{p_1}{\text{TEMPO}_{\text{Lipid}}}} \underset{k_2}{\overset{k_1}{\rightleftharpoons}} \underset{\omega_2}{\underset{p_2}{\text{TEMPO}_{\text{Aqueous}}}}$$

The difference in the Larmor frequency is $\Delta\omega = |\omega_1 - \omega_2|$. Note: $k_1 = 1/\tau_1$ and $k_2 = 1/\tau_2$, where τ_1 and τ_2 are the lifetime of the species in each phase. In our case, the lipid and water phase peaks are separated by ~7 G (for the central peaks) or 1.2×10^8 rad/s. In the case of fast exchange ($k_{ex} \gg \Delta\omega$), we would observe only one narrow peak at the average position of the two species. Since we observe well resolved water and lipid phase peaks, with the water phase peaks having nearly identical shape and field position to that of TEMPO in pure water alone, we conclude that in our case the exchange is slow i.e., $k_{ex} \ll \Delta\omega$. For a two state system, it is relatively straightforward to construct and solve the Bloch Equations modified to include the effects of the exchange, as seen below[112].

$$\frac{d}{dt}\begin{bmatrix}\widehat{M}_z(1)\\ \widehat{M}_z(2)\end{bmatrix} = \boldsymbol{L}\begin{bmatrix}\widehat{M}_z(1) - \widehat{M_0}(1)\\ \widehat{M}_z(2) - \widehat{M_0}(2)\end{bmatrix} = \begin{bmatrix}-k_1 - \frac{1}{T_1(1)} & k_2\\ k_1 & -k_2 - \frac{1}{T_1(2)}\end{bmatrix}\begin{bmatrix}\widehat{M}_z(1) - \widehat{M_0}(1)\\ \widehat{M}_z(2) - \widehat{M_0}(2)\end{bmatrix}$$

$$\frac{d}{dt}\begin{bmatrix}\widehat{M^{+}}(1)\\ \widehat{M^{+}}(2)\end{bmatrix}=\begin{bmatrix}-\mathrm{k}_1-i\omega_1-\dfrac{1}{\mathrm{T}_2(1)} & \mathrm{k}_2\\ \mathrm{k}_1 & -\mathrm{k}_2-i\omega_2-\dfrac{1}{\mathrm{T}_2(2)}\end{bmatrix}\begin{bmatrix}\widehat{M^{+}}(1)\\ \widehat{M^{+}}(2)\end{bmatrix}$$

where $M^{\pm}=M_x\pm i\times M_y$

In the case of slow exchange, as a first approximation, the off-diagonal terms in the modified Bloch equations can be ignored. Hence, it can be readily seen that the exchange broadens the peaks i.e., linewidths change from $\frac{1}{\mathrm{T}_2^{(1)}}$ to $\{\frac{1}{\mathrm{T}_2^{(1)}}+\mathrm{k}_1\}$ and $\frac{1}{\mathrm{T}_2^{(2)}}$ to $\{\frac{1}{\mathrm{T}_2^{(2)}}+\mathrm{k}_2\}$ for the first and second exchanging states respectively.[112,113] Similarly, the T_1 relaxation in presence of exchange is enhanced by the exchange rate such that the $\frac{1}{T_1^{ex}(1)}=\frac{1}{T_1^{0}(1)}+k_1$ and $\frac{1}{T_1^{ex}(2)}=\frac{1}{T_1^{0}(2)}+k_2$, where $T_1^{ex}(i)$ and $T_1^{0}(i)$ are the T_1 relaxation times of the i^{th} species in the presence and absence of exchange respectively. Further, as the population and the exchange rates are simply related $p_1=\frac{k_2}{k_1+k_2}=\frac{k_2}{k_{ex}}$, knowledge of one of the rate constants and the population ratios (via partition coefficients) are enough to identify the exchange rates.

We prepare our samples by eliminating excess bulk water; therefore, most of the observed water phase signal emerges from the interbilayer water layers. Comparing the relaxation in this condition merely to a solution of TEMPO in water may not be a good way to estimate the exchange rate from the increase in T_2^{-1}, since interbilayer water has been shown to differ from the bulk phase.[41] Therefore, we compare the linewidths and the T_1 of TEMPO in the water phase as the lipid molecules undergo the main phase transition (at ~25 °C) from the P_β to L_α phase to see the evidence for exchange. In the

gel phase (P_β), the viscosity of the lipid phase is significantly increased compared to the fluid (L_α) phase and therefore the translational diffusion of the TEMPO molecule is reduced by at least an order of magnitude.[105] This should significantly reduce the exchange rate between the lipid and water phase for the TEMPO molecule in the gel phase (P_β). If 0.8mM TEMPO solution is used to prepare the sample, the T_1 of the water phase changes from 469 ns at 17 ℃ to 433 ns at 37 ℃. If the exchange rate is slower at 17 ℃, if the reduction in T_1 at 37℃ can be attributed to the increase in the exchange rate as the lipid phase undergoes a phase transition. The calculated exchange constant (k_2) for the water phase is 0.18×10^6 s^{-1} or 0.18 μs^{-1} and the p_1 calculated from the intensities of the peaks is 0.89. This gives us an exchange constant (k_{ex}) of 0.22 μs^{-1}. This value should be taken as a lower estimate for exchange rate constant due to several reasons. First, since we compare to 17 ℃, a finite exchange rate at this temperature needs to be added to our estimate to obtain the exchange constant at 37 ℃. Second, as the lipid phase undergoes a phase transition, there is almost a fivefold increase in the TEMPO partition coefficient in the lipid phase;[104] this will lead to TEMPO depletion in the water phase. This decrease in TEMPO concentration could increase the T_1 in the water phase by lowering Heisenberg exchange; however, the observed decrease in T_1 indicates that relaxation enhancement from the exchange with the lipid phase overwhelms this effect. This exchange process should also affect the linewidths (via T_2), but the change in linewidths for this sample is very small, less than 0.1 G in line broadening.

Hence, even though the relaxation enhancement indicates the presence of exchange, it does not allow for precise measurement of the exchange rate. For systems with slow

exchange, 2D-Exchange Spectroscopy (2D-EXSY), the NMR analog of 2D-ELDOR, has been the most successful method to study the exchange rate in the system.[100,114] Therefore, 2D-ELDOR should be the most direct method to observe the dynamic exchange of spin probes between two phases. In 2D-ELDOR, we observe the rate of development of cross peaks between the spectral lines of the two species that undergo exchange (i.e., TEMPO exchanging between the water and L_α phase). The rate of development of cross peaks between the two phases directly measures the rate of exchange between the two phases.[6,87,95] The time domain 2D-ELDOR spectrum can be expressed[92,100] as:

$$s_{Sc-}^{\mathrm{ELDOR}}(t_1, T_m, t_2) \propto \sum_{jn} \exp\left(-\lambda_j^* t_2\right) \times [\exp(-\boldsymbol{L}\, T_m)]_{jn} \times \exp(\lambda_n t_1)\, \boldsymbol{M_{n0}}$$

where **L** is the matrix described above in the modified Bloch equations for the longitudinal relaxation and λ's are the complex eigenvalues of the relaxation operator. The diagonal elements of **L** lead to the development of the auto peaks while the off-diagonal elements of this matrix lead to the development of cross peaks. After 2D-Fourier Transformation along the t_1 and t_2 dimensions, we can obtain the intensities of the auto and cross-peaks as a function of the mixing time and the magnetization ($\mathbf{M_{n0}}$):[100,115]

Auto peaks:

$$I_{11}(T_m) = \frac{I_{11}(0)\left[-\left(\Lambda_- - k_1 + \frac{1}{T_1(1)}\right)e^{-\Lambda_+ T_m} + \left(\Lambda_+ - k_1 + \frac{1}{T_1(1)}\right)e^{-\Lambda_- T_m}\right]}{\Lambda_+ - \Lambda_-}$$

$$I_{22}(T_m) = \frac{I_{22}(0)\left[-\left(\Lambda_- - k_2 + \frac{1}{T_1(2)}\right)e^{-\Lambda_+ T_m} + \left(\Lambda_+ - k_2 + \frac{1}{T_1(2)}\right)e^{-\Lambda_- T_m}\right]}{\Lambda_+ - \Lambda_-}$$

Cross peaks:

$$I_{12}(T_m) = \frac{I_{11}(0)[(-k_1)e^{-\Lambda_+ T_m} - (-k_1)e^{-\Lambda_- T_m}]}{\Lambda_+ - \Lambda_-}$$

$$I_{21}(T_m) = \frac{I_{22}(0)[(-k_2)e^{-\Lambda_+ T_m} - (-k_2)e^{-\Lambda_- T_m}]}{\Lambda_+ - \Lambda_-}$$

Here Λ_+ and Λ_- are the eigenvalues of the **L** matrix such that,

$$\Lambda_\pm = \frac{1}{2}(k_1 + \frac{1}{T_1(1)} + k_2 + \frac{1}{T_1(2)} \pm \sqrt{\left(k_1 - k_2 + \frac{1}{T_1(1)} - \frac{1}{T_1(2)}\right)^2 + 4k_1k_2}$$

The easiest way to determine the exchange rate is by comparing the ratio of the auto peaks to cross peaks ($\frac{I_{11}}{I_{12}}$), as the above expressions are quite complicated.

In our experiments (Figure 2-12), we do not observe cross peaks for short mixing times (T_{mix} < 400ns), as the 2D-ELDOR experimental time scales are shorter than the rate of exchange. At long mixing times, the exchange cross peaks are visible. During the mixing time (T_m), as the T_1 occurs, a significant portion of the ESR spectrum is already decayed. For example, for a lipid phase with a T_1 of about 384 ns, about 87% of the signal intensity has decayed at the mixing time of 800 ns; this makes it more difficult to observe cross peaks, which are lower in intensity than the auto peaks. In our case, $k_2 \sim 8 \times k_1$, T_m = 800 ns, at 37 °C, we obtain an exchange rate (k_{ex}) of 0.52 μs^{-1} which gives us a mean exchange time of ~1.9 µs. In an ideal case, we should observe the gradual development of cross peaks for a series of mixing times, but this was not possible due to the relatively rapid T_1 relaxation and current sensitivity limitations.

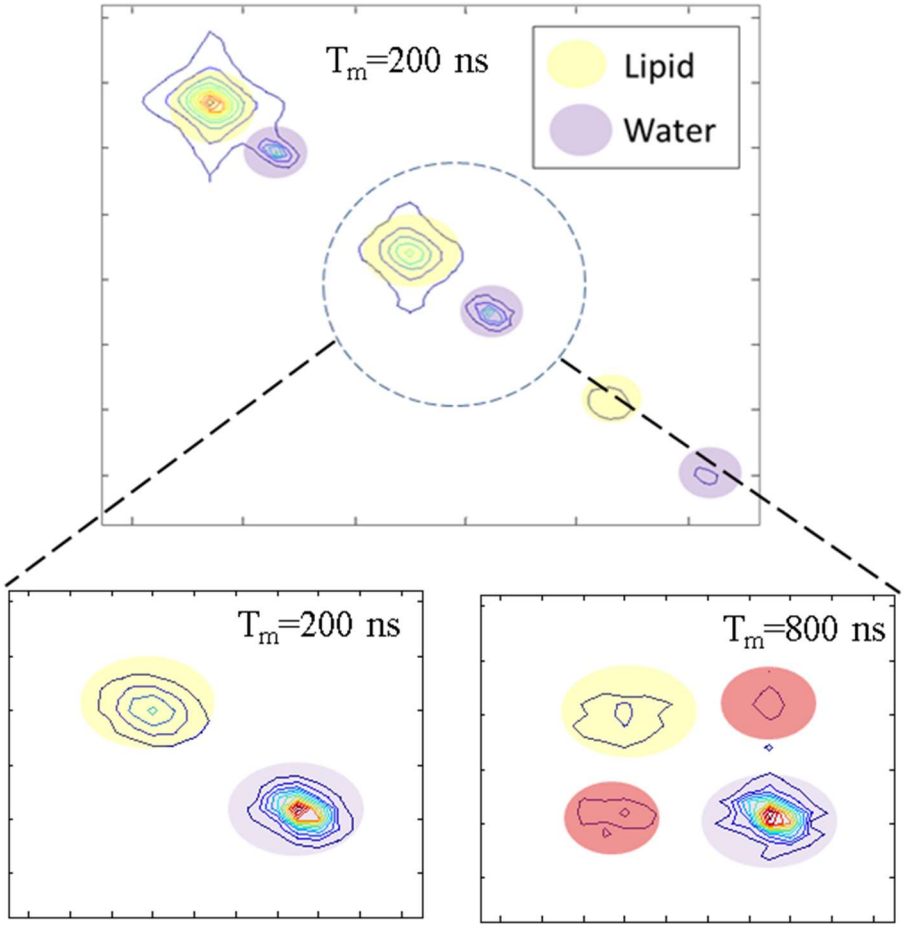

Figure 2-12: Development of exchange cross peaks with 2D-ELDOR. Top: 2D-ELDOR Spectra of the 0.8mM TEMPO partitioning between the Lipid and Water phases at 37°C, Tm = 200ns. Below: The central peaks of the 2D – ELDOR spectra are highlighted and the cross peaks developed due to exchange are highlighted in red. Note: the m_I = -1 peaks are the most intense and should in principle have the highest cross peaks, however, these peaks are not well resolved due to the proximity of the lipid and water phase peaks, while the m_I = +1 peaks are not intense enough to observe any cross peaks. Hence only the m_I = 0 peaks are shown and used in the analysis. For T_m = 800 ns, Intensities (in a.u.).: Lipid auto peak ~ 4.45 and cross peak intensity ~2.281.

We see that the exchange rate values obtained from 2D-ELDOR are larger than the values obtained from T_1, since the direct measurement of cross peaks is free from the artifacts mentioned above for the T_1 method. However, these 2D-ELDOR values can still give a lower estimate. As mentioned above our sample preparation method involves intense centrifugation in order to completely remove bulk water and to obtain fully

hydrated multilamelar vesicles containing only hydration and interbilayer water. However, due to the complex nature of the multilamelar vesicles and the hydration process, their phase may contain micro-inclusions of bulk water. These inclusions would be less disperse than the interbilayer water and likely have a lower exchange rate with the lipid phase than the interbilayer water. Consideration of the presence of this slow exchanging bulk water will lower our estimates of the exchange rate.

Here we for the first time report a direct observation of exchange due to small molecule partitioning between the lipid and water phase by ESR. Exchange has been routinely studied by various NMR techniques, with the time scale observed by cross peak development and relaxation enhancement spanning from milliseconds to nearly seconds.[116] On the other end of the timescale, very fast exchange processes can be studied by 2D infrared spectroscopy, with its ability to detect dynamics in the picosecond regime defined by the short lifetimes of the excited vibrational states.[117] Here we report the use of 2D-ELDOR ESR to detect and study exchange with characteristic times in a range of nanoseconds to greater than microseconds, an important timescale for a variety of biological processes.

2.5.4.Paramagnetic Relaxants

Relaxation enhancement of nitroxide spin labels by other paramagnetic compounds in the membrane environment can provide important information about location and functionality of various constituents in biomembranes. Paramagnetic relaxants such as nickel selectively broaden the different components of our partitioning system, with

nickel ions primarily broadening the water phase component. While spin-labeling sites located near the membrane surface are accessible for water-soluble polar paramagnetic species (e.g. metal ions), the sites submerged into the hydrophobic core of the membrane will be more affected by oxygen.

Since for nitroxides at room temperatures usually $T_2 << T_1$, change in the T_1 value should be much more sensitive to weak interactions[118] while using T_2 adequately reports on stronger magnetic interactions. The saturation recovery method[119,120] has been so far most useful to observe T_1 relaxation in lipid membranes, in particular, the hybrid technique by Subczynski and Hyde using long saturation pulses and following observation of the signal by low-power cw-ESR.[118] Simple and readily available cw power saturation technique can detect the T_1 effects indirectly. It has been extensively used to measure relaxation enhancements of spin labels by paramagnetic compounds along with direct line broadening measurements reporting T_2 effects. We illustrate these cw techniques and their application range using an example of $Ni(ClO_4)_2$ at a concentration in water of c_r = 1mM interacting with TEMPO with an exchange constant of k_r=1.1×10^{9}s^{-1}M^{-1}.

2.5.4.1.Linewidth broadening by cw-ESR

In cw-ESR line broadening experiments, the changes to linewidth (B_{pp}, the peak-to-peak linewidth) induced by paramagnetic relaxants is measured. The change in linewidth is defined as $\Delta B_{pp} = B_{pp}^r - B_{pp}^0 \propto \frac{1}{T_2^r} - \frac{1}{T_2^0}$ and $\frac{1}{T_2^r} = \frac{1}{T_2^0} + k_r c_r$

It gives for $\Delta B_{pp} = \frac{2k_r c_r}{\sqrt{3}\gamma_e}$ ~ 0.073G – barely detectable for 1 mM of Ni^{2+}, but for 10 mM the ΔB_{pp} is ~0.7 G, which is in a convenient range for reliable measurements. This shows that cw-ESR linewidth broadening is appropriate only for relatively strong relaxation enhancements.

2.5.4.2. Cw-ESR saturation experiment

Cw-ESR saturation experiments measures the change in the value of the saturation factor (P), which is a product of both the T_1 and T_2 relaxation times, defined as $P = \gamma^2 T_1 T_2$. Usually the value $\Delta\left(\frac{1}{P}\right) = \frac{1}{P_r} - \frac{1}{P_0}$ is used to characterize the effect of the paramagnetic relaxant,[49] where P_r is the saturation factor in the presence of the relaxant while P_0 is the saturation factor without the relaxant. The equation is readily modified to $\Delta\left(\frac{1}{P}\right) = \frac{1}{\gamma^2}\left(\frac{1}{T_1^r T_2^r} - \frac{1}{T_1^0 T_2^0}\right)$.

For the case of collisional or Heisenberg exchange, the relative change in $1/T_1$ and $1/T_2$ are equal i.e., $\Delta\frac{1}{T_1} = \Delta\frac{1}{T_2}, \frac{1}{T_2^r} = \frac{1}{T_2^0} + k_r c_r$ and $\frac{1}{T_1^r} = \frac{1}{T_1^0} + k_r c_r$, we get $\Delta\left(\frac{1}{P}\right) = \frac{1}{\gamma^2}\left(\frac{k_r c_r}{T_1^0} + \frac{k_r c_r}{T_2^0} + k_r^2 c_r^2\right)$.

For our values of k_r and c_r and taking T_1^0 and T_2^0 as 380 and 80 ns respectively it gives $\Delta\left(\frac{1}{P}\right) = \frac{1}{(1.76 \times 10^7)^2} \times (1.66 \times 10^{13} + 1.21 \times 10^{12}) = 0.053\ G^2$.

The $\Delta(1/P)$ = 0.05 corresponds, for example, to a change of P from 5 to 4. This can be detected by a CW saturation experiment although it still requires precise sample

positioning and B_1 measurements. For lower relaxant concentrations (i.e., $k_r c_r \ll \frac{1}{T_2^0}$), we see that the term $\frac{k_r c_r}{\gamma^2 T_2^0}$ makes the major contribution into $\Delta\left(\frac{1}{P}\right)$ and other terms can be ignored in the first approximation.[49] On the other hand, for higher relaxant concentrations, when the third term substantially contributes as $k_r^2 c_r^2 \approx k_r c_r \left(\frac{1}{T_1^0} + \frac{1}{T_2^0}\right), i.e.\ \frac{1}{T_2^0} \sim k_r c_r$, we will already observe substantial line broadening, e.g. for 10mM of Ni^{2+} (i.e., $\frac{1}{k_r c_r} \sim T_2^0$=80 ns) it will be ~ 0.7G. At these conditions (10 mM Ni^{2+}) as for relatively strong relaxation enhancement in general, direct linewidth measurement will be more reliable than saturation, which could be difficult to observe.

2.5.4.3. Two-dimensional ESR and relaxation measurements

However, the techniques most sensitive to relaxation enhancement are two-dimensional ESR techniques such as 2D-ELDOR. First, we can directly and separately determine the relaxation times (T_1 and T_2). Second, in pulsed 2D-ESR we often require relatively smaller concentration of paramagnetic relaxant to observe considerable effects to spectra when compared to cw-ESR.[121]

2.5.4.4. Oxygen: Simple Collisional Exchange

In samples prepared in air atmosphere, the concentration of oxygen in the lipid phase is significantly higher than in the water phase. The solubility of oxygen in water is ~ 1.56 mM at 17°C, 1.38 mM at 25 °C and 1.2 mM at 37°C at standard atmospheric

pressure.[122,123] This yields 0.33, 0.29 and 0.25 mM for air-saturated solutions, respectively. In hydrocarbon solvents, the solubility was reported 10.64 mM in *n*-hexadecane at 25°C[124] (2.23 mM at air pressure) and ~ 11.1 mM in *n*-decane at 25°C (2.35 mM at air pressure) with very little temperature trend at 10-40°C. In[125] a slightly outlining but close value of 1.72 mM for *n*-dodecane at air pressure at 35°C is given, as well as a distribution coefficient of 7.9 for oxygen between dodecane and water phases. A partition coefficient of 4.4 for olive oil vs water[126] has been used in a number of papers as an estimate for the oxygen concentration in lipid membranes. Therefore, we expected that oxygen would induce greater broadening in the lipid phase spectra compared to the water phase.

However, the effect of oxygen on the relaxation rate of TEMPO in various media is defined by its concentration-diffusion product.[124,127,128] As discussed earlier, at low concentration of the relaxant, the additional relaxation $\propto k_r c_r$, as the collisional rate (k_r) is directly dependent on the diffusion rate (D_r) and additional relaxation $\propto D_r c_r$. The diffusion rate of oxygen was estimated 1.51×10^{-5} cm^2/s in DMPC vesicles at 37°C,[128] similar to water and n-hexadecane (2.11×10^{-5} cm^2/s and 2.49×10^{-5} cm^2/s respectively[124]). The relative high diffusion of oxygen in membrane environments, similar to diffusion in water, has been discussed earlier.[118] The effects of oxygen on membranes has been previously studied by Subczynski, Hyde and coworkers earlier using the saturation recovery method to observe the T_1 relaxation rates.[42,118,129]

Indeed, the oxygen-induced relaxation enhancement in water follows the Henry law, estimate $(\frac{1}{T_1^{oxygen}} - \frac{1}{T_1^{argon}})$ for 100% O_2 gives ~7-8$\times10^6$ s^{-1}. This value is smaller than

literature data on oxygen- induced $\Delta (1/T_1)$ on PC spin labels in fluid DMPC membranes measured by progressive cw saturation[43] or by saturation recovery[42] techniques, 9-16×10^6 s^{-1}. In our experiments, for the DMPC membrane the T_1 values change from 329 to 168 ns upon addition of air (i.e., 20% Oxygen), this corresponds to a $(\frac{1}{T_1^{air}} - \frac{1}{T_1^{argon}})$ value of 2.9×10^6 s^{-1}, hence for 100% O_2 we obtain a $\Delta (1/T_1)$ value of ~14.2×10^6 s^{-1} (Figure 2-18, Figure 2-19, Figure 2-20, and Table 2-2 in the supplement). Note that for the lipid phase (L_α) signals we also observe equal values of $\Delta(1/T_1)$ and $\Delta(1/T_2)$; this shows that oxygen induces relaxation only due to collisional exchange. Thus, we conclude that for TEMPO the relaxation enhancement (RE) value due to oxygen in membranes is approximately double the RE by oxygen in water. Therefore, the diffusion-concentration product for oxygen in membranes is roughly double the value for oxygen in water. Taking into account the difference in diffusion rate between water and DMPC, we estimate the effective oxygen concentration at the site of the spin label (TEMPO) in the lipid phase is ~2-2.5 times the concentration of TEMPO in the water phase.

This result is in general consistent with the line broadening of cw-ESR due to the addition of oxygen. The line broadening can be determined from the best fit of the spectrum of an air-saturated by a convolution of the spectrum recorded under anaerobic conditions with a Lorentzian line (c.f. 2.7.11). For TEMPO in the L_α phase at 37 °C, the linewidth broadening for the addition of air is 0.18G, while that for 100% oxygen is 0.90G. These values give us the relaxation parameters of 2.8×10^6 s^{-1} and 13.7×10^6 s^{-1} for air and 100% oxygen respectively. For TEMPO in water, we observe line broadening

of 0.11G and 0.57G for air and 100% oxygen respectively, which gives us relaxation enhancement parameters of 1.7×10^6 s^{-1} and 8.2×10^6 s^{-1}. These values are similar to $\Delta(1/T_1)$ and $\Delta(1/T_2)$ observed by 2D-ELDOR. In samples of TEMPO in the hydrophobic solvent (hexadecane) prepared in anaerobic vs aerobic (21% Oxygen) conditions, the increase in T_1 relaxation (from 193 ns to 47 ns) due to the presence of oxygen is also equal to the increase in T_2 relaxation, which is $16.2\times10^6 s^{-1}$. The cw-ESR spectrum of TEMPO in hexadecane has 0.92G of additional broadening due to the addition of air, which corresponds to a relaxation enhancement of $14.0\times10^6 s^{-1}$. This relaxation enhancement (RE) for air in hexadecane (~14-16.2 $\times10^6 s^{-1}$) roughly a factor of 10 greater than the RE for oxygen in water (~1.4-2 $\times10^6 s^{-1}$). After accounting for the differences in the diffusion rates of oxygen, it is readily seen than the solubility of oxygen is about an order of magnitude greater in hexadecane than water, consistent with literature data.[124]

2.5.4.5.Nickel: Collisional Exchange coupled to exchange dynamics

Nickel salts have a different effect than oxygen, as they are only soluble in the water phase and hence enhance relaxation in the water phase (c.f. Figure 2-13). This can be used to selectively remove the signal emerging from spin label molecules partitioned into the water phase. The addition of 5mM Ni^{2+} to TEMPO causes the T_1 relaxation times to reduce from 375ns to 111 ns, thereby leading to a relaxation enhancement ($\Delta\frac{1}{T_1}$) of $6.34x10^6$ s^{-1}, this values is equal to the ($\Delta\frac{1}{T_2}$) values obtained from 2D-ELDOR

simulations (Table 2-3 and Table 2-4), consistent with relaxation by collisional exchange and negligible dipolar contribution.[48]

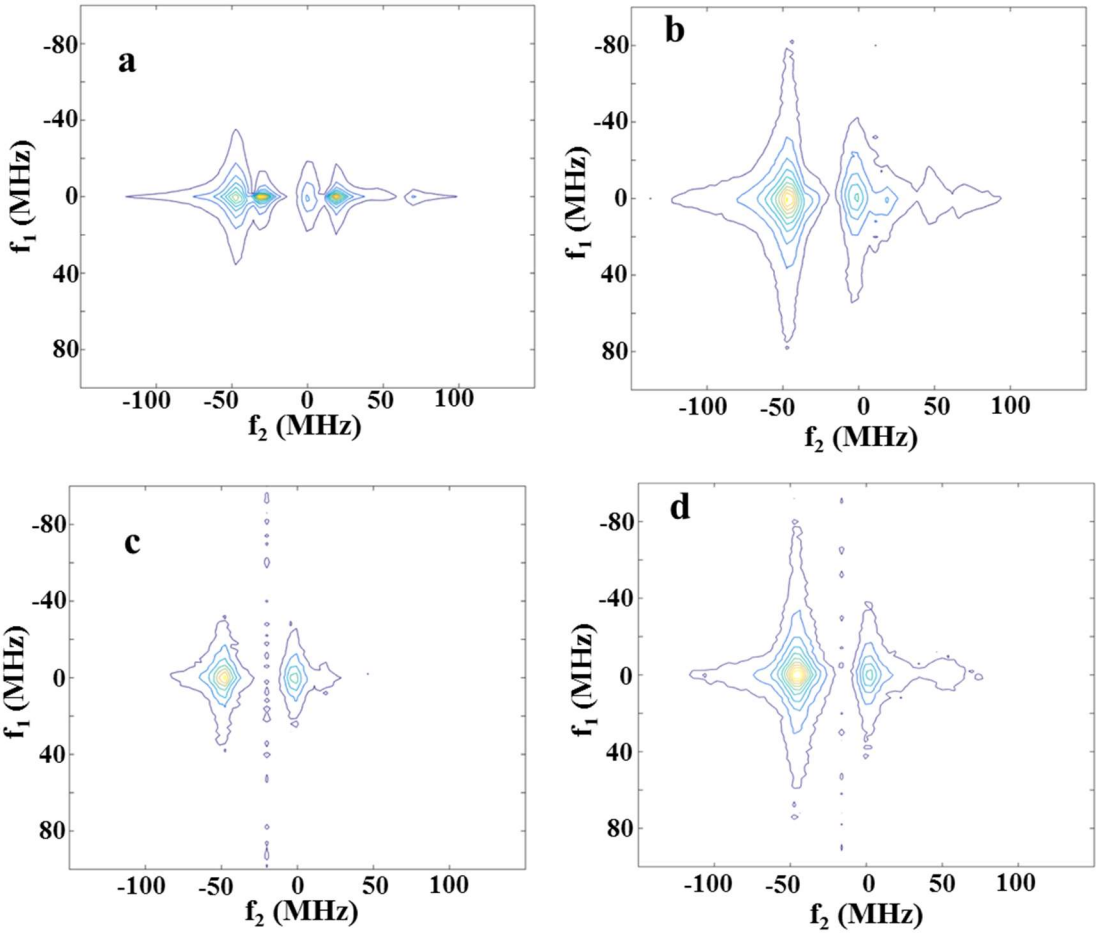

Figure 2-13: Effect of nickel ions on 2D-ELDOR spectra of the water and the lipid phase peaks . 2D-ELDOR (SECSY mode) contour plot of TEMPO partitioning between the lipid and water phase at 37 ℃. (a) No nickel (b) 5mM Ni(ClO₄)₂ (c) 5mM Ni (EDDA) and (d) 10mM Ni (EDDA). The 5mM Ni (EDDA) does not broaden the lipid phase (Lα) very much while Ni (ClO4)₂ and 10mM Ni (EDDA) induces significant broadening of the lipid phase (Lα). In the nickel solutions, the water phase is completely broadened out. Simulation results are in the supplement (Figure 2-23 and Figure 2-24)

For TEMPO, the presence of nickel in the water phase also induces broadening of the lipid phase (L_α) signal although much smaller than in the water phase. It has been shown

earlier[48] that the presence of NiEDDA does not affect the saturation behavior of membrane-embedded PC spin labels, e.g. saturation curves in the presence/absence of 30 mM NiEDDA for the 10PC/DMPC system are identical (Figure 2-21 in the supplement). For our system TEMPO/DMPC, however, NiEDDA causes noticeable relaxation enhancement of the lipid phase signal as can be seen also by the cw-ESR power saturation experiments (c.f. Figure 2-22 in the supplement). 2D-ELDOR shows that the T_1 relaxation times of the lipid phase change from 329 ns to 218 ns due to addition of 10mM NiEDDA to the water phase, this corresponds to a substantial relaxation enhancement of $(\Delta\frac{1}{T_1})$ of ~1.5 x 10^6 s^{-1}. This effect cannot be explained by relaxation enhancement resulting from the exchange of TEMPO between the two phases. Indeed, in the slow exchange limit ($k_{ex} \ll \Delta\omega$, where $\Delta\omega$ is the difference in Larmor frequency of TEMPO in the lipid and water phase), as a first order approximation, the relaxation enhancement only depends on the exchange rate. Hence, in the slow exchange limit, the exchange driven relaxation enhancement of the lipid phase should only be weakly (via second order terms) affected by the relaxation time in the water phase. Apparently, these nickel compounds directly enhance the relaxation of TEMPO spins located in the lipid bilayer, similar to the effect of $Ni(ClO_4)_2$ on membrane-embedded PC labels.[48] Interestingly, NiEDDA measurably affects the relaxation of the lipid-partitioned TEMPO molecules while having little effect on tethered PC spin labels. The tethered PC spin labels can only magnetically interact with nickel ions absorbed on the interface. Forming NiEDDA complex prevents this adsorption on surface. The difference between TEMPO and PC labels is that the non-

tethered amphiphilic TEMPO molecules move freer within the lipid bilayer and the bilayer interface. Therefore, we speculate that they are able to interact with NiEDDA molecules located further into the polar area of the interface. For the lipid phase signal, for example, we see the isotropic hyperfine constant (A_{iso}) value about 0.7 G larger than the A_{iso} for TEMPO in hydrocarbons; this indicates that the average location of the TEMPO molecules spans both the polar and non-polar membrane regions. Further, we observe increase in relaxation enhancement compared to NiEDDA (c.f. Figure 2-13) for TEMPO in the lipid phase in the presence of nickel salts such as perchlorate.

Interestingly, the addition of nickel to the water phase causes enhanced T_2 relaxation, i.e., $(\Delta\frac{1}{T_2})$ ~ 2-3 x $(\Delta\frac{1}{T_1})$. This result is surprising as nickel's relaxation enhancement mechanism is largely due to collisional or Heisenberg exchange and not due to dipolar exchange.[48] This has likely to do with the complex interaction dynamics of TEMPO at the membrane interface and needs to be studied further.

2.6.Conclusions

Small probes detectable by ESR have been used to study biological system for many years. Their magnetic parameters, i.e. spin-lattice (T_1) and spin-spin (T_2) relaxation times are very sensitive to the local environment's viscosity, polarity, and the presence of other paramagnetic species. For studying biological systems, ESR spectral resolution is crucial since it allows for simultaneous observing and analyzing multiple spectral components, which are otherwise overlapped and difficult to interpret. In this study, we have shown results obtained by the 2D-ELDOR (Two-Dimensional Electron-Electron

Double Resonance) technique with our novel 95GHz High Field High Power Pulse ESR spectrometer. As the model system, we used the partitioning of a nitroxide spin label (TEMPO) between the lipid and aqueous phases of the model membrane. By combining the benefits of high field (HF) ESR with two-dimensional (2D) ESR, we have achieved spectral resolution, which was not be achieved by either HF-ESR or 2D-ESR alone. We demonstrate the complete separation of ESR signals from these two phases and show how our recent method (full Sc-) of 2D data analysis[92] is used to extract motional dynamics parameters and relaxation times in each phase. It allowed us to study the effect of paramagnetic relaxants such as nickel and oxygen on the relaxation of the spin probe in each phase, as well as the subtle effects of the presence and the phase state of the lipid on the probe molecules in the water phase. Importantly, for the first time, we report here report a direct observation of exchange due to small molecule partitioning between the lipid and water phase by ESR.

2.7.Supplementary Information

2.7.1.Spectrometer upgrades

We have upgraded the fast high-power modulator that controls the output of the high power EIK (extended-interaction klystron) amplifier to both significantly reduce electron beam turn-off timing jitter and to stabilize output power. In order to reduce time uncertainty in the pulse cutoff, we revised the modulator section internal fast logic with a design upgrade of the timing control from triggered- to gated-mode. By using an external gating signal of 1ns resolution and less than 100 ps jitter to replace the modulator internal timing network, and appropriate control scripting to assure a minimum modulator settling time, we eliminated the ca 45ns turn-off timing uncertainty associated with the prior fixed modulator "on" interval of 1 μs. This modification decisively eliminated modulator timing as a significant dead time contributor, reducing spectrometer dead time from approximately 50ns to an initially verified value of approximately 30 ns, attributable exclusively to waveguide and resonator ring down times. To further reduce the dead time to ca 25 ns, we have added system control scripting within the Python based spectrometer operating software to enable off-field baseline collection for subtraction during subsequent data processing. Finally, we have implemented instrumentation for direct real-time observation of the mode vector magnitudes, an improvement that facilitates rapid operator waveguide and resonator experimental setup for minimum cross-polarized mode generation and, consequently, dead time. It is anticipated that work currently underway for improved ring down and

bridge reflection damping, and reduction of cross-polarized mode generation will in the near-term permit further reduction of spectrometer dead time to less than 15ns.

2.7.2.Determination of the 90° time (Calibration of B_1)

The power of the microwave pulse (B_1) was calibrated by observing the intensity of the ESR spectrum with pulse length (Figure 2-14). This gives us pulse length required to obtain a magnetization flip of $\frac{\pi}{2}$, π, and $\frac{3\pi}{2}$. The pulse length required to obtain a $\frac{\pi}{2}$ flip for our spectrometer is around 5-6 ns, this corresponds to a B_1 of around 16-18 ns with our current set up. We showed that B_1 can be further improved up to 4 times by dielectric loading - the results will be described elsewhere. The nitroxide spectrum in the fast motional limit has a spectral spread of about ~50G (c.f. Figure 2-7) and the B_1 of 16-18 G is enough to obtain near complete coverage of the entire nitroxide spectrum in this motional regime.

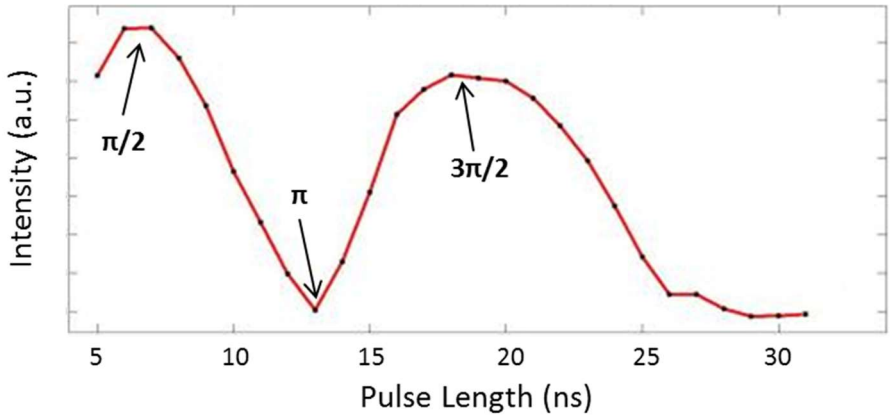

Figure 2-14: Calibration of pulse power. B_1 calibration experiments were carried out with 2mM Tempo in Di Butyl Phthalate (DBPh), the above curve reflects the changes in the intensity of the central line of the three line 1D spectra of the spin label TEMPO. The π/2 pulse length is between 5-6 ns.

2.7.3.Full Sc- Fitting

The advantage of performing the full Sc- fitting is twofold: (a) better optimization of motional parameters due to the simultaneous fitting of real and imaginary parts of the Sc- spectrum, and, (b) pure absorption spectra used to obtain the relaxation parameters can be calculated from the full Sc- fit. To perform this fitting, the magnitude mode (magnitude of the real and imaginary parts) spectra of each component were simulated to obtain reasonable seed magnetic and motional parameters for the Full Sc- fit. Then the real and imaginary parts of the experimental spectra were fit using the Full Sc- program by keeping the seed magnetic and motional parameters constant but by varying the phase factors (a2, b1, and b2). Finally, all the parameters were simultaneously varied to obtain the most rigorous fit. It is to be noted that in the final step only small variations in the simulation parameters were required. The full Sc- program can be used to obtain the theoretical pure absorption spectra from the magnitude mode spectra; the pure absorption spectra will be used to obtain the T_2 relaxation times of the sample.

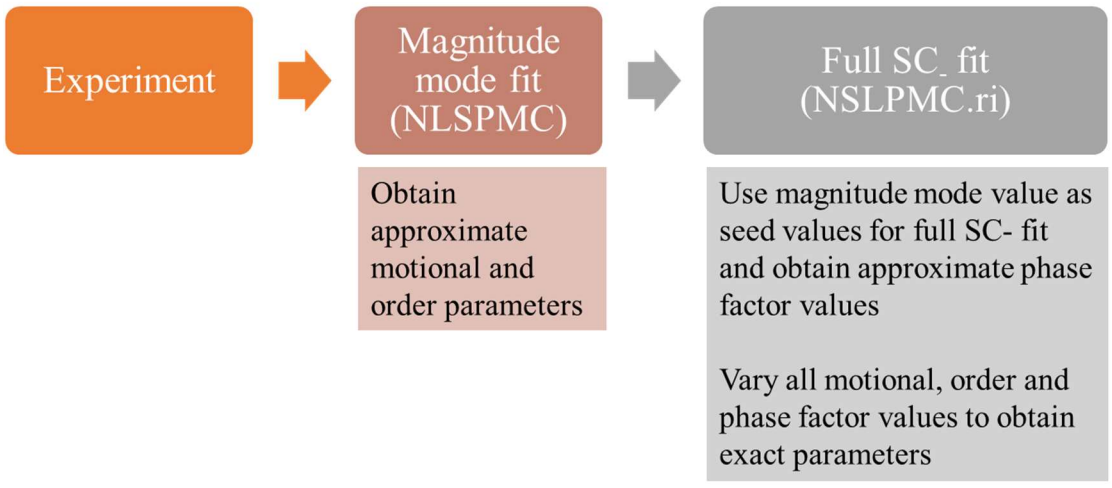

2.7.4.END vs HE

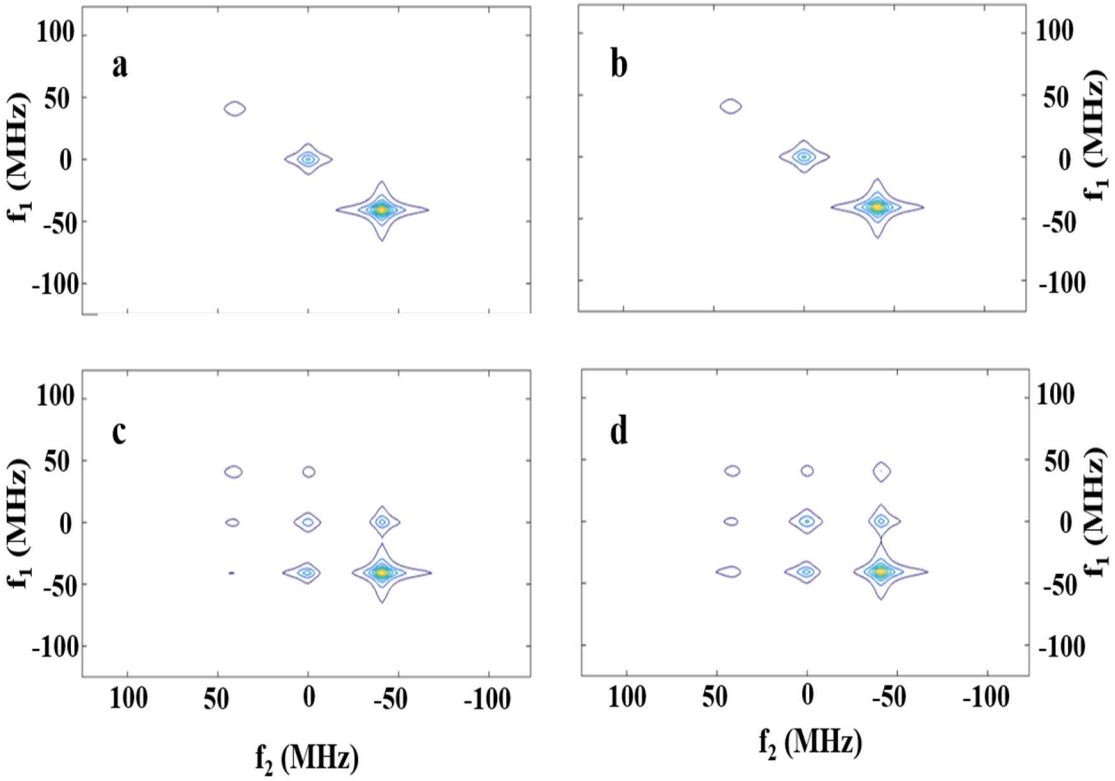

Figure 2-15: Development of END and HE cross peaks in 2D-ELDOR. A contour plot of a 95 GHz 2D-ELDOR simulation obtained for a nitroxide spin label with the following parameters: $\bar{R}$=8.91 x 10^9 s^{-1}, Δ_g= 0.26, Residual T_2 = 95ns, g_{xx} = 2.0087, g_{yy} = 2.0056, g_{zz}= 2.00224 and a_{xx} = 5.0 G, a_{yy} = 5.0 G, a_{zz}= 33.5 G. (a) W_{END}= 1.74 x 10^6 s^{-1}, no HE, T_m = 50 ns; (b) W_{HE} = 1.74 x 10^6 s^{-1}, no END, T_m = 50 ns; (c) W_{END}= 1.74 x 10^6 s^{-1}, no HE, T_m = 800 ns; (d) W_{END}= 1.74 x 10^6 s^{-1}, no END, T_m = 800 ns. In the case of the cross peaks due to END mechanism (plot c), the cross peaks developed for $\Delta m_I = \pm 2$ are negligible while for the case of Heisenberg exchange these cross peaks are well developed (plot d).

2.7.5.Pure Absorption Spectra for the Lipid and Water phases

The pure absorption spectrum is generated "theoretically" as the SECSY mode 2D-ELDOR simulation can be easily obtained using the NLSPMC.ri program. The pure absorption 2D-ELDOR SECSY mode spectra for the two components (water and lipid) obtained by the procedure described above are shown in Figure 2-16 and Figure 2-17.

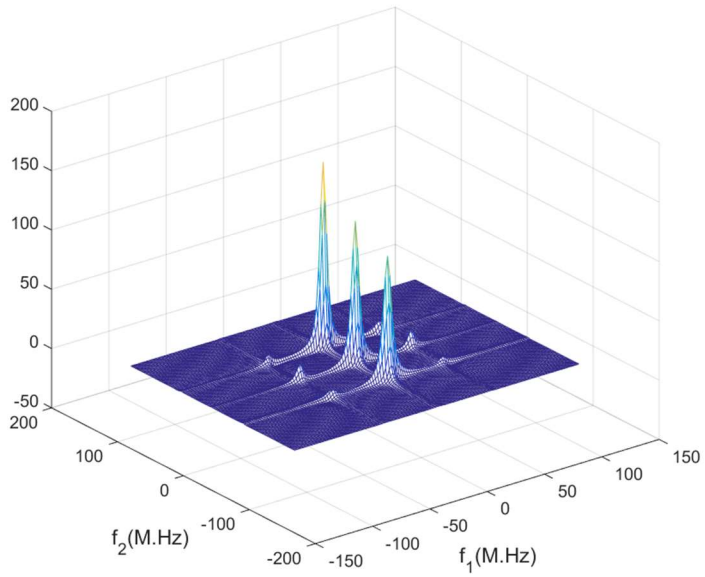

Figure 2-16: The pure absorption 2D-ELDOR (SECSY mode) spectra of TEMPO in water at 17℃, T_m = 50ns

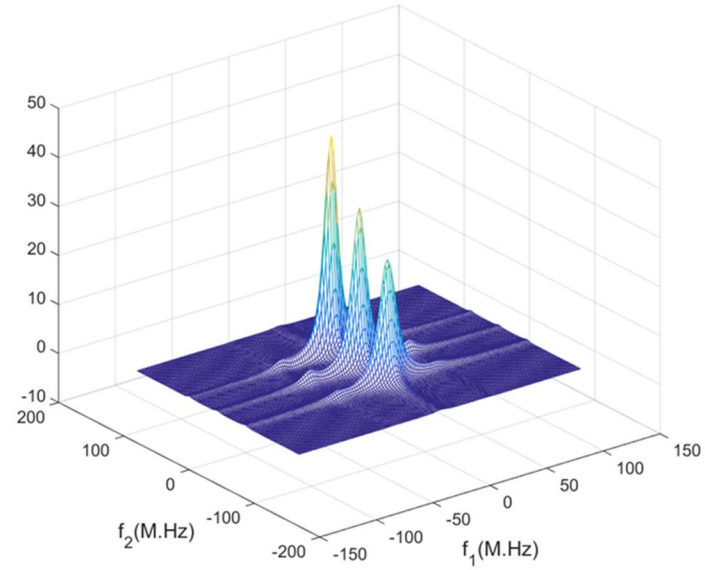

Figure 2-17: The pure absorption 2D-ELDOR (SECSY mode) spectra of TEMPO in the lipid phase (L_α) at 37℃, T_m = 50ns

2.7.6.Effect of Oxygen (broadening of the water phase)

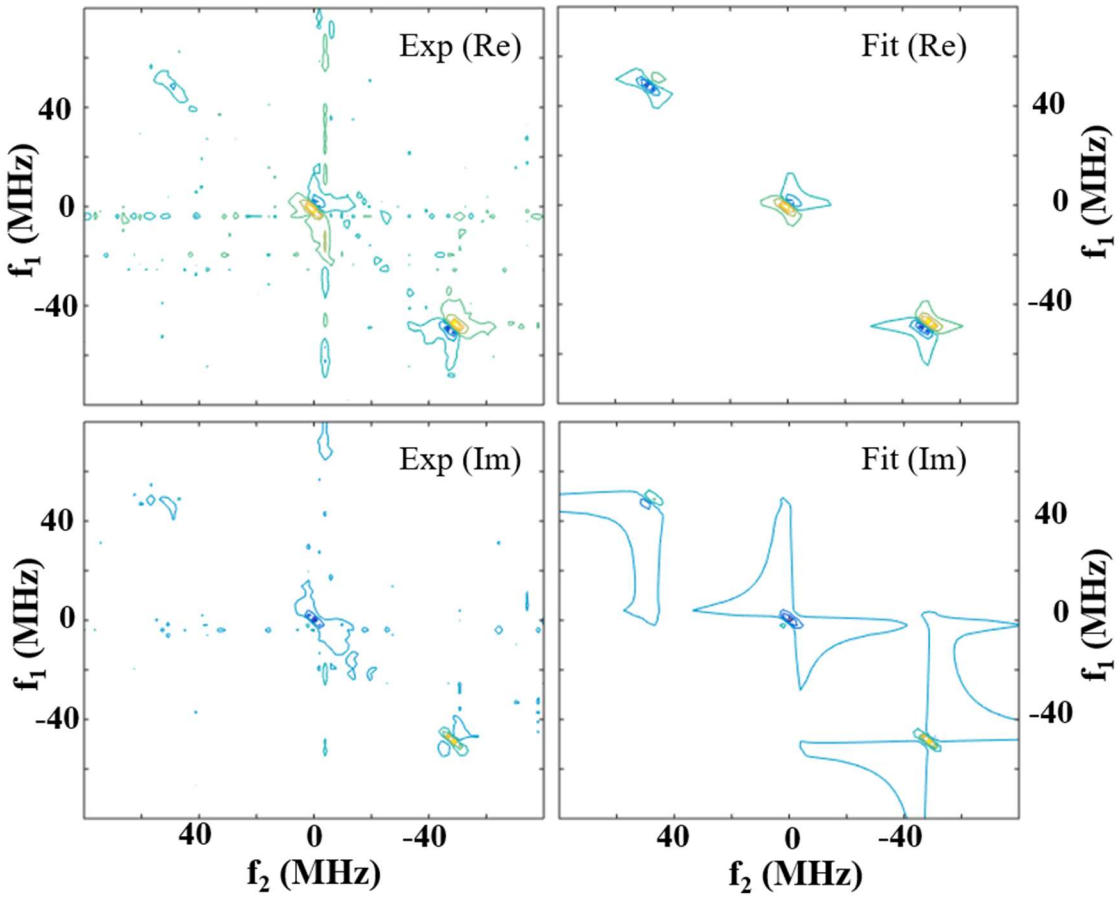

Figure 2-18: The 2D-ELDOR experiment and simulation of 0.5mM TEMPO in water at 95 GHz at T_m = 50ns under deoxygenated conditions. Both the real (Re) and imaginary (Im) parts of the spectra are shown.

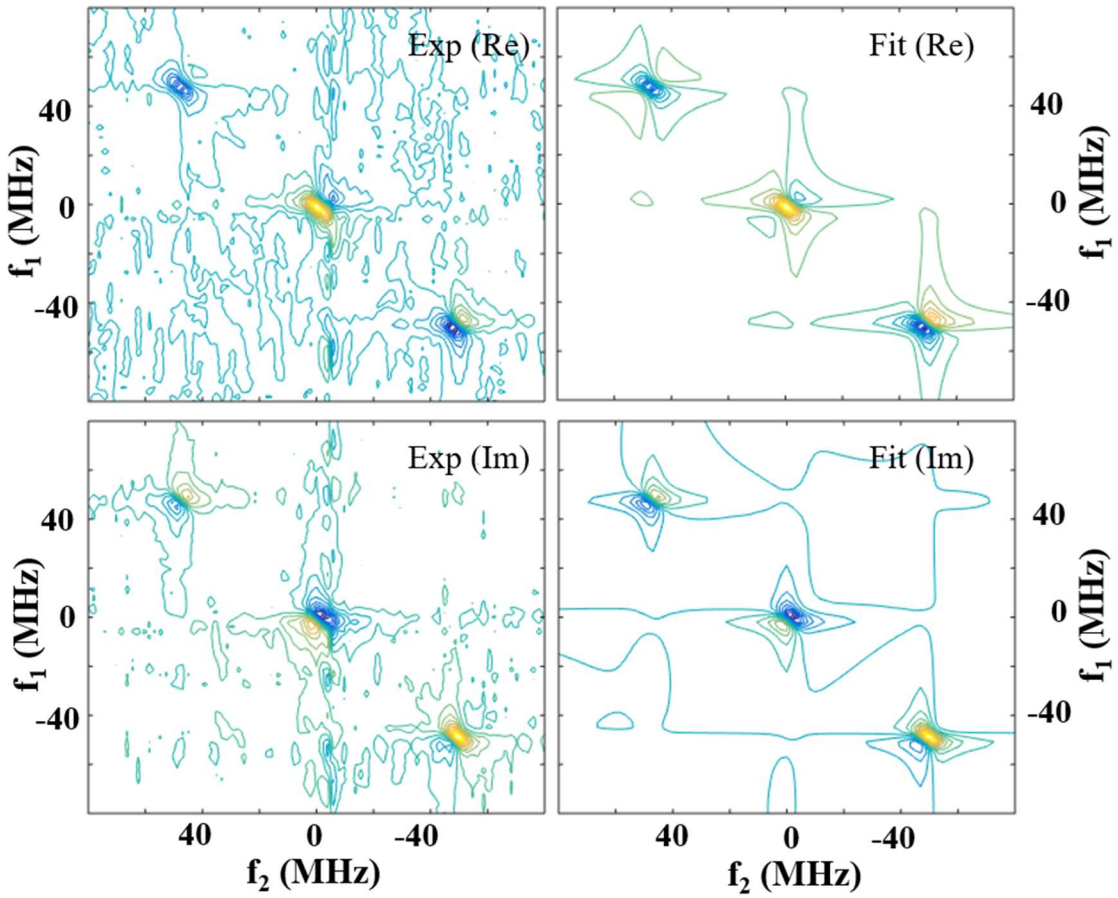

Figure 2-19: The 2D-ELDOR experiment and simulation of 0.5mM TEMPO in water at 95 GHz at T_m = 50ns under oxygen saturated conditions. Both the real (Re) and imaginary (Im) parts of the spectra are shown.

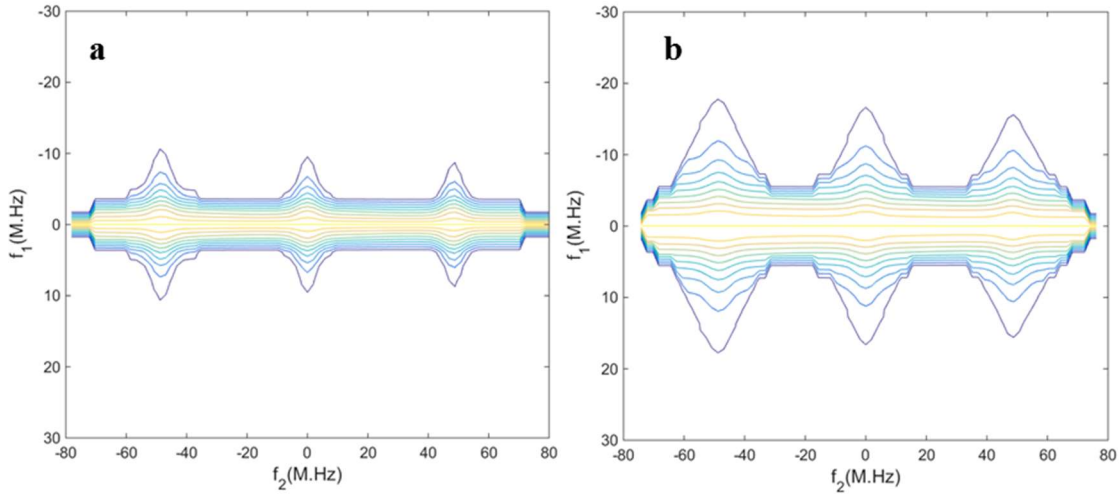

Figure 2-20: The 2D-ELDOR (SECSY mode) spectrum of 0.5mM TEMPO in water at 95 GHz, (a) Deoxygenated and (b) Oxygen Saturated. The spectrum is shown as normalized contours, i.e., the spectrum along the f_2 dimension is divided by the intensity of spectrum at the corresponding f_1=0 value.

Table 2-2: The relaxation times for 0.5mM TEMPO in bulk water at 95 GHz under oxygenated and deoxygenated conditions.

Conditions	T_2 **(ns)**	$\overline{T_2}$ **(ns)**	T_1 **(ns)**
Oxygen saturated	61, 58, 54	57.45	113
Deoxygenated	105, 97, 88	96.62	608
$\frac{1}{T_{oxygen}} - \frac{1}{T_{deoxygenated}}$		**7.06 x 10^6 s^{-1}**	**7.20 x 10^6 s^{-1}**

Note: At 17 C, the concentration of oxygen is ~1.5mM in water.

2.7.7.Nickel and Collisional Exchange in the water phase

Table 2-3: The relaxation times for 2mM TEMPO in water (largely interbilayer water) at 17°C at 95 GHz with the water phase containing different concentrations for Nickel.

Conditions	T_2 (ns)	$\overline{T_2}$ (ns)	T_1 (ns)
5mM Ni	61, 58 , 54	57.49	111
0mM Ni	98, 90, 82	89.69	375
$\frac{1}{T_{5mM\ Ni}} - \frac{1}{T_{0mM\ Ni}}$		**6.24 x 10^6 s^{-1}**	**6.34 x 10^6 s^{-1}**

Note: For the water phase, the exact nature of the nickel counter ion is not important, the values presented above are for Nickel Perchlorate [$Ni(ClO_4)_2$].

Table 2-4: The relaxation times for 2mM TEMPONE in water at 17°C at 95 GHz with the water phase containing different concentrations for Nickel.

Conditions	T_2 (ns)	$\overline{T_2}$ (ns)	T_1(ns)
0mM Ni	127, 98, 76	100.3	254
2mM Ni	95, 79, 65	79.7	161
5mM Ni	57, 49, 43	49.7	72
$\frac{1}{T_{2mM\ Ni}} - \frac{1}{T_{0mM\ Ni}}$		**2.59 x 10^6 s^{-1}**	**2.27 x 10^6 s^{-1}**
$\frac{1}{T_{5mM\ Ni}} - \frac{1}{T_{0mM\ Ni}}$		**10.17 x 10^6 s^{-1}**	**9.95 x 10^6 s^{-1}**

2.7.8.Saturation Curves for Nickel

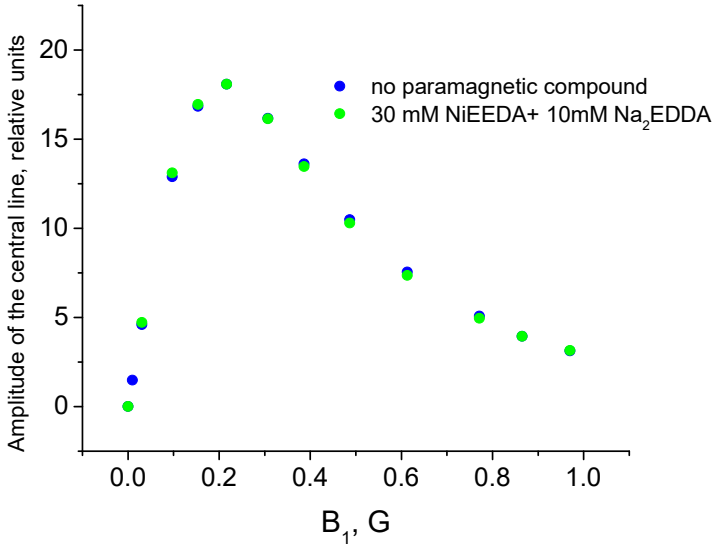

Figure 2-21: The saturation curve of 10-PC spin label in DMPC. This spin label does not undergo any enhancement in relaxation due to the addition of Nickel EDDA to the water phase.

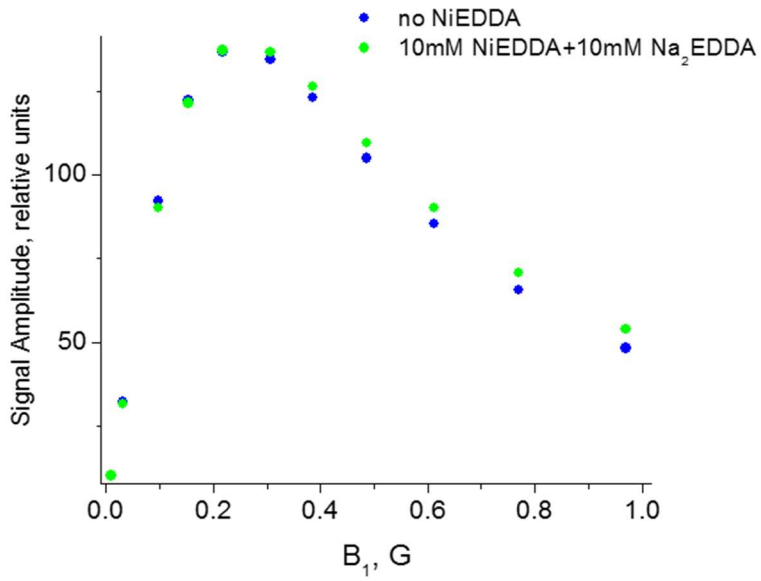

Figure 2-22: The saturation curve of TEMPO spin label in DMPC. TEMPO shows enhancement in relaxation due to the addition of Nickel EDDA (even at 10mM) to the water phase.

2.7.9.Effect of Nickel counter ion in the lipid phase

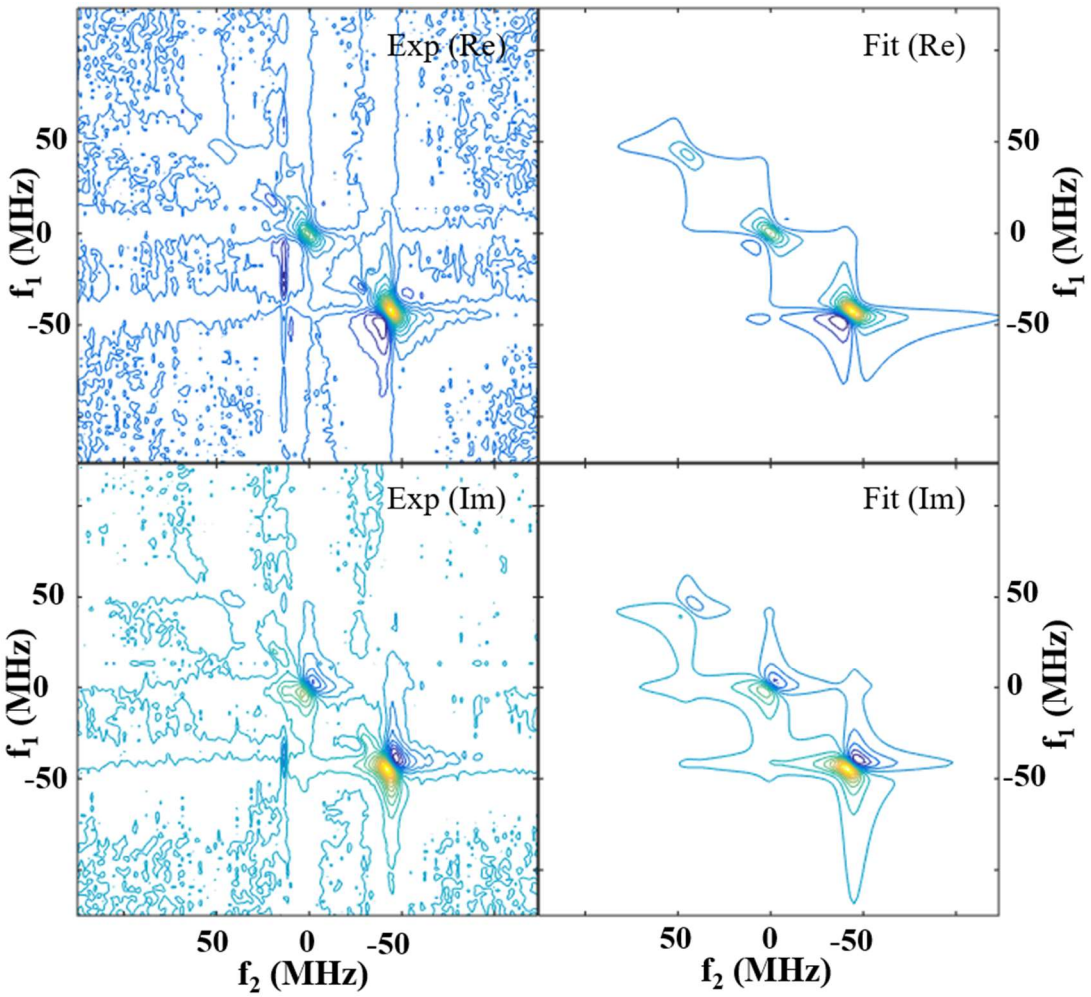

Figure 2-23: The experimental (Exp) and simulated (Fit) 2D-ELDOR spectrum of TEMPO in the lipid phase with 5mM Nickel Perchlorate in the water phase at 37°C; Tm = 20ns.Both the real (Re) and imaginary (Im) parts of the spectra are shown.

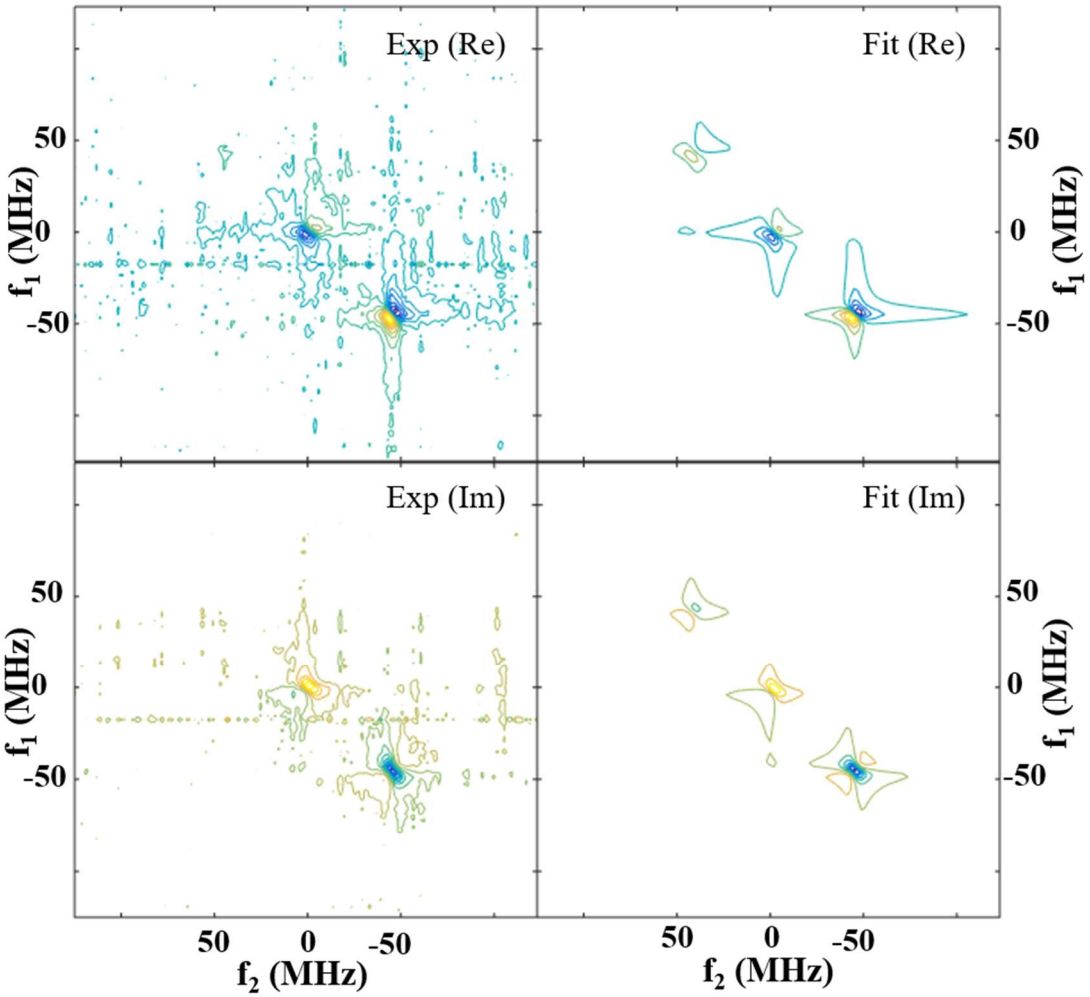

Figure 2-24: The experimental (Exp) and simulated (Fit) 2D-ELDOR spectrum of TEMPO in the lipid phase with 5mM Nickel EDDA in the water phase at 37℃, T_m = 20ns. Both the real (Re) and imaginary (Im) parts of the spectra are shown.

2.7.10. T_1 Relaxation Times

The T_1 relaxation times measured on the different samples are in Table 2-5 and Table 2-6. The T_1 relaxation times are affected by the phase and the presence of paramagnetic relaxants.

Table 2-5: The spin-lattice relaxation times (T_1) estimated for TEMPO in different conditions

Sample	***Phase***	***Conditions***	***T_1 (ns)***
0.5 mM TEMPO	*b. w.*	*Deoxygenated, 17 ℃*	*608*
0.5 mM TEMPO	*b. w.*	*Air (~20% Oxygen)*	*258*
0.5 mM TEMPO	*b. w.*	*100% Oxygen (Oxygen Saturated), 17 ℃*	*113*
*2 mM TEMPO**	*i.w. + b.w.*	*Deoxygenated, 17 ℃*	*375*
*2 mM TEMPO**	*i.w. + b.w.*	*Deoxygenated, 17 ℃, 5mM Ni^{2+}*	*111*
*0.8 mM TEMPO**	*i.w. + b.w.*	*17 ℃*	*469*
*0.8 mM TEMPO**	*i.w. + b.w.*	*37 ℃*	*433*
*TEMPO in DMPC***	*Lipid (L_α)*	*37 ℃, 0.8 mM TEMPO in water phase*	*318*
*TEMPO in DMPC***	*Lipid (L_α)*	*37℃, 2mM TEMPO in water phase*	*329*
*TEMPO in DMPC***	*Lipid (L_α)*	*37℃, 2mM TEMPO in water phase in Air (~20% Oxygen)*	*168*
*TEMPO in DMPC***	*Lipid (L_α)*	*37℃, 5 mM NiEDDA, 2mM TEMPO in water phase*	*255*
*TEMPO in DMPC***	*Lipid (L_α)*	*37℃, 10 mM NiEDDA, 2mM TEMPO in water phase*	*218*
*TEMPO in DMPC***	*Lipid (L_α)*	*37℃, 5mM Nickel Perchlorate, 2mM TEMPO in water phase*	*148*

i.w. = interbilayer water; b.w. = bulk water

***The exact concentration of TEMPO in the lipid phase depends on the sample, depending on the water present in the sample and the TEMPO concentration in the water phase.*

Table 2-6: The spin-lattice relaxation times (T_1) estimated for TEMPO in organic solvents

Sample	***Phase***	***Conditions***	***T_1 (ns)***
0.5mM TEMPO in Hexadecane	*Organic*	*Deoxygenated, 20 ℃*	*193*
0.5mM TEMPO in Hexadecane	*Organic*	*100% Oxygen, 20 ℃*	*47*

2.7.11.Line Broadening by Convolution

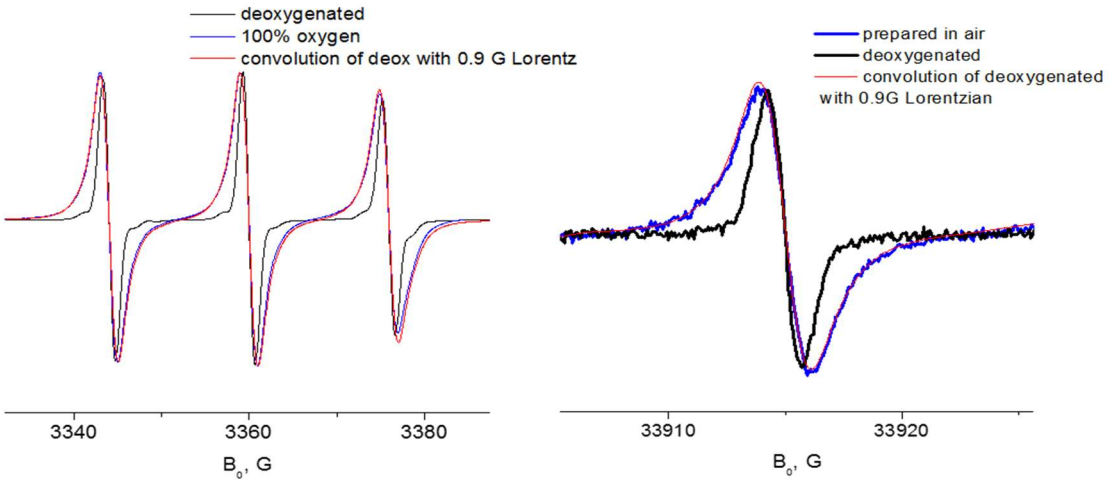

Figure 2-25: Line broadening measured by cw-ESR. Left: The cw-ESR spectrum of TEMPO in DMPC at 36 ℃ measured at 9.4 GHz. Right: The cw-ESR spectrum of TEMPO in hexadecane at 17 ℃ measured at 95 GHz, only the central peak of the spectrum is shown. This figure shows that the Lorentzian convolution is an effective method to assess the linewidth broadening.

The deoxygenated spectrum (S_0) is convolved with the Lorentzian $[L(t-\boldsymbol{\tau};\Gamma)]$ function and fit to the oxygen broadened spectrum (S_r). The fitting with Lorentzian function gives us the extent of broadening (Γ).

$$S_r(t) = \frac{1}{\pi}\int_{-\infty}^{\infty} S_0(\boldsymbol{\tau})\, \boldsymbol{L}(t-\boldsymbol{\tau};\Gamma)\, d\boldsymbol{\tau}$$

As the extent of broadening (Γ) is directly proportional to the T_2 relaxation as discussed earlier. $\Delta\frac{1}{T_2} = 15.25\ x\ \Gamma\ (\text{in Gauss})\ x\ 10^6\ s^{-1}$

It is important to note that, as the additional broadening is dependent only on nature (e.g. oxygen, nickel) and concentration of the relaxant, it is field independent i.e., the broadening observed is exactly the same at 9 and 95 GHz ESR spectroscopy (Figure 2-25).

CHAPTER 3 : ESR STUDY OF NANODOMAINS IN FOUR-COMPONENT MODEL MEMBRANES

3.1.Introduction

Cell membranes contain more than 1000 different lipid constituents[29] that are required to carry out an array of complex cellular functions. These lipids need to be organized (e.g. separated into ordered and disordered domains) so as to achieve its varied functionality including signaling and transport. However, the sizes of these separated domains are subject to speculation, and this is of interest for the entire biomedical community.[24,25,130–132] The current understanding is that the sizes of these domains are nanoscopic and therefore not easily studied by florescence imaging techniques. We have extensively studied a wide range of cellular membrane domains[3,18–20,133] using Electron Spin Resonance Spectroscopy (ESR). However, the study of 1000+ lipids in their natural cellular membranes is much too complicated and hence simplified model systems consisting of three lipid components (high melting lipid, low melting lipid, and cholesterol) have been extensively used to model a cell membrane. The ordered domains (L_o-domains) are rich in high melting (hi-T_m) lipids and cholesterol while the disordered domains (L_d-domains) are rich low melting (Low-T_m) lipids. In some studies, these ordered domains are also referred to as "lipid-rafts". Moreover it is difficult to prepare model membranes in which the bilayer asymmetry (i.e., different inner and outer leaflet) can be realized, and hence typically only the outer leaflet (rich in phosphocholines[134]) is modeled. Such a model system has been used extensively by researchers.[29,50,52]

3.1.1.Modeling the nanoscopic domains

The Feigenson group at Cornell has shown that the lipid compositions containing DSPC/POPC/Chol form nanoscopic domains while DSPC/DOPC/Chol form macroscopic domains.[135,136] In the case of these two lipid systems, the replacement of a low melting lipid, DOPC by another low melting lipid, POPC leads to a size scale transition from macroscopic to nanoscopic domains. Therefore, the replacement of DOPC by POPC, while holding the DSPC and cholesterol compositional ratios constant, is an important compositional sequence to study this size scale transition (Figure 3-1). At certain intermediate compositions of DSPC/POPC/DOPC/Chol, highly-patterned, "modulated" phase domains form.[136]

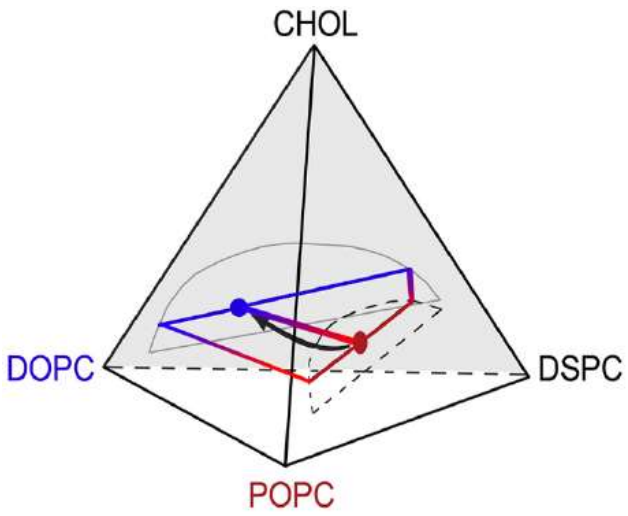

Figure 3-1: The phase diagram of the DSPC/DOPC/POPC/Chol system. The black arrow indicates the DOPC/POPC trajectory that is being studied[137].

To study such a range of compositions the variable 'rho (ρ)' is defined which indicates the relative mole fraction of the DOPC present in the sample as shown in Equation 3-I. A rho (ρ) value of 1 indicates that the low melting lipid is completely DOPC

(macroscopic domains), while a value of 0 indicates that the low melting lipid is completely POPC (nanoscopic domains).

$$\rho = \frac{\chi(DOPC)}{\chi(POPC) + \chi(DOPC)} \qquad \text{3-I}$$

The size of these nanoscopic domains at ρ=0 composition has been found to be ~7nm.[138] Even though this system has been well studied, there are many questions that still need to be answered. Specifically, are there any significant changes in the lipid phase behavior that are the result of the size-scale transition? Moreover, in this system, are they any domain size-dependent effects (such as extent of boundary or interface) which need to be considered (particularly in the nanoscopic regions)?

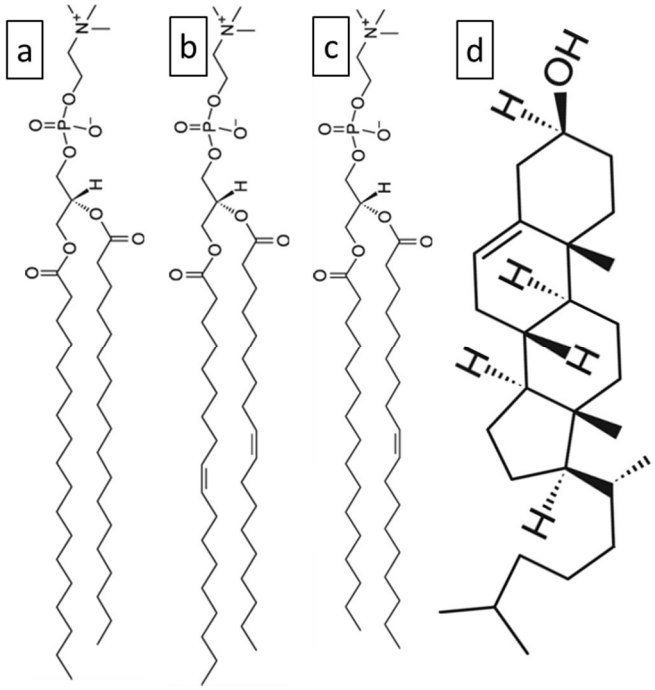

Figure 3-2: The structure of the lipids used in this study: (a) DSPC: 1,2-distearoyl-sn-glycero-3-phosphocholine; (b) DOPC: 1,2-dioleoyl-sn-glycero-3-phosphocholine; (c) POPC: 1-palmitoyl-2-oleoyl-sn-glycero-3-phosphocholine; (d) Cholesterol

ESR spectroscopy was used to study the transition to the nanoscopic domains from the macroscopic domains i.e. by replacing POPC with DOPC. The structure of the lipids used in this study is shown in Figure 3-2. ESR spectroscopy measures the ensemble average of all the electron spin labeled lipids that are present in the sample. ESR is therefore independent of the domain size[139] and can be used to study both the nanodomains as well as the macrodomains.

To study membrane systems, there are many lipid based spin probes available (such as 5-PC, 16-PC, cholestane). For this study, 16-PC was chosen as the preferred spin label, as it has nearly equal partitioning into both the L_o and L_d domains[10,19] with distinct ESR spectra. This probe (16-PC) has a nitroxide group (containing the unpaired electron) located on the 16-position of an acyl chain of the probe (Figure 3-3).

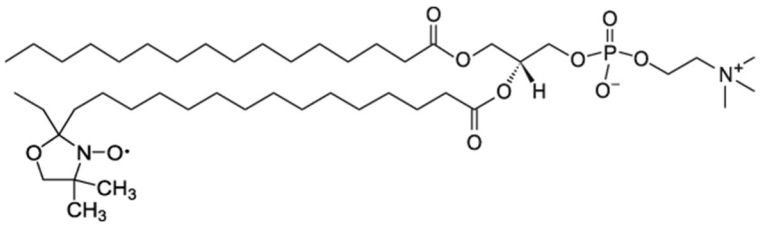

Figure 3-3: Structure of a 16-PC molecule (1-palmitoyl-2-stearoyl-(16-doxyl)-sn-glycero-3-phosphocholine).

Given that an ensemble average of all the spins present in the sample are measured, the spectra obtained ($\vec{S}$) is proportional to a linear combination of the spectra ($\vec{S}_i$) of the 16-PC in different chemical and physical environments. In equation 3-II, $\vec{S}_i$ represents the individual spectral component corresponding to the i^{th} environment and the x_i represents the fraction of the spin-labeled lipid experiencing that environment.

$$\vec{S} = \sum_i x_i * \vec{S}_i \qquad \text{3-II}$$

This equation is valid when there are no rapid exchange effects between the environments in the time scale of the measurement. It is important to note that the time scale of the cw-ESR experiment is faster than lipid translation (for 16-PC), so we do not observe effects of the (slower) lipids transitioning between the two neighboring domains[3]. Lipid systems for which the phase diagram is well understood (c.f. Figure 3-1), it is possible for us to determine the "tie-lines" in a two phase coexistence region, for which the mole fractions of the L_o and L_d phase can be determined on the basis of the Lever Arm Rule, (i.e. the fraction of each phase is determined by its distance from the phase boundary). This is possible because the partition coefficient (K_p) is constant as we restrict compositional changes to remain on the tie-line.

3.2.Experimental

3.2.1.Sample Preparation:

3.2.1.1. Coexistence samples for 9 GHz spectra

The preparation for these samples is described elsewhere.[137,140] In summary, two stock solutions, A and B (with 40.4 μM total lipid concentration) containing (A) DSPC/POPC/Chol and (B) DSPC/DOPC/Chol in a ratio of 0.39/0.39/0.22 respectively were prepared in chloroform. Then, 0.3 mole-percent of 16-PC was added to these stock solutions as the spin labeled lipid probe. In this limit we have about 1 spin labeled lipid for about 300 non spin labeled lipids. This concentration was chosen, as it was sufficient

for obtaining a good signal to noise ratio (SNR), while at the same time minimizing the intermolecular spin-spin interactions occurring at high spin label concentrations. These two stock solutions were mixed in different ratios to obtain the desired DSPC/POPC/DOPC/Chol ratio, i.e., to obtain the rho 0.2 solution, 80% of solution A (POPC mix) was added with 20% of solution B(DOPC mix). The desired lipid mixture solution was evaporated under a steady flow of compressed nitrogen gas and then completely dried under high-vacuum in a desiccator for about 8 hours. About 0.4 ml of milliQ water was added to the dried lipid solution and was hydrated for one hour at ~47 ℃ with occasional vortexing every 5-15 minutes. The samples were then transferred to 2ml centrifuge tubes and centrifuged at 14,000 g and 4 ℃ for 30 mins. The supernatant was carefully removed, leaving behind approximately 80 µl of residual water plus the lipid pellet. The pellets were re-suspended in the remaining water (~80 µl) and transferred to an ESR capillary tube. The sample was finally re-pelleted at 3,300 g and the supernatant was removed, a small layer of water (~1-2 µl) was left behind to prevent oxidation of the sample. The capillary tubes were carefully sealed to prevent evaporation and oxidation. For 9 GHz measurements, the total weight of the lipids was approximately 2mg.

In the case of Chol 26, the process for Chol 22 is repeated except that the ratio of DSPC/low-melting lipids (DOPC/POPC)/Chol is different. The cholesterol concentration is fixed at 26 mole percent. The two stock solutions containing (A) DSPC/POPC/Chol and (B) DSPC/DOPC/Chol in the ratio of 0.37/0.37/0.26 were mixed together to obtain the desired lipid composition. To obtain the pure phase spectra at the end of the tie-lines, the lipid composition was determined from the phase diagram. The

lipids were mixed in these pre-determined ratios of the four components (DSPC/POPC/DOPC/Chol) in chloroform and 0.3 mole percent of 16-PC was added.

3.2.1.2. Coexistence samples for 95 GHz spectra

Table 3-1: Ratios given in DSPC/DOPC/POPC/chol, along the Chol 22 tie-line

rho-value	**Coexistence Sample**	**L_o from Tie-line**	**L_d from Tie-line**
0	39/0/39/22	55/0/18/27	10/0/79/11
0.1	39/4/35/22	56/0.5/16/27.5	10/7/72/11
0.2	39/8/31/22	57/1/14/28	10/13/63/11
0.5	39/20/19/22	60/2.5/9/28.5	10/40/39/11
1	39/39/0/22	65/5/0/30	10/79/0/11

The lipids for the L_o, L_d and Chol 22 line were mixed in the pre-determined ratio of the four components (Table 3-1) in chloroform and 0.3 mole percent of 16-PC was added. The lipids were dried under nitrogen flow, vacuum desiccated and hydrated as described above for the Chol 22 (9 GHz sample preparation). The samples were then pelleted at 13,000g and 4°C for 30 mins and the supernatant carefully removed. The lipid pelleted (~6 mg and ~10 µl) was then carefully transferred into a 25 mm etched (concave surface) quartz coverslip. A flat quartz coverslip was used to cover the sample. The two coverslips were held together and sealed by a thin layer of vacuum grease (Dow Corning), the details of this sample holder have been described earlier by Barnes et al.[141] As described earlier, for experiments performed at 9 GHz the samples were sealed in glass capillaries; earlier studies have shown that the geometry of the sample holder does not affect the ESR spectrum.[14]

3.2.2.Spectral Acquisition and Processing:

3.2.2.1. 9 GHz measurements:

Samples were left to equilibrate in the sample holder capillaries for at least 1hr before the ESR measurements. The 9 GHz measurements were collected on a commercial Bruker ELEXSYS (E500) CW-ESR spectrometer at room temperature (~293-297 K) using a modulation amplitude of 0.5 G. To obtain sufficient signal to noise ratio (SNR), 16 scans of the experiment were collected and averaged. The phasing for the experimental spectra was automatically performed by the spectrometer. The spectra were shifted along the magnetic field axis to appropriately align the centers of all the ESR spectra and normalized based on the first integral.

3.2.2.2.95 GHz measurements:

Samples were left to equilibrate in the flat sample holders for at least one hour before the ESR measurements. The 95 GHz measurements were collected on a home built High Power CW and Pulsed ESR spectrometer[6,83] at room temperature (~296.5 K) using a modulation amplitude of 6G; (this was required as signal strength increases with increase in modulation amplitude). The higher modulation amplitude at 95 GHz is justified, as linewidths are significantly broader. Further, the spectra were carefully checked to ensure no effects of modulation-dependent broadening effects were observed. All the measurements were repeated (between 36-100 scans) and averaged until an appropriate SNR was achieved. In the 95 GHz spectrometer both the '*in-phase*' (I) and '*out-of-phase*' (Q) signals are obtained and needed to be phased. This phasing

procedure was performed to obtain the cw-ESR spectra. The spectra are then normalized and horizontal shifts were performed as in the case of the 9 GHz spectra. The centering of the 95 GHz data is more challenging as it is difficult to identify the center of the L_o and L_d spectra for the high field data (Figure 3-4). The 95 GHz spectra have more complicated line shapes when compared to the 9 GHz data. Further, because of the increased g-resolution, 95 GHz spectroscopy is extremely sensitive to subtle motional and ordering effects.

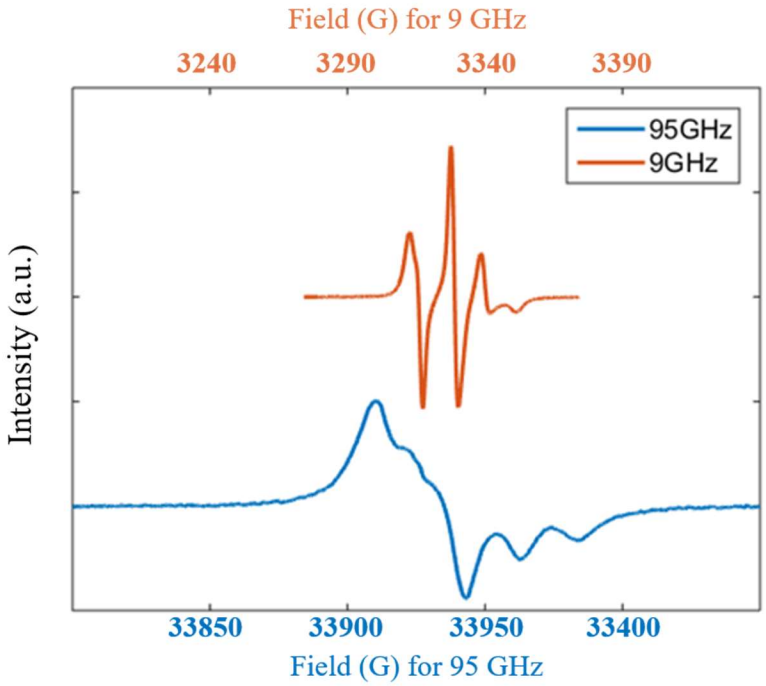

Figure 3-4: A comparison of the 9 and 95 GHz cw-ESR spectra of 16-PC in the L_o phase. The spectral spread of the 9 GHz data is ~55 Gauss while the 95 GHz is ~125 Gauss. This is mainly due to the increased role of the g-tensor at higher field values as is typically the case with 95 GHz.

3.2.2.3.Nonlinear Least Squares Analysis (NLSL)

The NLSL analysis using the Microscopic Order Macroscopic Disorder (MOMD) model was carried out.[96] The version of the NLSL program gives us the following parameters: (a) rotational diffusion rate ($R_\perp$ and $R_\parallel$) and the order parameters (S_0 and S_2). The rotational rate ($R_\perp$) is the rotational rate of the radical around an axis perpendicular to the mean symmetry axis (also the direction of the preferred orientation for the radical) for the rotation.[102] The NLSL also gives us the $R_\parallel$ (or the motion about the symmetry axis) but the 9 GHz spectra is not very sensitive to this parameter and is discussed in detail later. The rotational motion represents the motion of the spin label nitroxide attached to the acyl chain of the lipid molecule.[15,79] The order parameters (S_0 and S_2) gives us the measure of the ability of the nitroxide molecule to deviate from the membrane normal and the non-axiality of this deviation. A large order parameter value implies that the motion of the spin label is restricted (i.e., greater order). An order parameter of zero implies that all the spins are oriented randomly with respect to the membrane normal. NLSL also gives us the fraction of the components (i.e., in this case the fraction of the L_o and L_d phase) present along with a χ^2 residual for the fit.

3.2.2.4.L_o Fraction (α) based on fitting the coexistence spectra

Even though the NLSL analysis is useful for obtaining the motional parameters and the relative ratios of individual components in a multicomponent system, the analysis is computationally expensive and tedious when the primary information that is needed is the fraction of the L_o component. This information can easily be obtained by a tie-line

analysis fitting and hence a MATLAB® based method was developed to obtain the fraction of L_o phase. The co-existence point in the phase diagram for the given composition lies on a tie-line, and hence the spectrum can be expressed as a linear combination of those of the two end points using the equation 3-III.

$$\overrightarrow{\boldsymbol{S_{Co}}}(\rho) = \alpha(\rho) \times \overrightarrow{\boldsymbol{S_{Lo}}}(\rho) + (1-\alpha(\rho)) \times \overrightarrow{\mathbf{S_{Ld}}}(\rho) \qquad \text{3-III}$$

where $\overrightarrow{S_{Co}(\rho)}$, $\overrightarrow{S_{Lo}(\rho)}$, $\overrightarrow{S_{Ld}(\rho)}$ are the ESR spectra of the at the coexistence composition, liquid ordered phase, and liquid disordered phase respectively while α is the L_o fraction.

Here α is the mole fraction of the 16-PC spin probe exhibiting L_o phase behavior and can be estimated by fitting the spectral data. As the phase diagram and tie-lines information are available, the expected L_o fraction can be estimated. Therefore, the K_p values can be easily obtained as follows:

$$K_p = \frac{L_o \; fraction \; expected}{\alpha}$$

It is noted that 16-PC spin probes partitions almost equally (i.e., K_p ~1) between the L_o and L_d phases[10,19,51] while other similar probes (5-PC, 7-PC) favors the L_d phases. However, the partition coefficient is lipid composition dependent, therefore it can vary as we replace POPC with DOPC i.e., as we move from rho 0 composition to rho 1 composition.

3.3.Summary of earlier results: 9 GHz cw-ESR for Chol 22

Earlier, 111 points corresponding to different rho(ρ) values on the Chol 22 line were measured.[137,140] The pure phase (L_o and L_d) spectra for each of these points were either

measured or estimated (based on a linear combination of pure phase spectra on the phase boundary).

$$\overrightarrow{S_{Ld}}(\rho) = \rho \times \overrightarrow{S_{Ld}}(1) + (1-\rho) \times \overrightarrow{S_{Ld}}(0) \qquad \text{3-IV}$$

and

$$\overrightarrow{S_{Lo}}(\rho) = \rho \times \overrightarrow{S_{Lo}}(1) + (1-\rho) \times \overrightarrow{S_{Lo}}(0) \qquad \text{3-V}$$

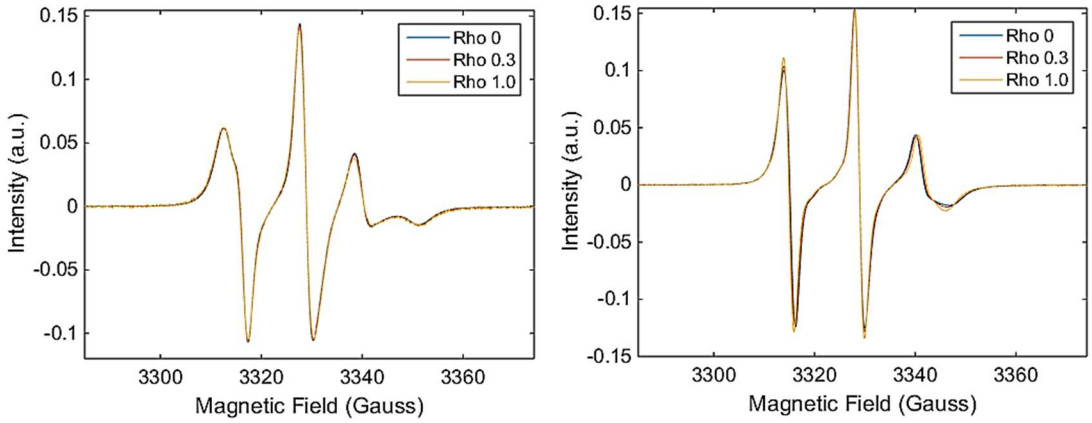

Figure 3-5: The pure phase L_o (left) and L_d (right) spectra for the Chol 22 line. The L_o and L_d spectra change minimally as we move along the phase boundary with the L_d phase showing more variance than the L_o phase.

This estimation was tested on a few different $L_d(\rho)$ and $L_o(\rho)$ spectra and the equation was verified. It is also observed that the pure phase spectra for the L_o and L_d phases does not change very much as we move along the phase boundary (Figure 3-5). Further, it can be seen that the L_d spectra changes more than the L_o spectra as we move along the phase boundary. The above spectra were fit using the nonlinear least squares program (NLSL) program developed by the Freed group.[96] The rotational diffusion and order parameters were obtained and are reported in Table 3-2.

Table 3-2: NLSL rotational and order parameters for the Chol 22 line (9 GHz spectra) using the MOMD model [137,140]

rho (ρ)	Phase	$R_\perp$ ($log_{10}\ sec^{-1}$)	S_0
0.0	L_o	8.6	0.36
0.3	L_o	8.6	0.36
1.0	L_o	8.5	0.34
0.0	L_d	8.4	0.13
0.3	L_d	8.5	0.12
1.0	L_d	8.5	0.11

As expected the rotational diffusion tensors values are similar for the two phases (L_o and L_d) varying between 0.2 - 0.4 x 10^9 s^{-1}. The order parameter however does change between the two phases, with the L_o phase showing significant order (0.34-0.36) when compared to the L_d phase (0.11-0.13). It is to be noted that 9 GHz cw-ESR spectra are not very sensitive to the rotational motions about the membrane normal ($R_\parallel$).

3.3.1. Fraction of L_o and K_p

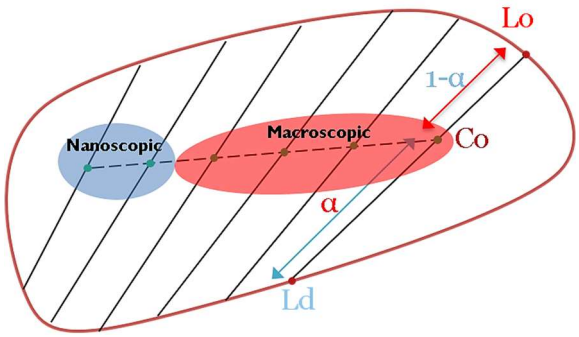

Figure 3-6: A simplified two-dimensional phase coexistence region to illustrate our compositional trajectory and the tie-lines in the coexistence region , where α represents the Lo fraction. Note: The modulated phase regime is also part of the macroscopic region in this figure.

The spectra of a point in the coexistence region on the Chol 22 line can be expressed as a linear combination of the ends (i.e., pure phase spectra) of the tie-line passing through this point (Figure 3-6). Hence, the fraction of the L_o and L_d phase was obtained by fitting the coexistence spectra with the pure phase (L_o and L_d) spectra and a variable parameter (α) representing the fraction of the L_o phase as shown in Equation 3-III. A few of the best fits are shown in Figure 3-7. As seen in the fits in Figure 3-7, only the two components of the L_o and the L_d phase are enough to fit the coexistence spectra for Chol 22 line. The fraction of the L_o phase (α) increases as the domain size decreases for the lower rho values. The L_o fraction value for rho 0 composition is 0.71, while the value for rho 1 composition is 0.28. Further, it is observed (Table 3-3) that the ratio of L_o fraction (α) observed and L_o fraction expected are different. This information can be used to obtain the partition coefficient values.

By our definition, the K_p values greater than 1 indicates that the spin label prefers the L_d phase, while a K_p value of lesser than 1 indicated a preference for the L_o phase. The results observed are similar to those observed earlier in the Freed group.[10,19] The K_p values along a tie-line are fixed but can vary between any two tie-lines and depends on the lipid composition (particularly cholesterol) of the L_o and L_d phases. It was observed that the K_p value does not change drastically, as the size-scale transition occurs implying that the phase behavior (the extent of ordering or fluidity) does not change at this transition. For the case of Chol 22 (at 9 GHz), only the five relevant values for the 95 GHz measurements are reported here. The values for the other rho values are not central to further discussion and are reported elsewhere.[137,140]

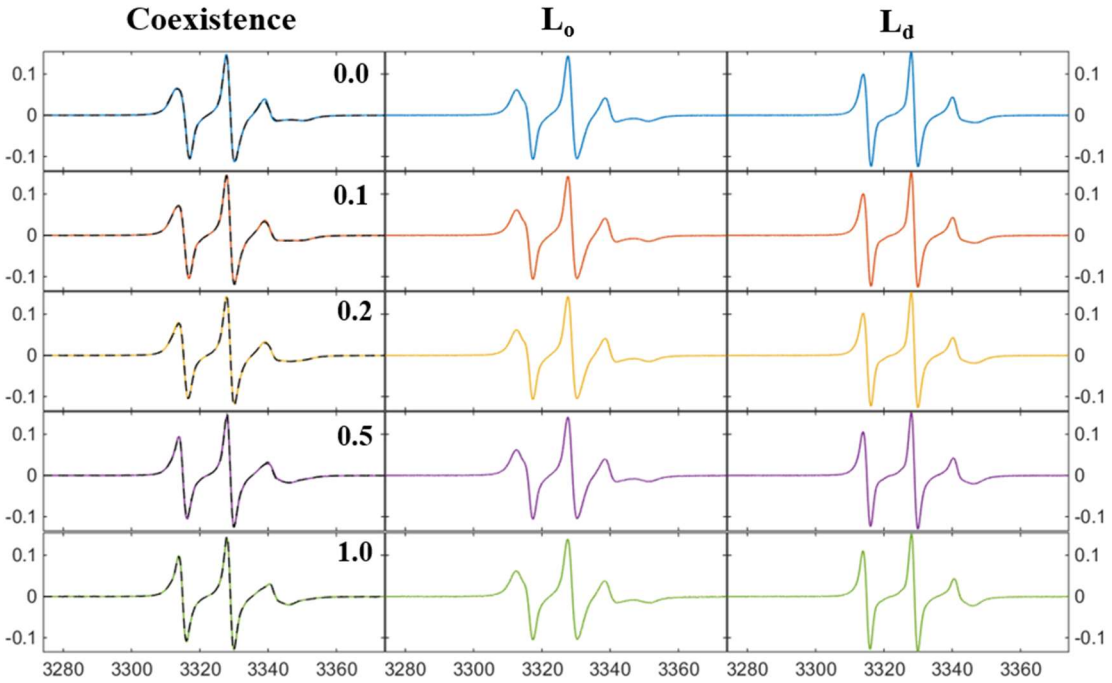

Figure 3-7: Summary of results for Chol 22 (9 GHz data). The intensity (in a.u.) is plotted against the magnetic field (G) in each plot. Left: Coexistence Spectra (experimental data are shown as solid lines and the fit spectra are shown as black dashed line). Center: Lo spectra and Right: Ld Spectra. The first three rho values (rho 0, 0.1, 0.2) are in the nanodomain region and the last two (rho 0.5, 1.0) are in the macroscopic region.

Table 3-3: Summary of the L_o fractions for the Chol 22 line at 9 GHz. Note the L_o fraction represents the fraction of 16-PC molecules present in the L_o phase.

rho value	L_o fraction Observed (α)	L_o fraction expected	K_p
0.0	0.71	0.64	0.89
0.1	0.58	0.62	1.08
0.2	0.48	0.60	1.24
0.5	0.31	0.57	1.82
1.0	0.28	0.53	1.88

3.4.Results and Discussion:

3.4.1. 95GHz cw-ESR for Chol 22 (MOMD vs SRLS)

The number of high field ESR studying the fluid phases (i.e., L_o and L_d phase in particular) of lipid membrane systems are limited.[15,47,103,142] Further, this is the first study that has attempted to comprehensively understand the phase behavior of coexisting nanodomains using 95 GHz ESR. As 95 GHz ESR spectroscopy has enhanced g-resolution (when compared to 9 GHz) due to higher magnetic fields, it is more sensitive to the faster rotational diffusion parameters. The MOMD model based NLSL fitting of the pure phase spectra at different rho values was initially carried out to obtain the rotational and order parameters (Table 3-4), which should be the same as at 9 GHz if the analyses are accurate. The 95 GHz spectra shows that the L_o domains have $R_\perp$ values of 0.7-1 x 10^9 s^{-1}. These values are almost comparable to the values obtained at the 9 GHz (~0.4 x 10^9 s^{-1}). For the L_d domains, the $R_\perp$ values observed for the 95 GHz (0.5-0.6 x $10^9 s^{-1}$) spectra are also similar to the 9 GHz (0.2-0.3 x 10^9 s^{-1}). In both the 9 and 95 GHz ESR spectra the L_o domains have faster $R_\perp$ values when compared to the L_d domains, which is in agreement with other studies performed earlier.[18,19] As expected the L_o domains are significantly more ordered (S_0 values of 0.35 - 0.37) than the L_d domains (0.20 - 0.23). Unlike 9 GHz ESR spectroscopy, the 95 GHz spectra are also sensitive to the $R_\parallel$ values (0.6-1.4 x 10^8 s^{-1}); this is one of the first studies where 95 GHz ESR spectra was used to determine the $R_\parallel$ values and shows the strength of this technique. In general, the $R_\parallel$ values reported were about 5-10 times slower than the $R_\perp$ values. The slower rates for $R_\parallel$ is consistent with results obtained from molecular

dynamics simulations of the lipid membranes,[143] where it has been observed that $R_{\parallel}/R_{\perp} \approx 0.1$. Similar trends have also been seen by cw-ESR for lipid phases before[15]. The differences in the $R_{\perp}$ and S_0 values between 9 and 95 GHz data are discussed in detailed below.

Table 3-4: NLSL rotational and order parameters for the Chol 22 line (95 GHz spectra) using the MOMD model.

	$R_{\perp}$ *log sec*$^{-1}$	$R_{\parallel}$ *log sec*$^{-1}$	S_0	S_2
$L_d(0.0)$	*8.75*	*7.88*	*0.21*	*-0.09*
$L_d(1.0)$	*8.73*	*8.14*	*0.23*	*-0.03*
$L_o(0.0)$	*8.87*	*7.75*	*0.36*	*-0.31*
$L_o(1.0)$	*8.96*	*7.82*	*0.36*	*-0.29*

Figure 3-8 shows the two main modes of motion that affects the ESR spectral shape: (a) the slow molecular diffusion (overall motion) of the lipid (in this case the entire lipid 16-PC molecule) and (b) the faster segmental motion (or the internal modes of the side chain where the nitroxide spin label is attached). At 95 GHz, the slow overall motion of the 16-PC molecule is expected to be almost frozen out and hence these spectra are more sensitive to the segmental diffusion at the site of the probe, while 9 GHz is also influenced by the overall motion. Further, the MOMD model based fits of the 9 GHz spectra give us a combination of the segmental diffusion and the molecular motion (i.e., overall motion). Hence, some of the parameters are smeared out, which leads to the differences in the $R_{\perp}$ values estimated from the 9 and 95 GHz data. To address this problem, the Freed group has developed the Slowly Relaxing Local Structure (or SRLS) model that can be used to fit both the global and local motion.[7,13–15] This model therefore

makes it possible to perform simultaneous global fitting of both the 9 and 95 GHz spectra with the same set of dynamical parameters. In MOMD, the global motions are assumed to be "frozen", therefore time-independent and randomly oriented. In SRLS, the global motions are allowed to be time-dependent by specifically introducing slow rotational diffusion for the larger structure.[6]

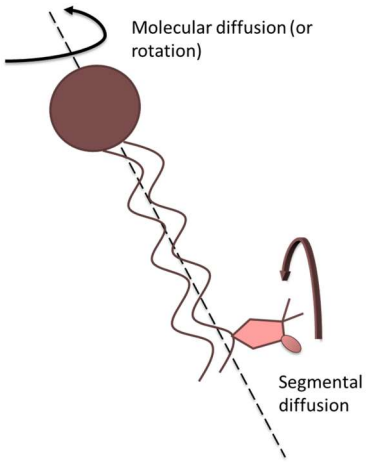

Figure 3-8: Global (molecular diffusion) vs Local (segmental diffusion) motion. At 95 GHz the global motion is completely frozen out while at 9 GHz, the global motion also affects the spectra.

The SRLS model was used in this work to simultaneously fit the 9 and 95 GHz cw-ESR spectra. During the simultaneous fitting process, both the 9 and 95 GHz spectra were appropriately weighted to give equal importance to the ESR spectra at both the frequencies[14]. The SRLS fitting procedure involves two steps:

(1) First, the best-fit dynamic parameters obtained from the 95 GHz MOMD model fits is used as seed values for the local dynamical parameters. The 95 GHz values are used because they are more sensitive to the local/segmental motions (as discussed

earlier). Only the global parameters were varied to obtain approximate global parameters.

(2) Finally, all the global and local parameters are varied together to obtain the best fits. The best SRLS fits obtained for the L_o and L_d phases are shown in Figure 3-9 and are summarized in Table 3-5 .

In general, it is noted that the local parameters obtained from the SRLS fits are not very different from the local parameters obtained from the MOMD fits of the 95 GHz ESR spectra. The global rotational rates obtained from the fits are denoted by a superscript c (e.g. R_⊥^c). The R_⊥^c values were around 0.3-0.4 x 107 s-1 and the R_‖^c was around 0.2 x 107 s-1 for both the Lo and Ld phases. The SRLS fits also yield the global ordering parameters i.e., the alignment of the lipid molecule with the bilayer normal. In general, the spectra of 16-PC spin label are not "directly" sensitive to the global ordering potential with only a small global ordering potential (a_20 ~ -0.15 for the Lo phase and a_20= 0.0 for the Ld phase) required to obtain good fits. The case of high local ordering and low global ordering for the 16-PC probe in the Lo and Ld phase implies that for an end labeled spin probe (like 16-PC), the spin probe attached to the end of the acyl chain segment acts relatively independently from the global ordering. However, it is sensitive to the interstitial sites or defects in the lipid bilayer. These defects are more structured in the case of the Lo phase leading to a larger local ordering parameter (So). Hence, the local ordering parameter also "indirectly" gives us information about the global ordering in the system.

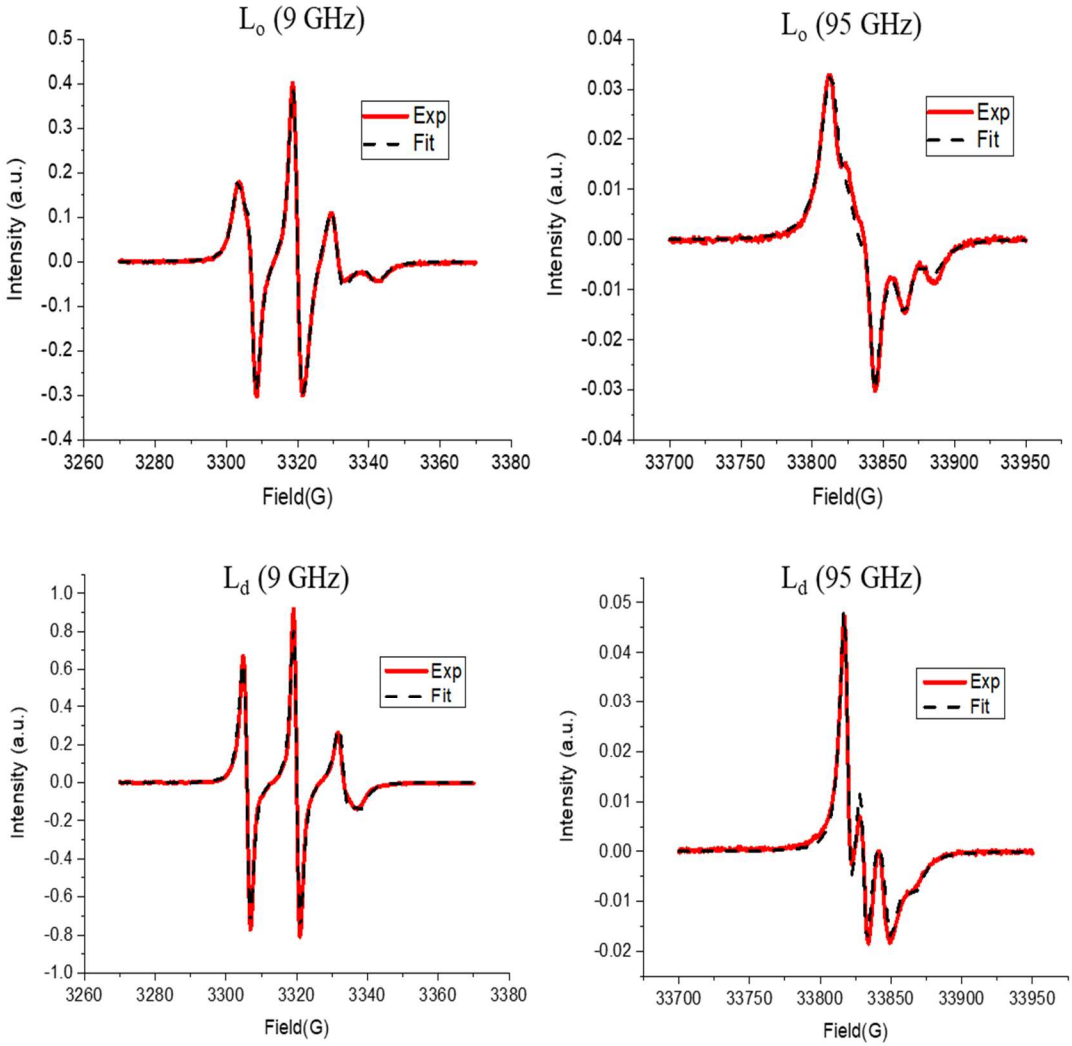

Figure 3-9: The SRLS fits for the pure phase spectra (L_o and L_d phase) for rho 1.0. The 9 and 95 GHz ESR spectra were fit simultaneously with the same set of dynamical and spin parameters.

Table 3-5: The motional and order parameters of the pure phase spectra (L_o and L_d) that are obtained from SRLS simulations of the 9 and 95 GHz data.

	Local Parameters				***Global Parameters***		
	$R_\perp$ $log\ sec^{-1}$	$R_\parallel$ $log\ sec^{-1}$	S_0	S_2	$R_\perp^c$ $log_{10}\ sec^{-1}$	$R_\parallel^c$ $log_{10}\ sec^{-1}$	a_{20}
L_d(0.0)	*8.79*	*8.35*	*0.21*	*-0.19*	*6.48*	*6.32*	*0.00*
L_d(1.0)	*8.69*	*8.38*	*0.17*	*-0.18*	*6.48*	*6.32*	*0.00*
L_o(0.0)	*8.73*	*7.90*	*0.37*	*-0.30*	*6.56*	*6.32*	*-0.13*
L_o(1.0)	*8.72*	*8.07*	*0.37*	*-0.29*	*6.57*	*6.32*	*-0.15*

3.4.1.1. Coexistence spectra and the tie-line analysis

Tie-line analysis was carried out for the 95 GHz data similar to the 9 GHz data to extract the L_o fraction (α) values. The results of this analysis are shown in Figure 3-10 and are summarized in the Table 3-6.

Table 3-6: The L_o fractions observed for the Chol 22 line at 95 GHz. Note the Lo fraction represents the fraction of 16-PC molecules present in the Lo phase.

rho	L_o fraction Observed (α) 9 GHz	L_o fraction Observed (α) 95 GHz	Δα (9 GHz-95 GHz)	L_o fraction expected
0.0	0.71	0.60	0.11	0.64
0.1	0.58	0.47	0.11	0.62
0.2	0.48	0.42	0.06	0.60
0.5	0.31	0.29	0.02	0.57
1.0	0.28	0.26	0.02	0.53

As can be seen, the fraction (α) of the L_o phase decreases as we move from rho 0.0 to rho 1.0, this trend was also observed using 9 GHz ESR earlier. Further, the α values in the macrodomain (rho 0.5 and 1.0 region) between the 9 and 95 GHz spectroscopy measurements are in close agreement with each other (i.e., a 2% difference in the value). However, in the nanodomain region, the α values do not agree. For example, in the case of rho 0.0, the L_o fraction value (α) at 9 GHz are close to 0.71 while the L_o fraction values at 95 GHz are close to 0.60 (i.e., a discrepancy of nearly 11%). The discrepancies in the L_o fraction values observed by 9 and 95 GHz spectra indicates that the K_p values estimated using 9 GHz spectroscopy (c.f. Table 3-3) are only accurate in the macrodomain region. Further, the change in the K_p value between rho 0.0 to 0.5 (0.89 to 1.82) is much greater than the change in K_p between rho 0.5 and 1.0 (1.82 to 1.88). This K_p behavior is unexpected as $K_p = e^{-\Delta G/RT}$, where ΔG is free energy difference

between the 16-PC probes in the L_o and L_d phases. As the L_o and L_d phase behavior does not change much as we move across the "rho" region, we expect a slightly exponential (nearly linear) change to the K_p value across the entire rho region. As the change in the K_p values in the nanodomain is large, this suggests that the 9 GHz fits in the nanodomain region are overestimating the amount of L_o phase present in the sample. The reasons for the discrepancy in L_o fraction and the K_p values are not completely understood but one possibility would be due to the presence of a significant "boundary" phase region (L_3). This is explored further below (Section 3.4.3).

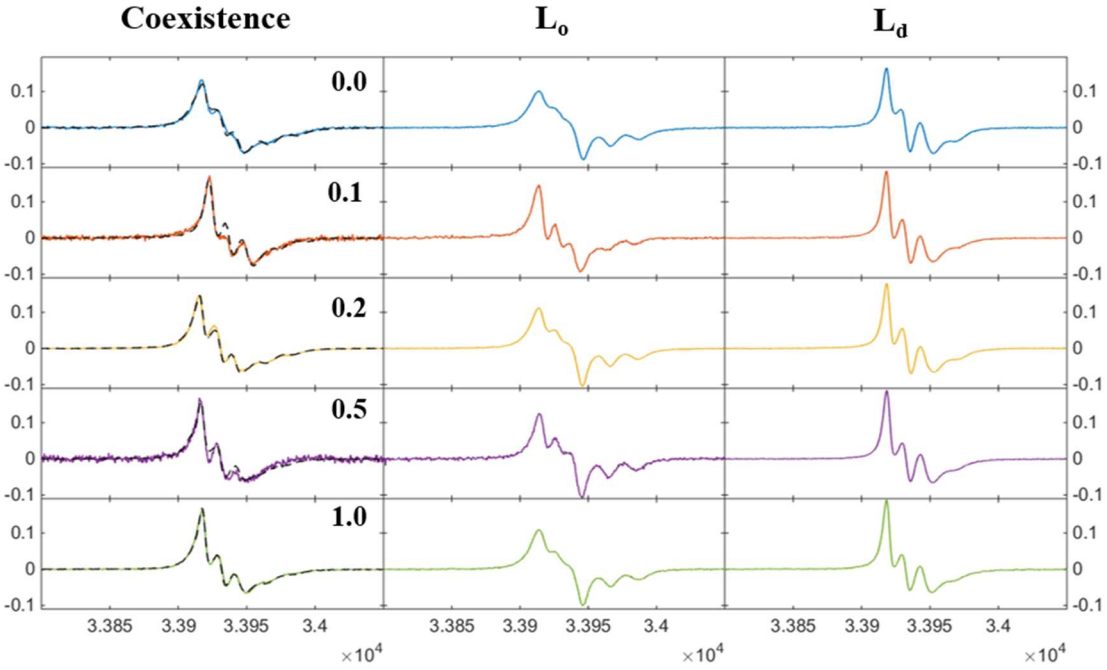

Figure 3-10: Summary of results for Chol 22 (95 GHz data). The intensity (in a.u.) is plotted against the magnetic field (G) in each plot. Left: Coexistence Spectra (experimental data are shown as solid lines and the fit spectra are shown as black dashed lines). Center: Lo spectra and Right: Ld Spectra.

The possibility that these differences in α values are due to sample preparation or other factors were eliminated by repeating the 9 GHz measurements, before performing the

95 GHz measurements. Further, Zhang et al.[14] have shown that the two different sample holders used for 9 and 95 GHz ESR measurements do not affect the spectral line shapes.

3.4.2. 9 GHz cw-ESR for Chol 26

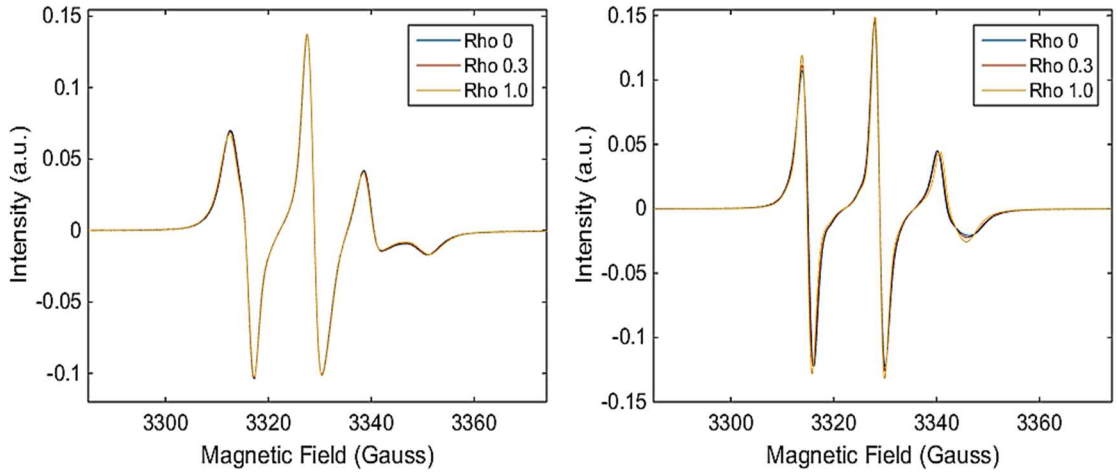

Figure 3-11: The pure phase L_o (left) and L_d (right) spectra for the Chol 26 line at three different rho values. Similar to the Chol 22 trajectory, the pure phase spectra does not change much with the rho values.

To supplement the results of Chol 22 coexistence line, another coexistence line containing 26% of cholesterol was studied (referred to as the Chol 26 line). The Chol 26 line forms nanodomains at higher rho (ρ) values than the Chol 22 line i.e., it forms nanodomains at higher DOPC concentrations. For the Chol 26 line, 84 points corresponding to different rho (ρ) values were measured. The pure phase (L_o and L_d) spectra for each of these points were obtained similar to the Chol 22 line. These spectra were analyzed and observed that the order and diffusion parameters are similar to the Chol 22 values. The fitting routine to determine the L_o fraction (α) was also performed (analogous to the Chol 22 line) and a sample of the results is shown in Figure 3-12 .

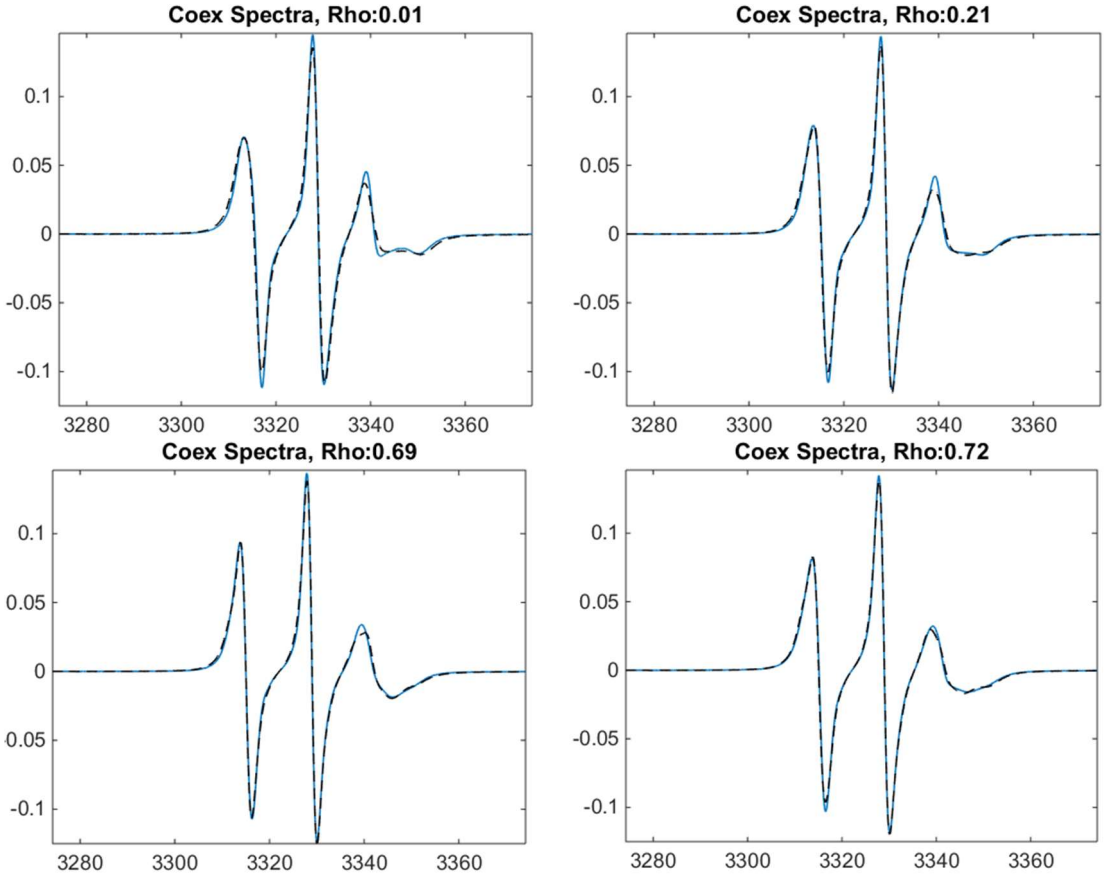

Figure 3-12: The coexistence spectra for four different rho values (0.01, 0.21, 0.69, and 0.72). The solid line represent the experimental spectra while the dashed line represents the fit spectra. It is clearly seen that for the lower rho values (i.e., in the nanoscopic region) the two component fits are not very accurate.

The results of all the fits are summarized in the Figure 3-13. As seen from the left plot the fraction of the 16-PC probe exhibiting L_o phase behavior, varies between 40-85%. This is compared with the expected values to obtain the Kp values which are ~1 (i.e., exhibiting almost equal partitioning as expected). The partition coefficient (K_p) values are dependent on the lipid composition, especially the level of cholesterol present in the sample. Models for the membrane organization indicate that cholesterol molecules occupy the interstitial sites between the hi-T_m lipids present in the ordered phase, hence

provides a steric hindrance for the nitroxide moiety of 16-PC spin probe. This effect is more pronounced for the other PC probes (i.e. 5 and 7-PC) as the cholesterol molecule prefers to be closer to the head group region of the lipid bilayer.[144] It is to be noted that previously reported K_p values have reportedly high error values,[40] almost 30% error in some cases. For the Chol 22 line, the range of K_p values observed with the 9 GHz cw-ESRis ~0.7-2.0. The K_p values for Chol 26 are also in a similar range, ~0.9-1.6. The values are similar to other values reported by the Freed group earlier.[19,40,52]

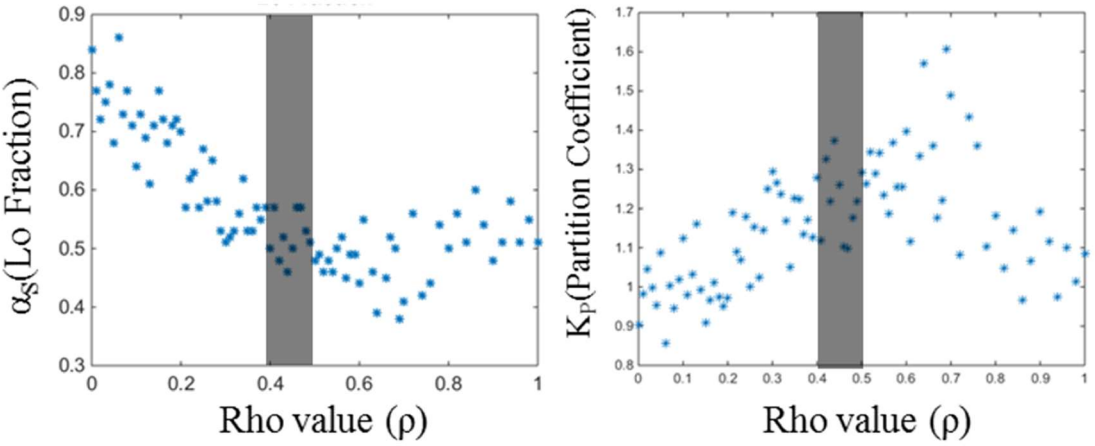

Figure 3-13:The L_o fraction and K_p for Chol 26. Left: Lo fraction (α) plotted versus the relative fraction of DOPC/POPC (i.e., rho value) for the Chol 26 trajectory; Right: A plot of the partition coefficient (K_p) and its dependence on the rho value. The K_p values are ~1, indicating that the 16-PC probe partitions nearly equally between the L_o and L_d phases. The grey band represents the modulated phase regime, for values below rho 0.4 we observe nanodomains.

$$\boldsymbol{Residual} = \left\| \boldsymbol{S_{Co(experiment)}} - \boldsymbol{S_{Co(fit)}} \right\| \qquad \text{3-VI}$$

In Figure 3-14, the residual magnitude (calculated as shown in Equation 3-VI) of a tie-line fit are shown, this gives us information about the features of coexistence spectra that are not fit by the two-component pure phase spectral fit. In an ideal case, the residual

values should represent noise present in the coexistence spectra and the pure phase spectra and is expected to be random (i.e. no correlation to the rho values). However, for the case of Chol 26 coexistence line, the residual values are bigger in the nanoscopic region than in the macroscopic region. The residual level present in the macrodomains region is essentially the noise present in the spectra and fits. Why does the residual magnitude depend on the size of domains? This facet of the residual magnitude is not well understood and is discussed in the boundary lipid section next.

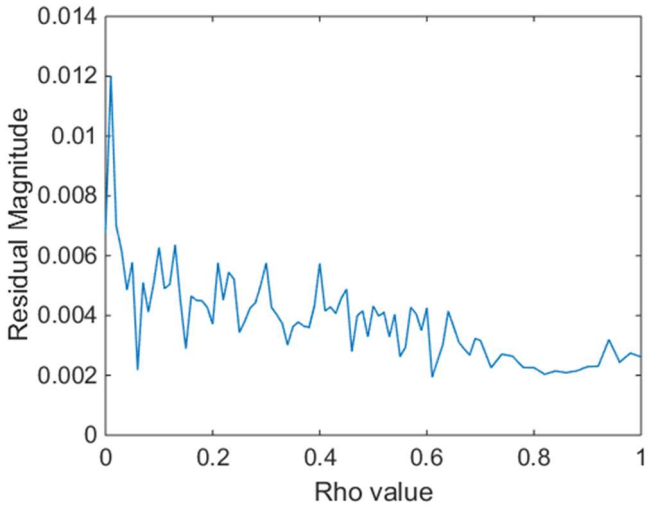

Figure 3-14: The residual magnitude obtained from a two component fit of the coexistence spectra (Chol 26). The residual magnitude is higher in the nanodomains (i.e., lower rho) than the macrodomains (rho >0.4)

3.4.3.Boundary lipids and phase behavior (L_3 phase)

The formation of nanoscopic domains from macroscopic domains should lead to a substantial increase in the interfacial regions between the ordered and disordered phase regions. Simple models indicate the fraction of this interfacial region would be inversely proportional to the domain size. A two orders of magnitude reduction in domain size

(i.e. from 1 µm to 10nm) would cause the interfacial region to increase by almost two orders of magnitude.The interfacial region is very important as many experiments have shown that there is a height mismatch between the L_o and L_d phases. Heberle[138] et al have shown that difference in heights (i.e., the distance between the head groups of the two leaflets of a bilayer) between the two domains is about 0.64 nm for domains with a radius of ~7nm (c.f. Figure 3-15). If there is a kink when the L_o and L_d domains come in contact with each other, then the acyl chain of the lipids in the L_o phase are exposed to the aqueous phase. This can cause significant hydrophobic interactions and potentially destabilize the membrane. To reduce hydrophobic exposure of the lipid acyl chain, it can be expected that lipids in the transition region between the domains adjust to reduce these hydrophobic interactions.[145]

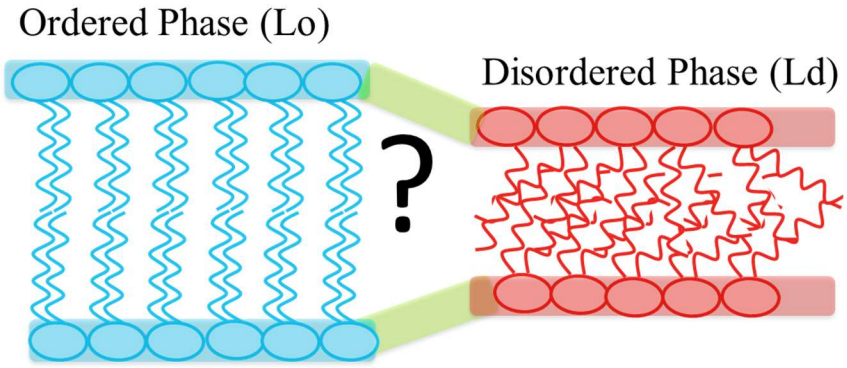

Figure 3-15: Membrane bilayer showing the height mismatch between the L_o and L_d phases. This mismatch is around 0.64 nm when the domain sizes are ~7nm.[138]

To estimate the percentage of the interfacial (boundary) region of the total lipids in the sample and its relation to domain size, a simple model based on fitting multiple small circular domains in a larger macroscopic sample is chosen. In this model, we can control the size of the domain, the size of annular ring around the domain and the separation

between any two domains. Using this model, it was estimated that for nanoscopic domains (radius of ~ 7 nm) the percentage of boundary region was at least ~11%. However, the boundary percentage expected for the circular domains gives us the lower limit for the boundary fraction. In reality these lipid domains are not circular and have more complex morphology as shown by Usery et al.[140], where the extent of boundary fraction is expected to be much larger. Therefore, the boundary fraction is likely to be a significant portion of the ESR signal and hence equation 3-III should be modified to include the effects of the boundary region.

$$\overrightarrow{S_{Co}}(\rho) = \alpha(\rho) \times \overrightarrow{S_{Lo}}(\rho) + \beta(\rho) \times \overrightarrow{S_{Ld}}(\rho) + \gamma(\rho) \times \overrightarrow{S_{L_3}}(\rho) \qquad \text{3-VII}$$

$$\text{Where } \alpha(\rho) + \beta(\rho) + \gamma(\rho) = 1$$

In the limit that $\gamma \rightarrow 0$, as is expected in the case with macrodomains, this equation will simplify to what we have in equation 3-III. The questions then arise, whether it is possible to distinguish such a boundary lipid ESR spectrum and does the boundary region (L_3) have a distinct ESR signal or is it a composite of the L_o/L_d phase signal (c.f. equation 3-VIII)? If the boundary region does not have a distinct ESR spectral signature, then it can likely be expressed as a linear combination of the pure phase spectra, i.e.

$$\overrightarrow{S_{L_3}}(\rho) \sim x_o \times \overrightarrow{S_{Lo}}(\rho) + x_d \times \overrightarrow{S_{Ld}}(\rho) \qquad \text{3-VIII}$$

Hence, equation 3-VII can be modified in this case to

$$S_{Co}(\rho) \sim \alpha'(\rho) \times \overrightarrow{S_{Lo}}(\rho) + \beta'(\rho) \times \overrightarrow{S_{Ld}}(\rho) \qquad \text{3-IX}$$

$$\text{Where } \alpha'(\rho) = \alpha(\rho) + x_o * \gamma(\rho) \text{ and } \beta'(\rho) = \beta(\rho) + x_d * \gamma(\rho)$$

Or

$$S(\rho) = \alpha'(\rho) \times \overrightarrow{S_{Lo}}(\rho) + \beta'(\rho) \times \overrightarrow{S_{Ld}}(\rho) + Residual \qquad \text{3-X}$$

Both α and β are ESR frequency independent in Equation 3-VII i.e., these values will be invariant between 9 and 95 GHz ESR experiments but are dependent on the lipid compositions (ρ values). However the modified α' (or fraction of L_o observed) and β' in Equation 3-IX can be ESR frequency-dependent. In general, ESR spectra obtained at different frequencies have increased sensitivity to different levels of ordering changes. Our simulations indicate that varying the ordering affects the different frequencies differently, so they can represent somewhat different views of the ordering in the system. Further, we observe that a small increase in order from the L_d (S_0 ~0.18-0.21) phase to S_0 ~ 0.26 causes the spectra at 9 GHz to appear more "L_o-like" while the 95 GHz line shapes are still "L_d-like". Therefore, the presence of a third component with intermediate order can cause the overestimation of the L_o-phase at 9 GHz and the L_d phase at 95 GHz. This can be used to explain the differences in the L_o fraction (c.f. Table 3-6) values observed between the 9 and 95 GHz spectroscopy. The discrepancies for rho 0.0 values between the 9 and 95 GHz values is 11% which is well within the range of the boundary region expected for this lipid composition. Further, it is noted that the discrepancies are larger for smaller domains (where the boundary component is expected to be larger). For the case of rho 0.0 (~7 nm) the discrepancy is ~11%, while for rho 0.2 (~12.4 nm) the discrepancy is only 6%. The fact that the L_o fraction values are bigger for the 9 GHz ESR spectroscopy indicates that the spectra of the boundary region (L_3) is more L_o-like at 9 GHz and more L_d-like at 95 GHz.

In Equation 3-X, the coexistence spectra can be approximated as a linear combination of the pure L_o and L_d phases along with a residual. This residual is part of the spectra

that is not fit by the two-component fit, in an ideal if the boundary component is zero, this residual will completely represent random noise that is present in the sample. However, in equation *3-VIII*, the L_3 phase is only approximated to be a combination of the pure L_o and L_d spectra, it is possible that some features of the boundary region are not captured by the L_o and L_d phase. Then these features will be present in the residual, which will be dependent on the size of the domains. As the boundary region is inversely proportional to the size of the domains, we expect more boundary region for the lower rho values (smaller domain sizes) and hence the residuals are likely to be greater. We observe this in the case of the Chol 26 line (c.f. Figure 3-14).

3.4.4.Boundary spectrum (L_3) and spectral estimation

The boundary spectrum can be determined by rearranging Equation 3-VII in terms of the boundary spectrum. Now the problem simplifies to estimating the correct fraction of the L_o (represented by α) and L_d(represented by β) phases

$$\overrightarrow{S_{L_3}}(\rho) = \frac{\overrightarrow{S_{Co}}(\rho) - \alpha(\rho) \times \overrightarrow{S_{Lo}}(\rho) - \beta(\rho) \times \overrightarrow{S_{Ld}}(\rho)}{1 - \alpha(\rho) - \beta(\rho)}$$

There are an infinite set of α and β values that can satisfy the above condition. However, in our case these α and β values can be constrained. Let us consider the rho 0 composition (for Chol 22) because this composition has the smallest domain sizes and expected to have the largest boundary fraction

- $0 < \alpha, \beta < 1$, both the α and β fraction values must be positive and lie between 0 and 1.

- $\alpha + \beta < 0.89$, as the discrepancy in the L_o fraction values is around 0.11 for the case of rho 0 (c.f. Table 3-6). In addition, $\alpha < 0.60$ (limit obtained from 95 GHz ESR spectroscopy) and $\beta < 0.29$ (limit obtained from 9 GHz ESR spectroscopy). This condition comes from the fact that the boundary spectra was approximated as a combination of the L_o and L_d phases when the two component fits are performed. This implies that the "real" L_o and L_d fraction values should be smaller than the L_o and L_d fraction values observed at 9 and 95 GHz ESR. In reality, this is a generous criteria, because if the "real" $\alpha = 0.6$ and $\beta = 0.29$, then we obtain a non-physical result of the boundary spectra being equivalent to the L_o spectra at 9 GHz and L_d spectra at 95 GHz.
- Physical appearance of the L_3 spectra, i.e., spectra with relatively large sharp features can be discarded as these line shapes are not typically observed for 16-PC in natural membranes. The advantages of simultaneously fitting spectra from the two frequencies (i.e., 9 and 95 GHz ESR) helps us in being more selective with the boundary spectra.

Using the above conditions, a candidate boundary spectrum was obtained with $\alpha = 0.48$ and $\beta = 0.14$. There are other boundary spectra possibilities with small differences to α ($\Delta\alpha = \pm 0.06$) and β ($\beta = \pm 0.04$) values but these spectra are nearly identical with very small differences to the boundary spectra observed. These differences are largest in the high field region for 9 GHz ESR spectroscopy (i.e., ~3340 G) and in the central peak region for the 95 GHz spectroscopy (i.e., 33840 G). However, all these differences are within the uncertainty levels in the experiment.

The boundary spectra (L_3) at 9 GHz (Figure 3-16) is more L_o-like as indicated by the broad peak in the low field region (~3300 G) and the double dip feature in the high field

region (~3340 G). However, the boundary spectra is more L_d-like at 95 GHz (Figure 3-16) as indicated by the peak at 33840 G. This difference in spectral line shape leads to different L_o fraction observed values between 9 and 95 GHz spectra in Table 3-6 when two component fits are performed.

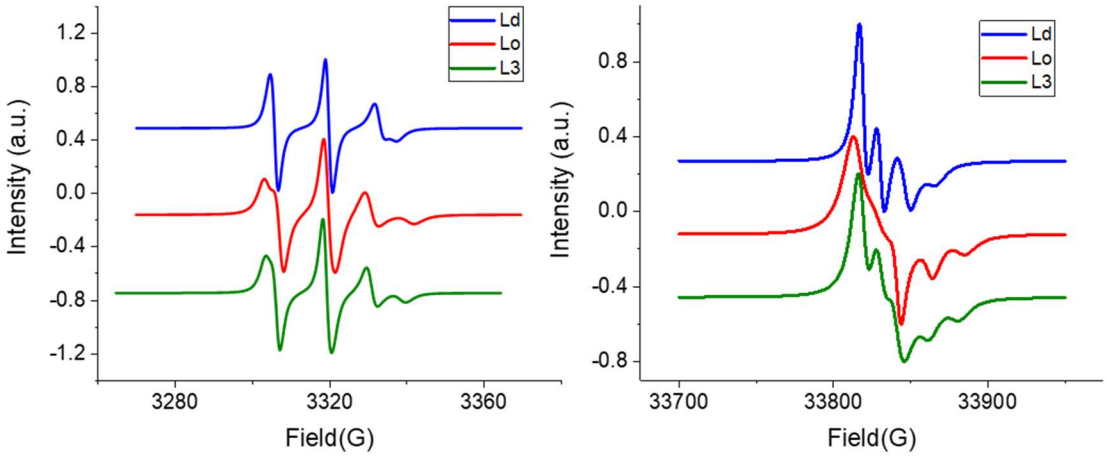

Figure 3-16: The ESR spectra of the L_o, L_d and boundary (L_3) phases at 9 GHz (left) and 95 GHz (right).

The SRLS fitting of both the 9 and 95 GHz ESR spectra was carried out to obtain the dynamical properties (Table 3-7). As expected, the SRLS simulations indicate that the boundary region spectrum (L_3) has intermediate local order (S_o = 0.31) between the L_o (0.35-0.37) and L_d (0.17-0.21) phases. The rotational rates are comparable to the L_o and L_d phases but are slightly faster for the L_3 phase. Particularly, the $R_{\|}$ rates are almost an order of magnitude faster for the L_3 phase than the L_o phase. However, there is a larger uncertainty in the determination of $R_{\|}$ rates as only the 95 GHz ESR spectra are sensitive to this motion. Finally, note that the global motional and dynamical parameters for the boundary region are similar to the parameters for the L_o and L_d phases.

Table 3-7: The motional and order parameters of boundary region spectra (L_3) that are obtained from SRLS simulations of the 9 and 95 GHz data.

	Local Parameters				Global Parameters		
	$R_\perp$ $\log_{10}$ sec^{-1}	$R_\parallel$ $\log_{10}$ sec^{-1}	S_0	S_2	$R_\perp^c$ $\log_{10}$ sec^{-1}	$R_\parallel^c$ $\log_{10}$ sec^{-1}	a_{20}
L_3	9.05	9.00	0.31	-0.28	6.60	6.32	-0.12

The boundary spectrum (L_3) should vary slightly with rho (ρ), however this can be ignored as the variation of L_3 spectra is likely to be minimal. This is a good approximation as we do not observe any significant changes to the L_o and L_d spectra in the nanodomain region between Rho 0.0 and Rho 0.2. The boundary spectra at 9 and 95 GHz ESR spectroscopy was used to determine the approximate boundary percentages at rho 0.1 and rho 0.2. A least squares fit of both 9 and 95 GHz ESR data was carried by varying both the $L_o(\alpha)$ and $L_d(\beta)$ fraction values to identify the boundary fraction ($\gamma = 1 - \alpha - \beta$). The best fit for rho 0.2 coexistence spectra using the L_o, L_d, and L_3 components is shown in Figure 3-17.

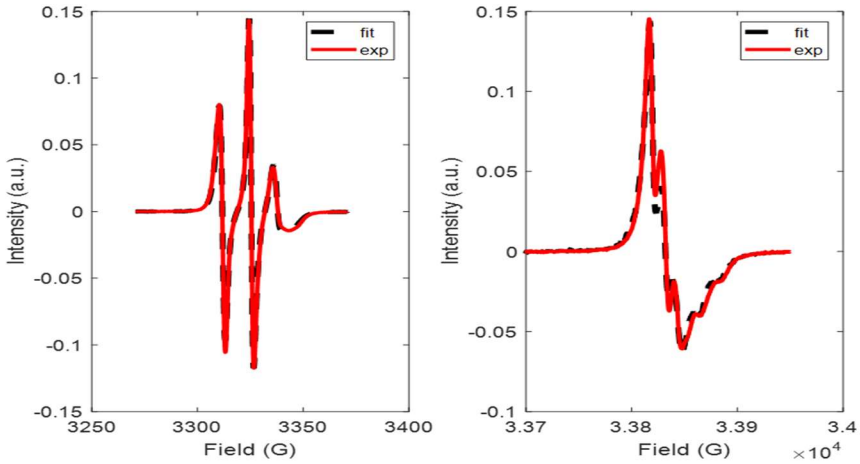

Figure 3-17: The coexistence cw-ESR (left: 9 GHz, right: 95 GHz) spectra for rho 0.2 along with the three component fits.

As the L_3 spectra can be expressed approximately as a linear combination of both the L_o and L_d spectra we get a small range of L_3 fraction (Table 3-8) values that give similar least squares minima value. In general, the boundary fraction values reduce as we move from rho 0.0 to rho 0.2. This behavior is expected because the domain sizes increase from rho 0.0 to rho 0.2 leading to a smaller boundary fraction. For the nanodomain region (rho 0.0 - rho, 0.2) we obtain the boundary fraction to be between 0.15-0.38, which shows that a significant fraction of ESR signal is obtained from the spin label (16-PC) present in the interface between L_o and L_d domains.

Table 3-8: The L_o, L_d and boundary (L_3) fractions observed for the Chol 22 line. Note α, β, and γ represents the fraction of 16-PC molecules present in the L_o, L_d and L_3 regions respectively.

	L_o fraction (α)	*L_d fraction (β)*	*Boundary fraction (γ)*
Rho 0.0	*0.48-0.54*	*0.14-0.18*	*0.38-0.28*
Rho 0.1	*0.40-0.44*	*0.34-0.37*	*0.26-0.19*
Rho 0.2	*0.33-0.37*	*0.47-0.48*	*0.20-0.15*

If the K_p of 16-PC in the different environments (L_o, L_d and L_3) is the same then the values in Table 3-8 represents the fraction of the lipid membrane exhibiting the corresponding phase behavior. At rho 0.0 (seven nm domain size), a boundary fraction of ~0.30 indicates that there are about 2-5 lipids in the interfacial region between the L_o and L_d regions depending on the shape of the domains. This implies that for a 7nm domain we have a transition region of approximately 2-4 nm. It is important to note that the 16-PC actually favors the L_d phase over the L_o phase (c.f. Table 3-3, K_p ~1.8 observed in the macrodomain region). As the boundary phase has intermediate order

between the L_o and L_d phases, it is a reasonable approximation that the boundary phase has intermediate partition coefficient (K_p ~1.2-1.3 with respect to the L_o phase) between the L_o and L_d phases. Therefore, it is likely that we have overestimated the amount of the L_d phase and underestimated the amount of the L_o phase and to a smaller extent the boundary phase (L_3) present in the sample. However, as the L_d fractions measured are quite small (0.14-0.47), there is at about a 10% error in our estimation of the boundary fraction.

3.5.Conclusions

A comprehensive analysis of the four-component lipid phase diagram containing DSPC/POPC/DOPC/Chol was carried out using ESR spectroscopy. POPC rich domains were nanoscopic in nature, while DOPC rich domains were macroscopic. By replacing POPC with DOPC the size-scale transitioning from nanoscopic domains to macroscopic domains were studied. It was observed that the size scale transition does not affect the phase behavior of the system i.e., lipids in the nanodomains and macroscopic domains show similar ordering and motional parameters. High Field High Frequency (HFHF) ESR (i.e., 95 GHz) was also used to study this system. This was one of the first high frequency studies that was used to obtain the motional and order parameters for phase separate coexisting domains (especially nanoscopic domains). The dynamic parameters were obtained using the Slowly Relaxing Local Structure (SRLS) model to simultaneously fit both the 9 and 95 GHz spectra. Further indirect evidence such as increased residual for smaller domains sizes and unphysical frequency dependent L_o fraction values were obtained to show the likely presence of a boundary region (L_3) in

the nanodomain region. Simultaneous 9 and 95 GHz cw-ESR fitting was performed to obtain a candidate boundary spectrum that has intermediate order between the L_o and L_d phases. However, further measurements with two-dimensional techniques such as 2D-ELDOR spectroscopy might help better resolve the boundary region components.

3.6.Supplementary Information:

3.6.1.95 GHz MOMD Simulations

The 95 GHz spectral simulations are more accurate to obtain the motional parameters from a MOMD based fit, as the overall tumbling motion of the lipids are completely averaged out and only the segmental motion is observed. However, there are some basic challenges that need to be overcome before the fitting can be performed and are listed below.

(a) Basis Pruning: As the 95 GHz ESR spectral line shapes are more complex than the 9 GHz case (c.f. Figure 3-4), a larger basis set is required to perform the spectral fitting. A choice of a larger basis set makes the spectral fitting computationally more expensive; hence, it becomes vital to perform basis pruning before running the MOMD simulation. It is observed that the basis pruning for these spectral line shapes typically reduces the number of basis sets required by a factor of 10-50.

(b) Number of Orientations: For the 9 GHz spectra, it is has been a practice to use ~25 orientations (NLSL parameter, $n_{ort} = 25$) for the MOMD calculations. This number was chosen empirically based on trial and error, and is sufficient for most low field ESR spectra (i.e., 9 GHz). However, as the 95 GHz spectra is more g-resolved and is highly orientation selective it becomes vital to increase the number of orientations for MOMD fits. For all the simulations reported here, the number of orientations was fixed to be about ~50. This number was chosen carefully after observing empirically how the fits varied with increase in orientations. Further, this information is also verified when the basis pruning is performed, for 9 GHz spectra is seen that the number of basis sets

required does not grow when more number of orientations are used. Whereas for the 95 GHz, it is seen that the number of basis sets are increased by 1 or 2 when the number of orientations increases in the range of 30-35 (Figure 3-18). Hence, a conservative value of 50 was chosen for the number of orientations. If lesser than 35 orientations are used than the MOMD program does not converge to the right values for the order and motional parameters.

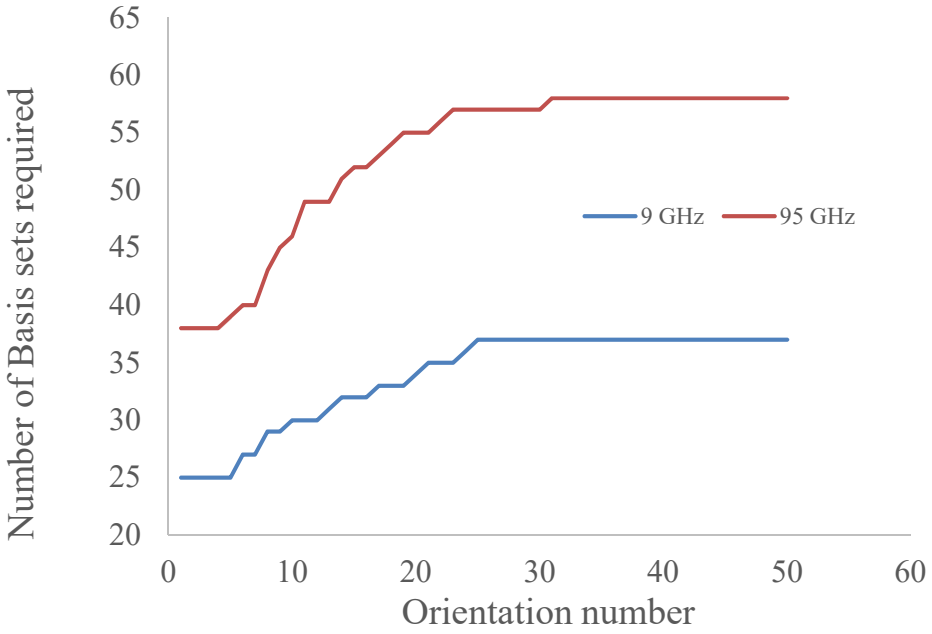

Figure 3-18: The number of basis functions for the cw-ESR simulations required depending on the number of orientations , as it is seen there is a small increase in the number of orientations required for the 95GHz spectra when 30+ orientations are used.

CHAPTER 4 : STUDYING IMMUNE RESPONSE DUE TO MULTIVALENT ANTIGEN BY ESR

4.1. Introduction

4.1.1. The model for IgE receptor binding

The dynamical and structural changes induced in the plasma membrane due to the crosslinking of immunoglobulin E (IgE) – receptor (FcεRI) complexes by multivalent antigen play a major role in initiating the signaling cascade that leads to an immune response from the cell.[34,146] Previous evidence suggests the formation of submicroscopic lipid ordered domains due to crosslinking of the IgE-FcεRI complexes at the plasma membrane. These domains selectively recruit signaling proteins that promote tyrosine phosphorylation of FcεRI and initiate the signaling cascades that lead to functional responses from the cell such as degranulation. It is medically important to study these complexes because they initiate the global cellular responses that can sometimes lead to life-threatening allergic reactions. Further, the study of IgE-FcεRI complexes can be used as a model to understand the signaling pathways in other structurally and functionally-related receptors such as the T cell and B cell receptors.[147]

The response to the crosslinking of IgE-receptor complexes is likely to involve the restructuring of the plasma membrane to form larger sub-microscopic liquid ordered (L_o)-like domains. These L_o domains are known to preferentially recruit Lyn kinase as indicated by the co-clustering of Lyn kinase with IgE-FcεRI in Scanning Electron Microscopy (SEM) and fluorescence studies.[148,149] Lyn kinase prefers to be in L_o

regions due to its membrane anchoring by saturated palmitoyl and myristoyl chains. In the L_o regions, Lyn is protected from transmembrane phosphatases that preferentially reside in the L_d regions.[150] Crosslinked clusters of IgE-FcεRI cause the formation of larger L_o regions in the plasma membrane where these receptors are phosphorylated by active Lyn kinase. This phosphorylation of IgE-FcεRI initiates other downstream signaling processes that mediate mast cell activation in the allergic response. Although many of these protein-protein interactions have been defined, the role of the plasma membrane in stabilizing these interactions is not yet completely understood. There are many reviews that highlight the daunting challenges for characterizing the structures and functions of membrane systems, especially for submicroscopic lipid domains.[151] Though the signaling mechanism (Figure 4-1) is known to involve plasma membrane restructuring, the extent of this restructuring and the kinetics of the submicroscopic domains formation remains inadequately understood. The term "lipid raft," commonly used to refer to these elusive structural arrangements, remains ill-defined and the subject of great controversy. Furthermore, the kinetics of IgE-FcεRI aggregation and the formation of these domains in live cell membranes must be characterized in better detail. Moreover, the role of cholesterol in cell membrane phase behavior and signaling is not completely understood.

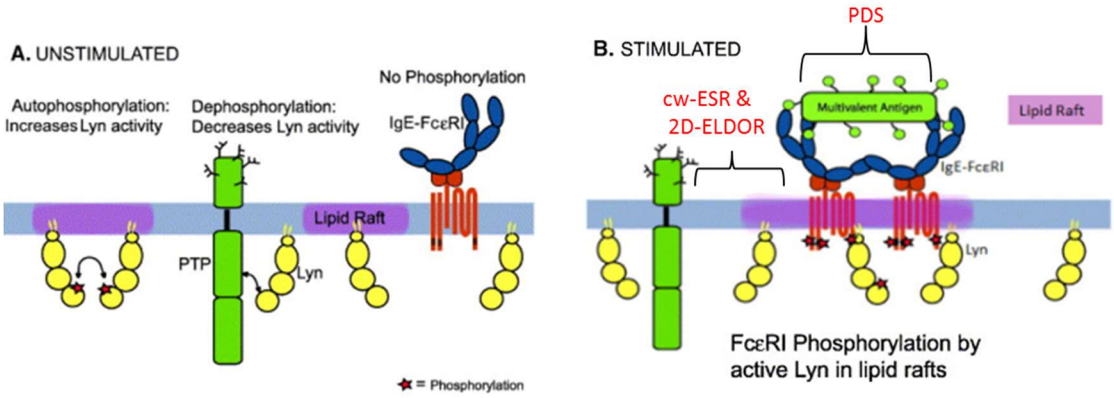

Figure 4-1: Clustering of the IgE (blue)-FcεRI(red) receptor assembly in the (a) unstimulated and (b) stimulated membrane. Cw-ESR and 2D-ELDOR can be used to study the membrane phase behavior while PDS along with rapid freeze quench method can be used study the kinetics of aggregation.

Earlier, cw-ESR (at 9 GHz) was used to show the co-existence of liquid ordered (L_o, "raft-like") & disordered (L_d) domains in mammalian cells and their derivatives (detergent-resistant membranes and plasma membrane vesicles).[18,19,133] Furthermore, because experiments in live cells are made difficult by the limited lifetime of spin probes (i.e., spin probes, being radicals, are reduced by enzymes present in the plasma membrane[19]), the membrane restructuring in plasma membrane vesicles (PMVs) obtained by chemically-induced vesiculation ("blebbing") of live cells was studied. The greater sample stability of these PMVs allowed for the use of more sophisticated advanced ESR techniques that required more extended signal acquisition times. So, 2D-ELDOR (Electron-Electron Double Resonance[6,92]) was used to detect changes due to antigen–receptor crosslinking by multivalent antigen ($DNP_{16}BSA$) in PMVs obtained from RBL mast cells. This showed the coexistence of L_o and L_d phases (optically unresolvable, and therefore submicroscopic, domains) with a moderate increase in the disordered phase (L_d) after receptor crosslinking.[20]

4.1.2. Dynamics of IgE Crosslinking

The crosslinking of IgE-FcεRI complexes can be studied with conventional fluorescence microscopy but requires sub diffraction-limited spatial techniques (such as PALM and STORM[152]) to obtain any quantitative measurements for the formation of the receptor clusters. Receptors are randomly organized around the cell membrane in unstimulated membranes and become clustered/ordered when they interact with the multivalent antigen. Studies have indicated the average domain correlation length (ξ) changes from around ~200 nm in unstimulated cells to ~70 nm within three mins of antigen addition.[153] Many other studies have attempted to study this aspect of IgE crosslinking in membranes through fluorescence quenching or similar techniques. However, very little information is available on the change in the inter IgE-IgE distance distribution with time after a crosslinking event. Pulsed Dipolar Spectroscopy (PDS) techniques such as DEER and DQC are able to measure distances in the 10-100Å range[62] which would be ideal for studying the IgE-IgE distance in crosslinked aggregates. Furthermore, the coupling of PDS with rapid freeze quench techniques[154] gives us the ability to study the time dependent kinetics of the IgE aggregation, by observing the PDS signal at specific time intervals before and after crosslinking with antigen. This would allow for direct measurement of receptor aggregation kinetics by measuring the time-dependent nanoscale changes in the size of receptor clusters.

To understand the dynamics of IgE crosslinking, it is essential to obtain only the intermolecular signal between two neighboring IgE's and not the intramolecular signal between two spin labels present on the same IgE. Spin labeling of the IgE antibody with

maleimido-TEMPO attached spin labels on all the available lysines on the protein. This method attached about five spin labels per IgE molecule so it was difficult to obtain the intermolecular signal caused by IgE aggregation by a multivalent antigen (like BSA-DNP_{16}).

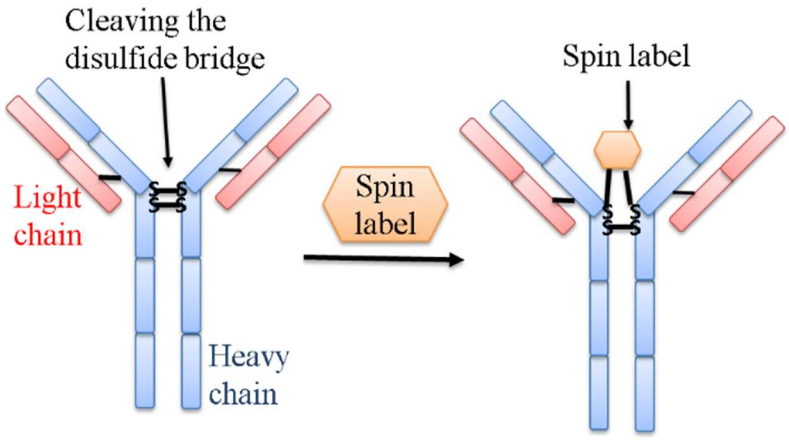

Figure 4-2: Spin-labeling of IgE at the inter-heavy chain position by cleaving the disulfide bridge and attaching a bidentate spin label (bis-MTS-P)

Hence, a novel method (Figure 4-2) was developed that allowed us to selectively attach one spin label per IgE molecule. In this method, a disulfide bridge between the inter-heavy chains of IgE is broken selectively by a reducing agent to make available two free cysteines in neighboring heavy chains of IgE. To the IgE antibody the bidentate ligand (bis-MTS-P, see Figure 4-4) is then attached, thus binding to both the available cysteines on neighboring heavy chains. The attachment of the bidentate ligand involves the formation of two disulfide bonds. Therefore, it is possible that the two cysteines could be bound to two different bis-MTS-P radicals, but this is unlikely because (a) steric hindrance prevents access to this site by two different bis-MTS-P radicals, and (b) the formation of the first disulfide bond increases the local concentration of the bis-MTS-P

label, which makes it more likely to form the second disulfide bond. This bidentate spin label has other advantages as well, due to its rigid linking to two different cysteines: it has limited rotamer states, and provides for narrow distance distribution when used for PDS applications.[155]

4.1.3. Membrane Dynamics and Cholesterol depletion

Previous evidence shows that cholesterol depletion interferes with the earliest steps in IgE receptor signaling.[156] This cholesterol depletion not only affects the phase behavior but also interferes with the signaling pathways and raft distribution in the cell.[157–159] Methyl-β-cyclodextrin (MβCD), a water-soluble cyclic polysaccharide, was initially used for the delivery of non-polar drugs in polar media. However, MβCD also induced cholesterol depletion at the membrane binding region, because the non-polar cavity of MβCD has a very strong affinity for cholesterol. Therefore, MβCD was used extensively to study cholesterol depletion in the plasma membrane.[160] In live cells, ~20% decrease in the total cholesterol is expected after five min. of MβCD addition while there is ~50% reduction in cholesterol after 15 min. of MβCD addition.[153] Fluorescence imaging measurements made by the Baird-Holowka group indicates that these membranes undergo phase separation into raft-like phases when undergoing cholesterol depletion by MβCD. However, the exact nature of these raft-like phases is not well understood; some recent studies[161,162] indicate that the raft-like phases could be solid or gel-like and not liquid ordered (L_o). Other studies have indicated that a decrease in cholesterol concentration leads to an increase in the L_d phase.[163] This can be expected as well,

because cholesterol is required for the formation of the L_o phase.[29] We can understand this by comparing with the model membrane system of DSPC/DOPC/Chol (Figure 4-3; Lα=L_d, Lβ=gel). The depletion of cholesterol leads to three different possibilities for the phase behavior of the system: (a) L_d +L_o; (b) L_d+ L_o+ gel; and (c) L_d + gel.

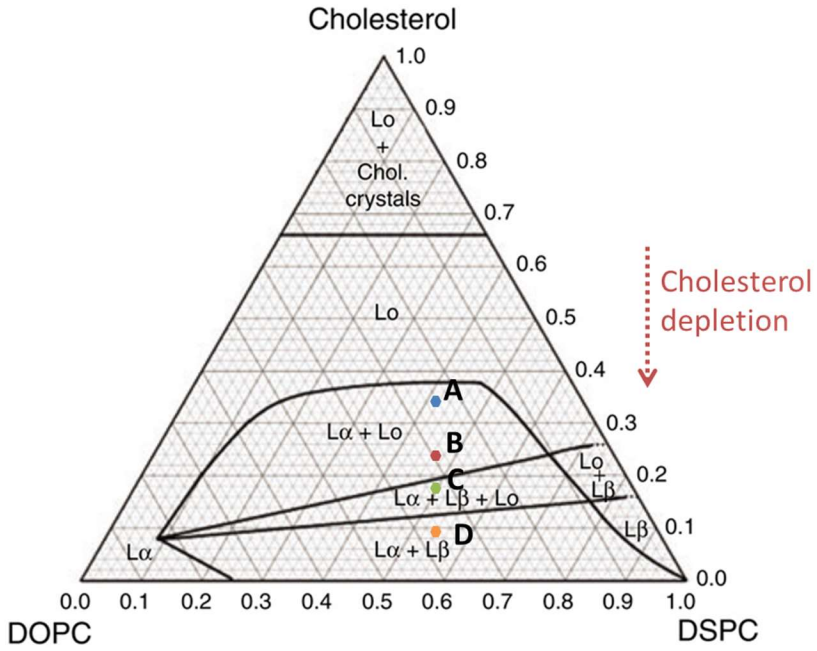

Figure 4-3: DSPC/DOPC/Chol phase diagram showing the different phase coexistence regions. As natural membranes are usually in the L_o and L_d phase coexistence regime. Point (A) represents the phase behavior of a natural membrane. Points (B), (C) and (D) represent the potential end points of cholesterol depletion. As can be seen, depending on the extent of local cholesterol depletion, the remaining lipids can exhibit either (B) L_α (L_d)+L_o, (C) L_α +L_o+L_β, or (D) L_α+L_β. L_α refers to the liquid disordered phase and L_β refers to the gel phase. Figure was modified from Feigenson (2006)[164]

4.2. Experimental

4.2.1. Spin labeling of IgE with bidentate cysteine nitroxide

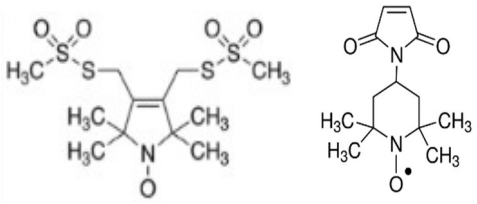

Figure 4-4: Structure of the bidentate spin label (bis-MTS-P) or 3,4-Bis-(methanethiosulfonylmethyl)-2,2,5,5-tetramethyl-2,5-dihydro-1H-pyrrol-1-yloxy radical (left). Structure of 4-Maleimido-TEMPO or 4-Maleimido-2,2,6,6-tetramethyl-1-piperidinylox free radical (right).

Spin-labeling was performed using a bidentate ligand similar to that used by the Hubbell group.[155] 300µl of 1mg/ml of IgE was dialyzed with BBS buffer at pH 8.0 for at least six hrs. The IgE in BBS is reduced with a fresh solution of 1mM dithiothreitol (DTT) for one hour. This step cleaves one or more disulfide bonds of the disulfide bridge between the inter-heavy chains. The pH of the IgE solution is lowered to 7.0 with the addition of small amounts (7.8 µl) of 0.1M HCl, and 15µl of 52mM bis-MTS-P spin label to obtain about 2.5mM concentration of the spin label. This reaction was carried out for about one hour and then the reaction mixture was spun down twice at 11-12,000 rpm for 5-15 minutes. The reaction mixture was dialyzed with PBS buffer and then spun down thrice at 13,000 rpm for 10 minutes. UV-VIS spectra of the spin labeled sample were compared with the native sample and no discernable changes were observed, which indicates that the spin labeling did not denature the sample. Based on the ESR

signal (Figure 4-5), the spin label concentration was identified to be 0.50 ± 0.06 μM, which shows that the spin labeling efficiency is around 10% for this method.

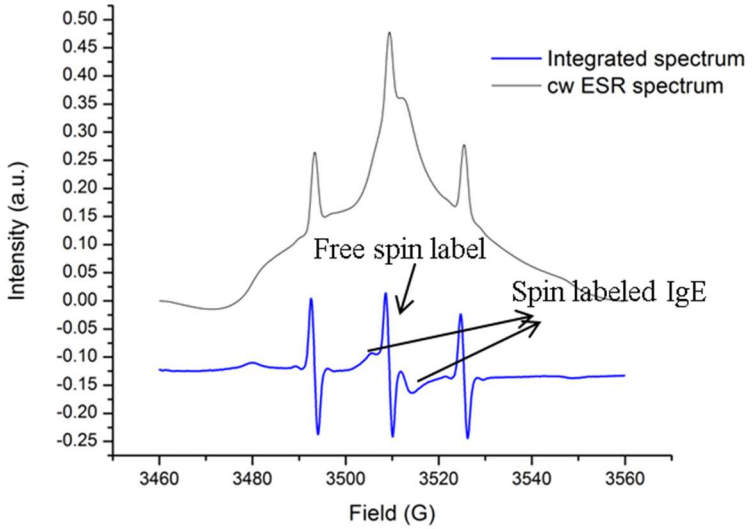

Figure 4-5: cw-spectra of IgE spin-labeled in the inter-heavy chain position with bis-MTS-P spin label. The broad ESR spectral signature corresponds to the spin-labeled IgE while the narrow/sharp lines correspond to the unreacted spin label.

The spin-labeled IgE sample was mixed in with twice the number of moles of trivalent antigen (Y_{16}-DNP_3, c.f. Figure 4-8). This crosslinking was allowed to reach equilibrium in 10-15 min. and then rapidly frozen in liq. N_2 to 77 K. The sample was then transferred to our home built Ku band spectrometer to observe the four-pulse DEER spectrum at 20-30K for ~18 h.

4.2.2. Preparation of Plasma Membrane Vesicles (PMV's) for cw-ESR

Monolayers of RBL-2H3 cells in small tissue culture flasks (T75 flask containing ~5 x 10^7 cells) were washed with 4ml of BB buffer (2 mM $CaCl_2$, 10 mM Hepes, 150 mM

NaCl, pH 7.4), and incubated with 6ml of freshly prepared GPMV buffer (containing the active reagents of 25 mM formaldehyde and 1 mM dithiothreitol in the BB buffer), for one hour at 37°C with gentle shaking. GPMVs were then decanted into a centrifuge tube and allowed to sit for ~20 min. to let the cell debris settle. The supernatant was then transferred into a pre-equilibrated dialysis tube and dialyzed overnight with the BB buffer with 2mM Ca^{2+} and 0.01% of NaN_3. The dialysis buffer is changed once after 6 hours to completely eliminate dithiothreitol (DTT) and formaldehyde, and the required amounts of IgE are added (typically about 6 µg of IgE per T75 flasks). The PMV solution was transferred to a centrifuge tube and pelleted at 6° C for 40 min. at 12,000 rpm. The supernatant was removed and the pellet re-suspended in 1.6 ml of BB buffer containing 2mM Ca^{2+}, and 42 µl of 0.07 mM n-PC spin label (where n = 5, 7, 12, 16) was added. This solution was incubated at room temperature for 10-15 min. with occasional stirring and re-pelleted at 12,000 rpm for 20 min. at 8° C. The sample pellet was then transferred to an ESR sample tube and the ESR spectrum was measured using our 9 GHz Bruker ELEXYS-II E500 spectrometer at the desired temperature.

Cholesterol depletion with MβCD was carried out by adding 80 µl of 20mM MβCD in PBS/BSA buffer to about 0.8 ml of the sample in the bleb buffer (i.e., final concentration of MβCD was ~2 mM). After about 5mins, the bleb buffer containing MβCD was dialyzed with BB buffer to remove the MβCD completely. The samples were then pelleted in a similar fashion to the sample pellet for PMVs described above, and the cw-ESR spectra were measured. To carry out the crosslinking experiments the ESR sample pellet (used to measure the uncrosslinked sample above) was re-suspended in a small amount of BB buffer (~100-800 µl) and about 10-30 µl of 2.5 µM crosslinking agent

(trivalent DNP, Y_{16}-DNP_3[165]) was added. The solution was then centrifuged at 12,000 rpm for 20 min. at 4°C, the sample pellet was then transferred to an ESR capillary tube, and the spectra were observed. The continuous wave ESR measurements were carried out on the pelleted sample at two different temperatures (8° C and 37° C).

4.3. Results

4.3.1. Pulsed Dipolar Spectroscopy

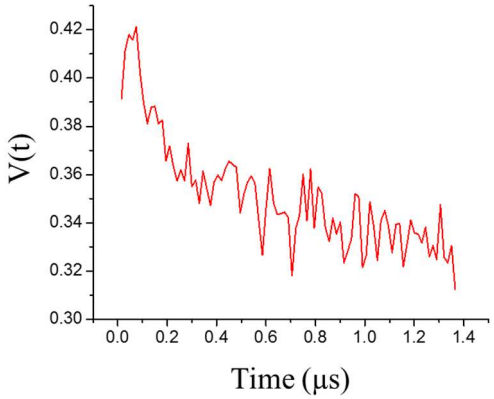

Figure 4-6: Time domain pulse dipolar signal (V(t)) of the spin-labeled IgE crosslinked with trivalent DNA-DNP_3 ligand. This data has not been baseline subtracted.

IgE in PBS/EDTA buffer was crosslinked with trivalent DNA-DNP_3 and the equilibrium PDS signal obtained. As seen in Figure 4-6, the PDS signal obtained for this experiment after overnight averaging (~18 hr.) was very weak. In fact, the signal obtained is so weak that it is difficult to determine the PDS signal background easily. This background always in DEER even with 100% labeling (caused by non-aggregated IgE) needs to be removed to obtain the relevant part of the signal. However, the background determination requires us to identify a log fit; this is unreliable in the case

where the spectra are so noisy. Therefore, a wavelet-based denoising approach developed by Srivastava et al[166] was recently used to help determine the background. This background was subtracted from both the noisy and denoised spectra to obtain the time-domain pulse dipolar signal (Figure 4-7 a). The distance distribution was initially obtained (Figure 4-7 b-c) using the L-curve based Tikhonov Regularization[68] method (TIKR) followed by refinement with the Maximum Entropy Method[70] (MEM).

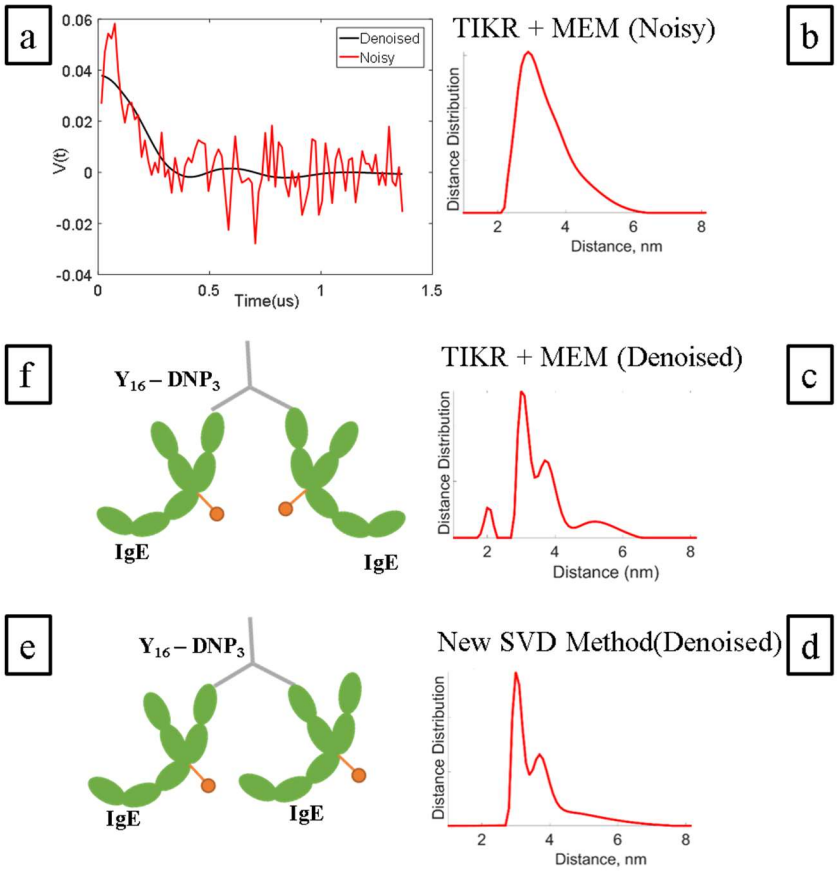

Figure 4-7: Distance distributions for spin labeled IgE crosslinked by Y_{16}-DNP_3. (a) Experimental time domain DEER data (noisy) along with wavelet denoised time domain DEER signal. (b) - (d): Reconstructed distance distribution for the noisy and denoised signal obtained using different reconstruction methods (TIKR/MEM and new SVD method). (e)-(f) Two potential orientations of the spin label in the IgE-(Y_{16}-DNP_3) complex that could explain the bimodal distribution observed in (d).

The distance distribution indicates a broad peak at ~3 nm (Figure 4-7 b) for the noisy spectra whereas the denoised PD distance distribution obtained using TIKR+MEM indicates peaks at 3, 3.7 and a broad peak at 5.2 nm (Figure 4-7 c). It is important to note that the peaks observed in the denoised distance distribution at and below two nm are unreliable and therefore not of importance. To avoid such artifact peaks such as those below 2 nm, a new SVD based method that was developed by Srivastava and Freed[72] and applied to this sample. This method for reconstruction of the PD distance distribution should be artifact free due to its good convergence. This method gave us two peaks, one at 3 nm and another at 3.7 nm with a long tail ~5 nm. The small peak observed at 5.2 nm in the TIKR+MEM reconstruction method is probably real and leads to the broad tail ~5 nm with the new SVD method. For the Y16-DNP_3 trivalent antigen, the distance between the antigen binding sites of two IgEs is ~5.2 nm. However due to the bent structure of IgE in solution[167], it is expected that the distance between the 'spin labeled' sites of IgE is between 3-5 nm (i.e., the distance between the inter heavy chain disulfide bridges of the neighboring IgEs is ~3-5 nm). Therefore the peaks at the 3, 3.8 nm distances could be expected for this sample depending on the orientation of the IgE molecule when bound to the DNP on the trivalent DNA molecule.[165] Figure 4-7 e-f shows two potential orientations of the IgE that can give the respective distances. It is important to note that this figure is a simplified two dimensional representation of an inherently three dimensional system.

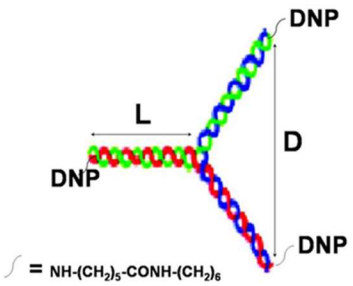

Name	L (nm)	D (nm)
Y16-DNP3	2.7	5.2 (±0.9)
Y26-DNP3	4.4	6.9(±1.3)
Y36-DNP3	6.1	10.4(±1.6)
Y46-DNP3	7.8	13.1(±2.5)

Figure 4-8: The rigid DNA spacer and distances. Left: Structure of the trivalent DNA ligand with variable space length. Right: Distance values (L & D) for the specified DNA spacer, our measurements used the Y16-DNP$_3$ spacer. Figure modified from Sil et al.[165] (2007)

4.3.2. Cholesterol depletion in the membrane

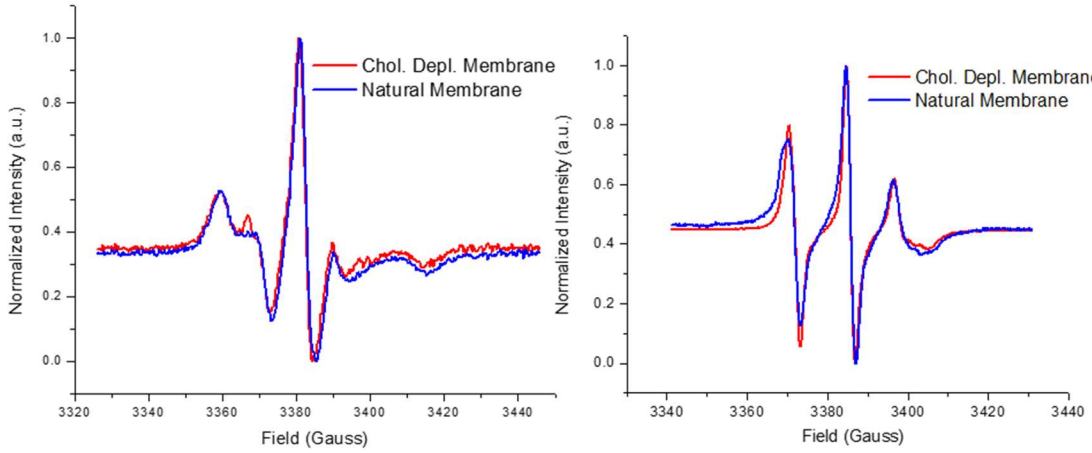

Figure 4-9: ESR spectra of 5-PC (left) and 16-PC (right) in natural and cholesterol-depleted plasma membrane vesicles obtained from RBL cells.

The 5-PC results are not surprising because they are largely excluded from the L_o phase and primarily report the L_d phase.[20,40] 5-PC's partition coefficient is 3:1 in favor of the L_d phase when compared to the L_o phase. Therefore, small changes in the fraction of L_o phase are unlikely to be observed by the 5-PC probe. However, significant changes to the ordering of the L_d phase will definitely be observed by the 5-PC probe. However,

this data from 5-PC clearly shows that the L_d phase behavior (Figure 4-9) is not greatly affected by the cholesterol depletion.

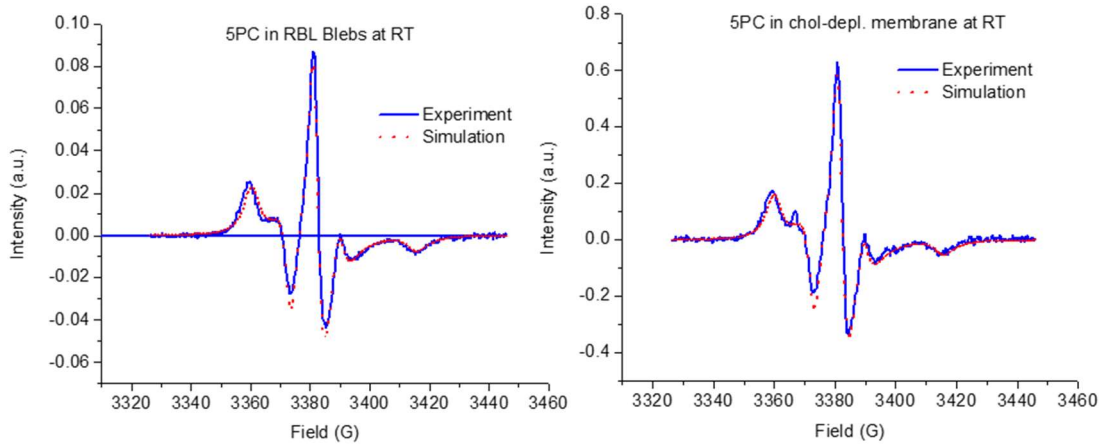

Figure 4-10: Comparison of simulated and experimental data for 5-PC in (left) natural membrane and (right) cholesterol-depleted membrane. For natural membrane ($\boldsymbol{R}_\perp$) = $3.7x10^7$ and S_0 = 0.39 whereas the cholesterol-depleted membrane is ($\boldsymbol{R}_\perp$) = $3.5x10^7$ and S_0 = 0.39. This indicates that there is not much change in the membrane spectra after cholesterol depletion for the 5-PC probe.

The 5-PC spectra were fit using the nonlinear least squares fitting program[96] to obtain the motional and ordering parameters. In the case of the cholesterol-depleted sample there is an insignificant decrease in the rotational rate ($R_\perp$), i.e., $R_\perp$value of 3.5 x $10^7 s^{-1}$ when compared to the $R_\perp$value of 3.7 x $10^7 s^{-1}$ for the natural membrane (Figure 4-10). The ordering parameter (S_0) does not change. However, the 16-PC probe clearly shows the effect of cholesterol depletion as seen in Figure 4-11. The effects of cholesterol depletion is most evident at the lower field positions (~3370 G), where the cholesterol-depleted ESR spectrum shows a much narrower feature than the natural membrane. This is because there is a larger amount of disorder observed in the system.

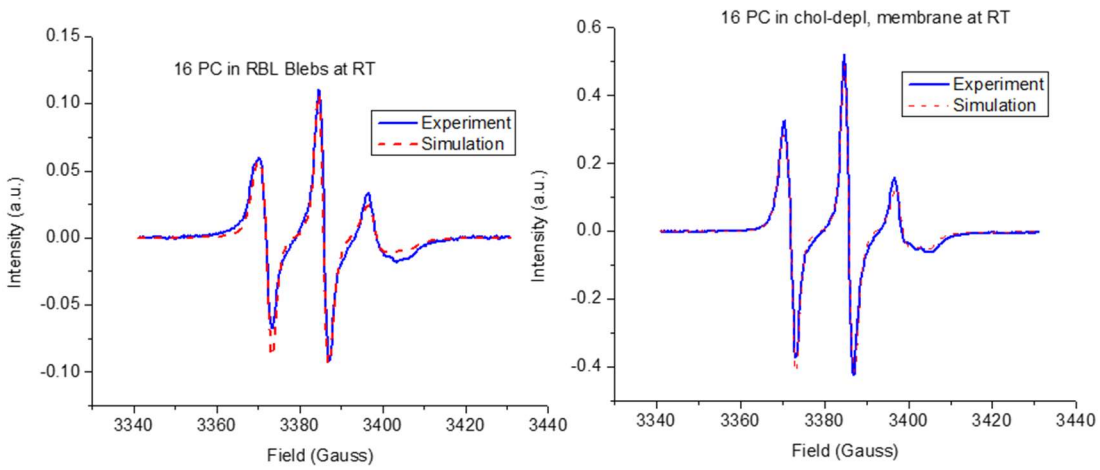

Figure 4-11: cw-ESR spectra observed for 16-PC probe in plasma membrane vesicles along with their respective fits. Fit parameters are tabulated in Table 4-1.

Table 4-1: Percentage of the L_d phase observed when cholesterol depletionis carried out along with the fit parameters obtained from NLSL fitting for the 16-PC probe.

Type of Membrane	**L_d parameters**	**L_o parameters**	**L_d fraction observed**
Natural	$R_\perp$ = 1.24 x $10^8 s^{-1}$ S_0 = 0.19	$R_\perp$ = 2.01 x $10^8 s^{-1}$ S_0 = 0.37	36.3
Cholesterol Depletion	$R_\perp$ = 1.23 x $10^8 s^{-1}$ S_0 = 0.19	$R_\perp$ = 5.27 x $10^8 s^{-1}$ S_0 = 0.27	65.2

NLSL fitting (Table 4-1) shows that the L_d phase of the 16-PC spectra shows that the L_d phase's motional and ordering parameters do not change very much (i.e., $R_\perp$ ~ 1.23 x $10^8 s^{-1}$ and S_0 = 0.19). The L_o phase does become more fluid and less ordered due to cholesterol depletion. This result is expected since cholesterol is required for the formation of the ordered phase (L_o).[3,28] Further, there is ~30% increase in the fraction of lipids exhibiting L_d phase behavior; these results obtained for this system are consistent with the results obtained by Levental et al.[163] (Figure 4-12).

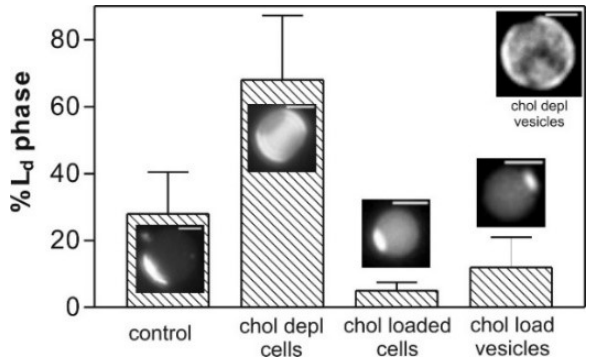

Figure 4-12: Fraction of L_d phase observed in GPMVs from NIH 3T3 fibroblasts as a function of cholesterol . The fraction of L_d phase increases from ~30% to ~65%, i.e., ~35% increase in the L_d phase for this sample. Figure modified from Levental et al.(2009)[163]

4.3.3. Changes to phase behavior due to antigen crosslinking as reported by cw-ESR

The cw-ESR spectra for the 12-PC and 16-PC probe (Figure 4-13) indicate that there is relatively very little change to the phase behavior when the IgE-receptors are crosslinked by multivalent antigens. A model system looking at crosslinking of peptides in membranes was developed and discussed further in Chapter 5.

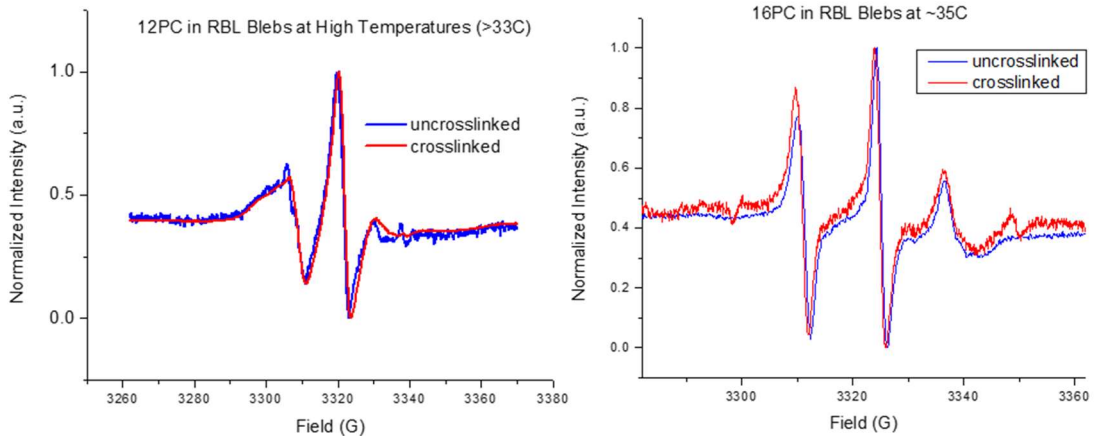

Figure 4-13: Measurement of changes to the ESR spectra for 12-PC (left) and 16-PC (right) probes for the crosslinked IgE-FcεRI receptors on plasma membrane vesicles (PMVs) obtained from RBL cells.

The ESR spectrum for the 16-PC probe shows two additional ESR peaks at 3300 and 3350 G; this is likely due to 16-PC to 16-PC probe interactions formed when large IgE-FCεRI crosslinked aggregates are formed on the membrane surface. However, these additional features are not always observed and therefore difficult to quantify using cw-ESR.

4.4. Conclusions and Future Directions

The complex natural membrane system of eukaryotic cells was studied using different ESR spectroscopic techniques. PDS was used to show the utility of this novel spin labeling technique using bidentate spin labels to identify the distance distribution for protein aggregates. However, the signal to noise ratio for this system is poor, so only the equilibrium distances of 3, 3.7 and 5.2 nm for our system could be measured. Further improvements in signal to noise ratio, by improvements to the PDS technique and instrumentation[67] as well as wavelet denoising[166] methods, are required to carry out future work on the time-dependent changes to distance distribution after IgE crosslinking by multivalent antigens. Cw-ESR was used to study the effect of cholesterol depletion in plasma membrane vesicles obtained from RBL cells, and it is observed that cholesterol depletion leads to an increase in the fraction of lipids exhibiting L_d phase behavior. Further work on studying changes to the phase behavior of lipid membranes due to the IgE-FcεRI also needs to be carried out using different crosslinking agents such as trivalent DNA-DNP_3, especially using advanced two-dimensional ESR techniques such as 2D-ELDOR as well as high frequency ESR.

4.5. Supplementary Information

4.5.1. Presence of Calcium

Calcium plays a major role in many cellular functions[168]. The binding of calcium to phosphatidylserine (PS) and other like negatively charged lipids[169] (e.g.: PG – phosphatidylglycerol) in the membranes significantly affects the phase behavior[170] as it induces PS crosslinking[171]. The presence of 2mM Ca^{2+} (i.e., physiologically relevant concentrations of calcium) induces large scale phase separation in lipid temperatures at low temperatures (<15 °C)[131]. However, the reason for this phase separation is poorly understood, especially if these changes are linked to changes to the phase behavior. ESR provides unique information as it largely provides information on the order parameter and motional dynamics of all the probes present in the sample independent of the size of the domains. Our results indicate (Figure 4-14) that there is very little change to the phase behavior associated with the calcium dependent phase separation.

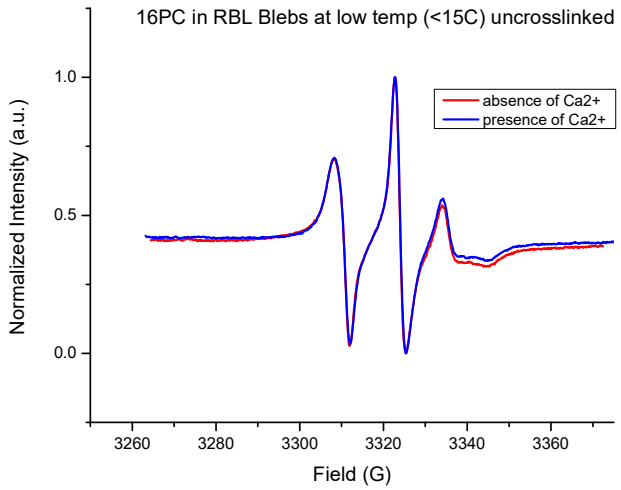

Figure 4-14: The ESR spectra of 16-PC probe in PMVs obtained from RBL cells at 8 °C in the presence and absence of calcium. The phase separation is observed for the plasma membrane vesicles (PMV's or blebs) in the presence of calcium using fluorescence imaging techniques.

CHAPTER 5 : CROSSLINKING OF BIOTINYLATED PEPTIDES IN MODEL MEMBRANES

5.1. Introduction

The cross-linking and/or aggregation of peptides and proteins in cellular membranes is a vital part of many membrane-linked cellular processes. The cross-linking of membrane proteins plays a major role in receptor signaling, viral budding, and vesicular transport. The exact mechanism for downstream processes involving protein cross-linking in membranes is not understood but it is observed that cross-linking of proteins induces formation of larger liquid ordered/domains. These larger domains can selectively recruit downstream signaling proteins (depending on the desired cellular response).[23,34,146,172] Currently, the extent of membrane restructuring induced by the cross-linking of proteins is poorly understood. Furthermore, very little information is available on the size of these lipid domains.

Natural membranes in their uncrosslinked states consist of liquid ordered nanodomains[26], the ordered domains have popularly been referred to as "lipid rafts." These lipid rafts are nanoscopic, varying between 10–200 nm, and are rich in sterols, sphingolipids and high melting lipids and are stabilized by protein and lipid interactions. The nanoscopic size of these domains make it difficult to study them with conventional spectroscopic techniques that are limited by the wavelength (~250 nm). Recent advances in super-resolution imaging and localization techniques have helped improve resolution by an order of magnitude, to almost ~20nm. However, this method is also complicated as these methods typically involve compiling many observed snapshots to

construct the "image." Moreover, this method can only indirectly give information about the phase behavior (by looking at "diffusion" rates in successive images).

Electron Spin Resonance (ESR) provides for an opportunity to observe sufficiently small domains as it observes the ensemble of all the spin probes present in the sample, provided, they are localized in these domains. Therefore, ESR can be used to report the phase behavior at both the nanoscopic as well as the macroscopic scale. Furthermore, ESR is extremely sensitive to the phase behavior of membrane systems and can be used to determine the exact change in the phase behavior.[1,3] Earlier, Chiang, et al.[20] have studied the cross-linking of IgE-FCεRI receptors by a multivalent antigen using the 2D electron–electron double resonance technique (c.f. Chapter 2). They found that membrane cross-linking increased the extent of disordering in the lipid membranes (Figure 5-1).

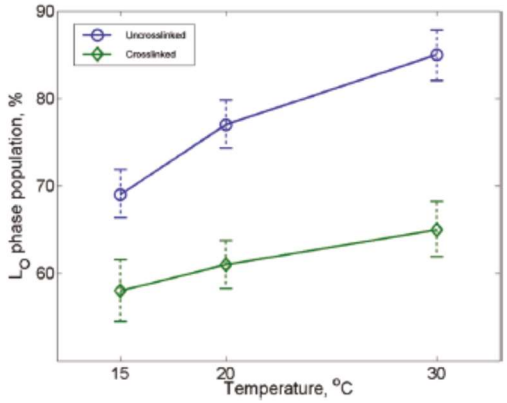

Figure 5-1: The change in the L_o fraction observed upon cross-linking of IgE receptor assembly in plasma membrane vesicles obtained from RBL cells. Figure was modified from Chiang et al. (2011).[20]

However, such studies on plasma membrane vesicles as well as cellular membranes are difficult due to a variety of factors. First, the ESR spin probes are reduced by reductases present in the cell membrane; this has not allowed for the longer signal averaging

required to obtain adequate signal to noise. Natural membranes contain substantial amounts of water molecules (i.e., “lossy” samples) and therefore are difficult to tune. The natural membranes contain more than thousand different types of proteins, so it is difficult to separate out only the cross-linking interactions from other non-specific interactions. Hence it is important to construct a model membrane system where only the cross-linking interactions can be carefully studied. Model membranes are stable and their exact composition can be controlled. To understand the effects of cross-linking in biological membranes, a model membrane system containing various lipid compositions in coexisting L_o/L_d phases similar to cell membranes was developed. The study was carried out in both the “nanoscopic” as well as “macroscopic” domain region; this permitted insights into size and composition-dependent cross-linking effects. The effects of cross-linking on the phase behavior by using spin-labeled molecules (16PC spin label) was monitored using conventional 9-GHz cw-ESR. For this study, biotinylated transmembrane peptide (biotin moiety attached to C-terminus of the peptide) was used, and the changes to the ESR spectra upon avidin cross-linking were observed.

5.1.1.Biotinylated Gramicidin and Avidin cross-linking

Gramicidin is an antimicrobial pentapeptide that is produced by the soil-based bacterium *Bacillus brevis*. Gramicidin-A, the most abundant form of gramicidin, is made up of alternating D & L-amino acids: HCO-L-Val^{1}-Gly^{2}-L-Ala^{3}-D-Leu^{4}-L-Ala^{5}-D-Val^{6}-L-Val^{7}-D-Val^{8}-L-Trp^{9}-D-Leu^{10}-L-Trp^{11}-D-Leu^{12}-L-Trp^{13}-D-Leu^{14}-L-Trp^{15}-$NHCH_2CH_2OH$ (cf. Figure 5-2).

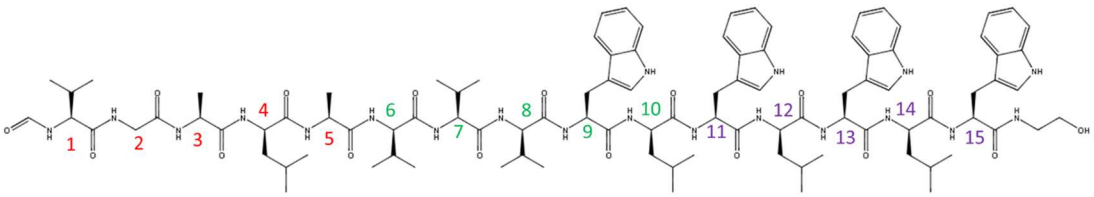

Figure 5-2: Structure of Gramicidin A along with the amino acid sequence.

The amino acids in gramicidin are either hydrophobic (Val, Ala, Leu) or amphipathic (Trp). The Trp residues (amino acids 9, 11, 13, 15 in the sequence, carboxy terminus), are present in the membrane interface due to their amphipathic nature while the hydrophobic amino acids (amino acids-1-10, amino terminus) are buried in the membrane bilayer. Gramicidin-A adopts a single stranded helical dimer (known as the channel form) in lipid bilayers.[173] A single molecule of Gramicidin-A is unable to traverse the membrane, so it forms end-to-end dimers between two gramicidin molecules linked together at the amino terminus (N-terminus). Gramicidin-A's principal state in the membrane is the dimer form with the dimerization constant ($>10^{13}$ cm^2/mol) in the fluid membrane phase being very high. Once the gramicidin-A dimer forms in the membrane, it is held together by six hydrogen bonds. Therefore, it is important to biotinylate gramicidin only at the carboxy terminus (C-terminus). Gramicidin-A's surface area is significantly more than that of the lipids in the bilayer; it can occupy up to 20% of the entire surface area of the membrane.[174] This can lead to large and significant changes in the membrane phase behavior.

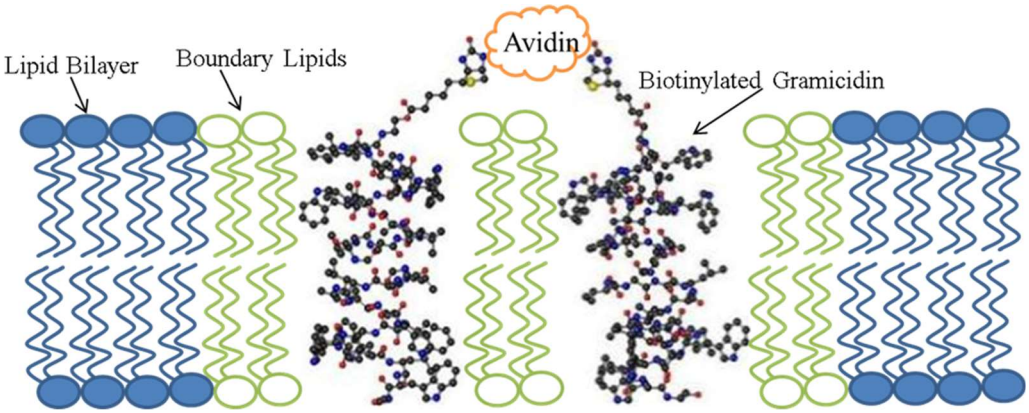

Figure 5-3: The cross-linking of biotinylated gramicidin in the membrane by Avidin.

Spin-labeled ESR has been used extensively to study gramicidin and its derivatives[33,53,54,175–177] in membranes. These studies have shown that gramicidin alters lipid membrane phase behavior at sufficiently high concentrations[175,176] while the 2D-ELDOR technique was used to distinguish between the bulk and boundary lipids as well as their aggregation.[33,53] Furthermore, biotinylated gramicidin (i.e., a biotin molecule attached to the C-terminus of Gramicidin) was chosen as a good model for studying membrane cross-linking effects, because this peptide is relatively stable and has a very simple structure that makes it easy to study the specific lipid-peptide interactions easily. The specific binding between avidin and biotin is very high ($K_a \sim 10^{15}$ mol^{-1}) and has been extensively used to introduce aggregation in a variety of systems. Avidin is a tetrameric protein with a molecular weight of ~68 kDa; an avidin molecule can bind up to 4 different biotin moieties. This property is used to coordinate biotin ligands from different biotinylated gramicidin peptides, therefore leading to cross-linking of the peptides.[178,179] As gramicidin forms end-to-end dimers, it can aid in forming extended networks (i.e., more than two gramicidin can be linked together) of biotinylated gramicidin (Figure 5-3). The distance between two biotin-binding sites on the "same

face" of avidin as needed for cross-linking is ~2 nm (Figure 5-4), therefore we expect the gramicidin-gramicidin distance upon crosslinking to be around ~2.5 nm.

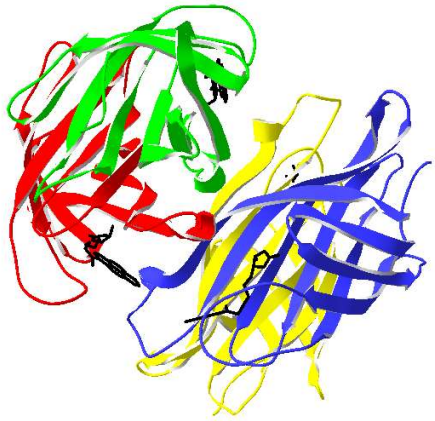

Figure 5-4: The structure of the biotin-avidin complex. Avidin is shown in its tetrameric form (red, blue, green and yellow domains) and the biotin sites are shown in black. On average the distance between the two biotin sites on the same face are ~2 nm. This structure is based on the crystal structure (5IRW).[180]

5.2.Experimental

5.2.1. Synthesis of Biotinylated Gramicidin

Biotin (6 mg) and Gramicidin-D (49 mg) were dissolved in 0.5ml of dry dimethylformamide (DMF) along with a pinch of 4-Dimethylaminopyridine (DMAP) and Hydroxybenzotriazole (HOBt) (0.32 mg). This mixture was heated gently to obtain a homogenous solution. 25µl of 1M N,N'-Dicyclohexylcarbodiimide (DCC) in chloroform ($CHCl_3$) was carefully added at room temperature and stirred for ~48 h. The reaction (Figure 5-5) was stopped by evaporating the DMF in a rotovap heated to 80 °C. The reaction mixture was then placed in a vacuum desiccator overnight to remove any residual DMF. Large scale (preparative) TLC was performed to separate out the

different reaction products by running the reaction mixture against 5:1 Chloroform/Methanol on a silica plate. The TLC indicated three bands with the upper band containing gramicidin and its derivatives. Mass spectrometry was used to identify the reaction product (cf. Figure 5-11 in the supplement). Gramicidin (GD) and Biotinylated gramicidin (BG) are not easily separated by the 5:1 $CHCl_3$: MeOH mixture, however as most of the gramicidin was converted into the product and further separation between GD and BG was not critical for further experiments. This procedure was modified from similar experiments in the literature.[54,181]

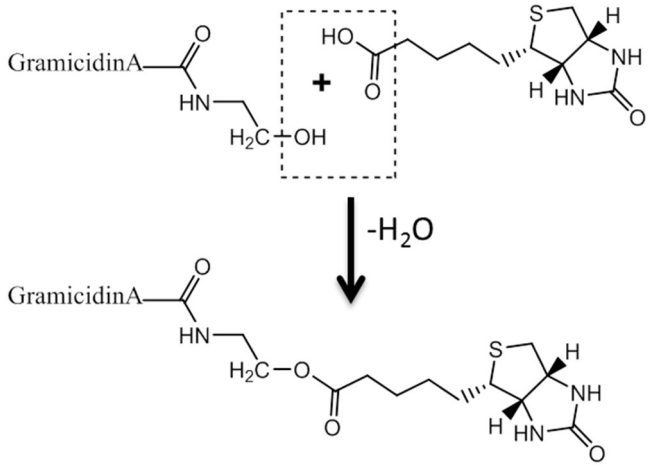

Figure 5-5: Basic scheme for the biotinylation of gramicidin-A at the C-terminus , based on the Steglich Esterification reaction.[182]

5.2.2.Preparation of lipid membranes

The lipids for each sample were mixed in a pre-determined ratio of the individual components (cf. Table 5-1 and Table 5-2) in chloroform and 0.3 mole percent of 16PC was added, 0.5-1.0% of gramicidin or biotinylated gramicidin was also added. The chloroform in this lipid mixture was evaporated under a flow of pure nitrogen gas and

then completely dried in a vacuum desiccator overnight (>8 hr.). About 0.5 ml of PBS buffer at pH 7.4 was added to the dried lipids and was hydrated for at least one hour at ~47 ℃ with rapid vortexing every 15 min. This process produces a turbid solution that is made up of multilamelar lipid vesicles (MLV). The MLV solutions were then transferred to 2 ml centrifuge tubes and centrifuged at 14,000 g and 4 ℃ for 30 min. The supernatant was carefully removed, leaving behind ~80 µl of water and the lipid pellets containing MLVs. The pellets were re-suspended in the remaining water (~80 µl) and transferred to an ESR capillary tube. The sample was finally re-pelleted at 3,300 g and the supernatant was removed; a small layer of water (~1-2 µl) was left behind to prevent oxidation of the sample. The capillary tubes were carefully sealed to prevent evaporation and oxidation. The total weight of the lipids varied between 2-4 mg.

Table 5-1: Lipid compositions for the pure phases and their compositions [23]

DOPC/DOPG/Sph /Chol Composition	***Phases***
44.1/4.9/20/30	Liquid Disordered (L_d)
9/1/53/35	Liquid Ordered (L_o)

Table 5-2: Lipid compositions used in this study for the coexistence region. These values are the same as the lipid compositions used for the Chol 22 line in Chapter 3.

Rho value (ρ)*	***DSPC/DOPC/POPC/Chol Composition***	***Size of Domains (in MLVs)***
0.0	*39/0/39/22*	Nanodomains (L_o & L_d)
0.1	*39/4/35/22*	Nanodomains (L_o & L_d)
0.5	*39/20/19/22*	Macrodomains (L_o & L_d)
1.0	*39/39/0/22*	Macrodomains (L_o & L_d)

** The rho value is the relative fraction of DOPC with respect to POPC, i.e. higher rho values indicate DOPC rich compositions while lower rho values indicate POPC rich compositions.*

5.2.3. Cross-linking with Avidin

For the cross-linking measurements, to increase the accessibility of the biotinylated gramicidin to the avidin molecule, sonicated vesicles were prepared. These sonicated vesicles are prepared by sonicating the MLV solution with a probe tip sonicator for five mins, this sonication allows for the proper mixing of all the components. To carry out the cross-linking, a slight excess amount of avidin was added (i.e., ~one avidin molecule was added for 3.9-4 molecules of biotinylated gramicidin). Avidin from egg white was purchased from Sigma Aldrich and a stock solution containing 5 mg/ml of Avidin was prepared in the PBS buffer at pH 7.4. The sonicated vesicles so obtained are difficult to pellet, the presence of large amounts of water in the sample lowers the spin label concentration and therefore makes it difficult to obtain strong enough ESR signal. These samples were therefore left overnight (~8 hr.) at 4 ℃ to allow them to settle by gravity. In the case that avidin was added to crosslink the biotinylated gramicidin, it was added during the sonication step to ensure that the crosslinking process was completed. This sample was then pelleted in a process similar to MLVs stated above to measure the ESR spectra.

5.2.4.Spectral Acquisition and Processing

The ESR spectra were obtained on a commercial Bruker ELEXSYS (E500) CW-ESR spectrometer at room temperature (~293-297 K). The ESR spectra so obtained were converted into ASCII format and then analyzed using the non-linear least squares analysis program[96] developed by the Freed group and by custom-built programs in MATLAB®. The spectra in this study were obtained for end-chain label 16PC (1-palmitoyl-2-stearoyl-(5-doxyl)-sn-glycero-3-phosphocholine), as this probe partitions equally between the L_o and L_d phases and therefore is the most sensitive to changes in the phase behavior.

5.3. Results

5.3.1. Effect of Gramicidin on the phase behavior of the cell membrane

The presence of gramicidin in the membrane has been shown to alter the phase behavior of the model membrane system.[175] This could be problematic if the presence of gramicidin prevents the formation of nanodomains and/or changes the domain size. Therefore, a sufficiently low concentration of gramicidin needs to be chosen. Earlier studies have indicated that low concentrations (~0.4%)[54] of gramicidin do not alter phase behavior very much. Therefore, gramicidin concentration of 0.5 mol % (i.e., one gramicidin per 200 lipid molecules) was chosen. Figure 5-6 shows that the presence of gramicidin does not change the phase behavior of the lipid membrane at such low concentrations. The lipid composition chosen in Figure 5-6 was the most restrictive case with the smallest domain size (~7 nm).[138]

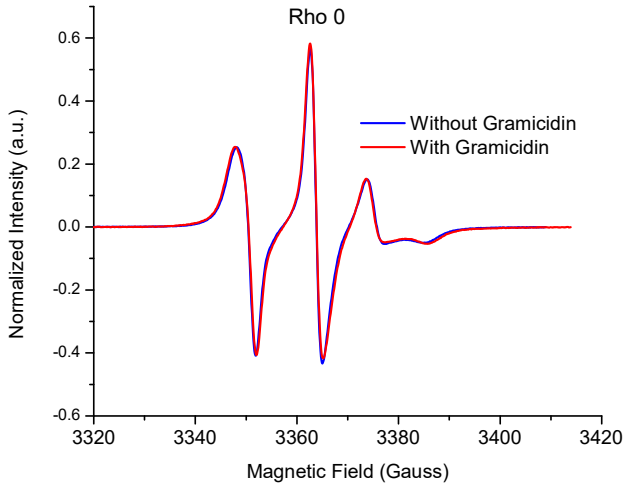

Figure 5-6: ESR spectrum of DSPC/DOPC/POPC/Chol lipid mixture at room temperature containing (a) no gramicidin and (b) 0.5 mol % of biotinylated gramicidin.

5.3.2. Effect of cross-linking on single phase systems

The effect of avidin cross-linking on the phase behavior of pure phases (i.e., the lipid composition chosen was in a single phase) was carried out both in MLVs and sonicated vesicles. These experiments (Figure 5-7) indicate that single-phase spectra are not affected by the cross-linking of biotinylated gramicidin at the low concentrations used.

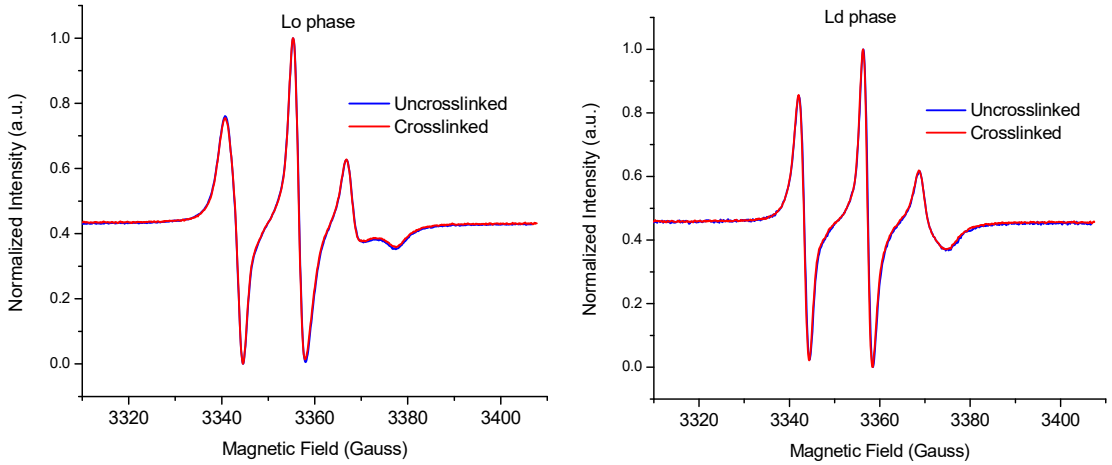

Figure 5-7: Comparisons of pure phase spectra of the (left) Lo phase and (right) Ld phase, with and without the presence of crosslinked biotinylated gramicidin The pure phase spectra show no significant changes to their spectra upon cross-linking.

5.3.3. Effect of cross-linking on coexisiting phases

Cross-linking of biotinylated gramicidin in the membrane was first carried out in multilamellar vesicles (MLVs). No significant changes to the phase behavior were obtained; this was likely due to restricted access to the biotinylated gramicidins on the membrane surface for the avidin molecule. Therefore, efforts were focused on studying the cross-linking effects in the sonicated vesicles. Figure 5-8 shows the ESR spectra for two different lipid compositions. As seen in Chapter 3, the Rho 0 composition is POPC-rich and in the nano-domain region while the Rho 1 composition is DOPC rich and in the macrodomain region.[136,140] As seen in Figure 5-8, the spectra for Rho 0 composition show a significant change in the spectra while the spectra for Rho 1 composition do not change very much. The differences are clearly evident in the high field region of the spectra (~3380 G) for Rho 0, where the uncrosslinked gramicidin has a double dip feature (signifying greater order) while the crosslinked gramicidin has only one broad feature.

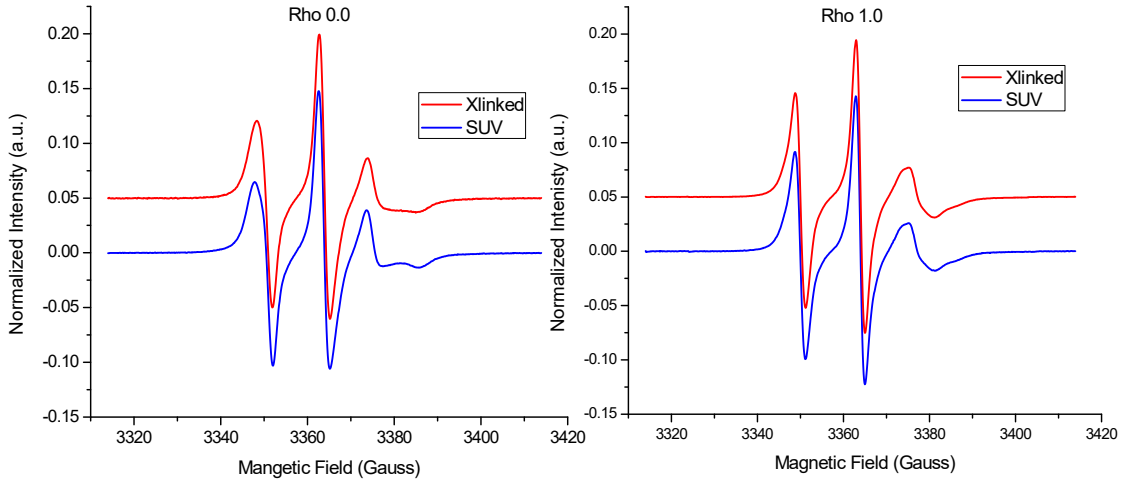

Figure 5-8: ESR spectrum of the DSPC/DOPC/POPC/Chol system for two different compositions. (cf. Table 5-2).

The uncrosslinked and crosslinked data were fit by performing a linear combination of the L_o and L_d phases in MATLAB as described in Chapter 3. Figure 5-9 shows the best fits obtained for the case of Rho 0.5 (both uncrosslinked and crosslinked) along with the residuals from the fit. As can be seen the two component fits are accurate and account for all the major features. A selection of these ESR spectra were also fit using the non-linear least squares fitting method (NLSL)[96] and the two component NLSL fits obtained had similar residuals to the linear combination (of L_o and L_d) method. So only the results from the linear combination fit method are discussed henceforth. The NLSL results show that the rotational diffusion parameter ($R_\perp$) for the L_o phase is ~3.5×10^8 s^{-1} while that for the L_d phase is ~2.8×10^8 s^{-1}. The order parameter (S_0) is significantly higher for the L_o phase (~0.35) when compared to the L_d phase (~0.12).

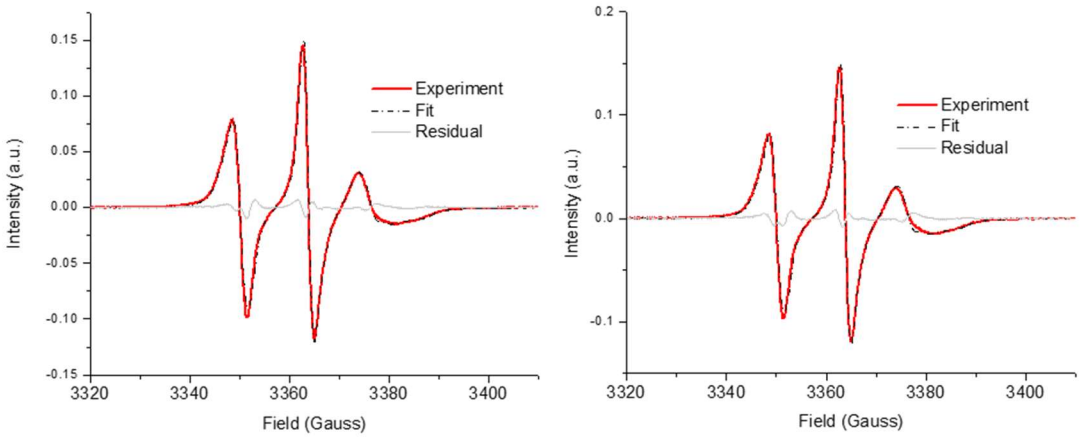

Figure 5-9: The results for the two component of the ESR spectrum for the rho 0.5 composition is shown for the uncrosslinked (left) and the crosslinked (right) sample.

Similar to the Rho 0.5 case, the four different compositions were fit by combining the spectra from the L_o and L_d components. A summary of these results given in Figure 5-10, show that the L_o phase is the predominant phase in both the uncrosslinked and crosslinked state for the lower rho values (below 0.3) while the L_d phase is the

predominant phase for the higher rho values. Furthermore, this figure shows that the L_o fraction reduces on cross-linking, i.e., cross-linking introduces a larger amount of disorder in the domain. This effect of cross-linking is more marked in the case of compositions rich in POPC. In the case of Rho 0, cross-linking reduces the amount of the ordered phase in the sample by almost 12% (from 80% to around 68%), while in the case of Rho 1 the change in the ordered phase is within the error levels of the fit. Therefore, this effect of cross-linking appears to be very composition (and possibly size) dependent.

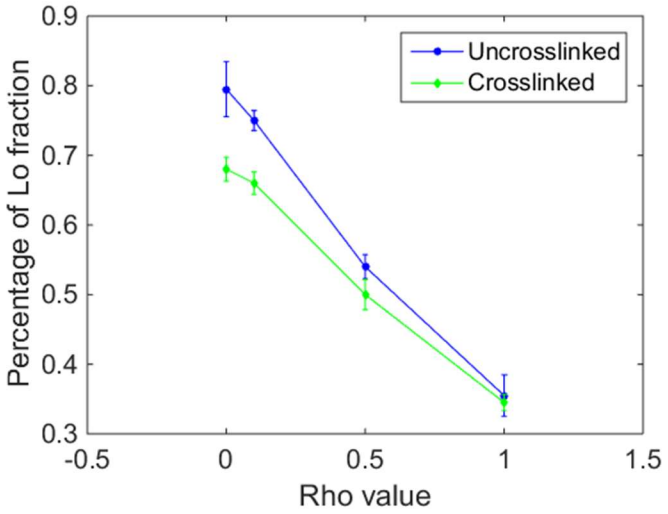

Figure 5-10: Ratio of L_o fraction for the uncrosslinked and crosslinked membrane system plotted against the rho value. The error bar is indicative of the residual levels from the fit, therefore informs of the accuracy of the fit. The ordering and dynamic properties of both the L_o and L_d components was not changed between the crosslinked and uncrosslinked sample.

These results are also consistent with the data obtained by Chiang et al.[20] (cf. Figure 5-1), where they observe that cross-linking of IgE-FCεRI receptors by multivalent antigen induces disorder in the plasma membrane vesicles obtained from the RBL cells. Gramicidin is known to prefer the L_d domain and the "boundary lipids" in the near

vicinity of gramicidin are known to behave in a disordered fashion.[33] Therefore, it appears that gramicidin cross-linking "releases" these lipids to increase the amount of total disorder in the system. However, to study the effect of the lipid domain boundary, a higher resolution technique like 2D-ELDOR is required.

5.4. Conclusion

A model membrane system using biotinylated gramicidin was constructed to understand the effects of peptide/protein cross-linking in the membrane. Continuous wave (cw) ESR was used to characterize the changes to the phase behavior induced by the cross-linking of gramicidin. No changes were observed when the system exhibited only one phase. In the case of coexisting L_o and L_d phases, cross-linking of biotinylated gramicidin in the membrane increased the fraction of the disordered phase; these results are consistent with other studies carried out with ESR[20]. Furthermore, substantial changes to the membrane phase behavior were observed in the case of POPC rich compositions while little to no change was observed in the case of DOPC rich compositions. This domain-size dependent effect of cross-linking might be important for biology and can give us clues about behavior of natural membranes. However, further work using peptides favoring the L_o domain need to be studied as well. Finally, advanced measurements using higher resolution ESR techniques such as 2D-ELDOR can help better separate the L_o and L_d domains and give insights into nature of the composition and domain-size dependent effect.

5.5. Supplementary Information

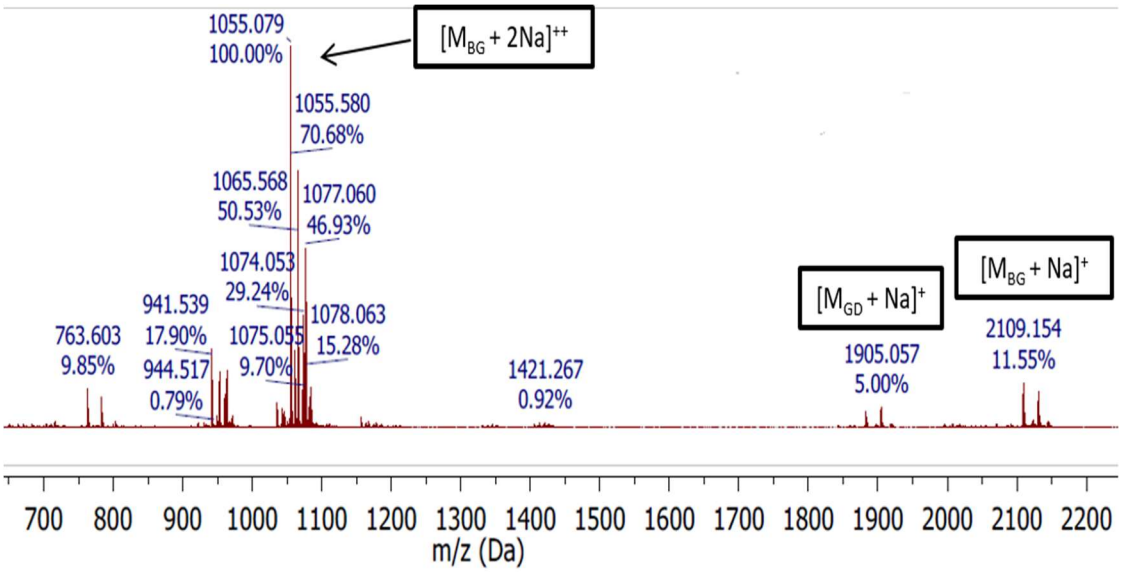

Figure 5-11: Mass spectrum (ESI-MS) of the biotinylation of gramicidin reaction mixture , the mol. wt. of gramicidin (GD) is 1882.3 g/mol; the peak at 1905.1 is the $[M_{GD} + Na]^+$ *and the peak at 2109.2 is the* $[M_{BG} + Na]^+$*. The* $[M_{BG} + 2H]^{2+}$ *and* $[M_{GD} + 2H]^{2+}$ *peaks are observed at 941.5 and 1055.1 respectively. The mass spectral peaks indicate that bulk (~70%) of the initial gramicidin (GD) was converted into biotinylated gramicidin (BG).*

CHAPTER 6 : CONCLUSIONS

In this section, I will summarize some of the results obtained during my graduate study. As each chapter has a slightly different objective, I will address this by the chapter:

In chapter 2, we have studied the partitioning of TEMPO into lipid membranes using 95 GHz 2D-ELDOR spectroscopy:

(1) We have developed a high power high frequency pulsed ESR spectrometer that can be used to study "lossy" aqueous samples at room temperature. We have used this spectrometer to study the partitioning of spin label (TEMPO) between the water and lipid phases. This is a significant achievement for the field of ESR spectroscopy, because very few high frequency studies (95GHz or higher) have been carried out on lipid membranes. We have earlier addressed the challenges of using pulsed 2D-ESR techniques to study molecular motions at higher frequencies.[6]

(2) We showed that the utility of high frequency ESR in providing improved spectral resolution to separate out the lipid and water phase peaks based on the differences in their g-values and hyperfines.

(3) We observe that the spin label partitioned into the lipid membrane is located close to the interface of the lipid and water phases. Using 2D-ELDOR spectroscopy, we are able to simultaneously measure the T_1 and T_2 relaxation rates in both the phases. Further, the use of full Sc-. method developed by our group has made it possible to obtain accurate motional rates for the lipid and water phases.

(4) We observe that relaxants such as nickel and oxygen enhance spin relaxation in both the water and lipid phases but have differing effects in both: whereas oxygen has nearly the same effect on both the water and lipid phase, nickel largely affects the water phase signal and has a smaller effect on the lipid phase signal. There are still some unanswered questions with regard to the relaxation enhancement (RE) of the lipid phase by nickel, as we observe a greater enhancement than expected of the T_2 than the T_1. This effect is rather surprising for nickel because nickel induces relaxation primarily by collisional exchange (for collisional exchange, RE of T_2 = RE of T_1). This needs to be studied in detail with a series of different nickel concentrations and salts.

(5) Finally but most importantly, for the first time in the field of ESR spectroscopy we observe the effect of exchange of the TEMPO molecule between the lipid and the water phases. We find that the exchange of TEMPO between the lipid and the water phases is in the microsecond (μs) regime. This result is exciting because there are many biological processes that occur on this time scale, e.g. it will be great to observe the rate of conformational changes in protein structures.

In Chapter 3, we have studied nanoscopic domains formed in four component model membranes (in collaboration with the Feigenson group):

(1) We have used multifrequency (9 & 95 GHz) cw-ESR to study the formation of nanoscopic domains in tertiary lipid mixtures (DSPC/DOPC/POPC/Chol). The formation of nanodomains from macro-domains was studied along a compositional trajectory by varying the relative amounts of DOPC and POPC lipids while holding the

cholesterol and DSPC concentration constant. The relative fraction of DOPC present in the sample was represented by the rho (ρ) value defined as $\rho = \frac{\chi_{DOPC}}{\chi_{DOPC} + \chi_{POPC}}$.

(2) The Feigenson group earlier found that for the Chol 22 (mol. fraction of Chol = 0.22) trajectory, as DOPC was replaced with POPC, the fraction of lipid spin probes exhibiting L_o behavior increased (i.e., as the rho value decreased the fraction of L_o increased). We had determined the partition coefficient of 16-PC to be ~1.38±0.3[140]. These results agree with earlier results obtained by Swamy et al.[19] This data also shows that the transformation from macrodomains to nanodomains (i.e., size scale transition) does not affect the phase behavior drastically.

(3) We have further studied the Chol 22 trajectory using 95 GHz cw-ESR spectroscopy, as the enhanced g- and orientational- resolution obtained using HF-ESR could help further resolve the spectra of the L_o and L_d phases. This is one of the first instances where coexisting fluid domains have been studied with 95 GHz cw-ESR spectroscopy.

(4) We carried out non-linear least squares fitting for the 9 and 95 GHz cw-ESR data individually using the MOMD model. We used the 95 GHz cw-ESR data to obtain the $R_{\|}$ rates; this information is not accessible from 9 GHz cw-ESR fits. The $R_{\|}$ rates are usually slower than the $R_{\perp}$ by around an order of magnitude.

(5) Further, simultaneous fitting of the 9 and 95 GHz spectra with the SRLS model was carried out to obtain parameters for the global motion of the spin label.

(6) We have also studied the Chol 26 trajectory (i.e., with 26 mole percent of cholesterol). For this trajectory we also observe that the decrease in the rho value also

lead to an increase in the L_o fraction. These results follow a similar trend to Chol 22 with a slightly different K_p value of 1.15±0.15.

(7) We observe that the 9 and 95 GHz ESR indicate the presence of a third (possibly a boundary) region that has intermediate properties between the L_o and L_d domains. Further studies using advanced techniques like 2D-ELDOR spectroscopy are required to better characterize this third component.

In Chapter 4, we have studied the IgE-FcεRI receptor assembly in the plasma membrane of RBL cells (in collaboration with the Baird-Holowka group)

(1) We used a multipronged ESR approach for this project, Pulse Dipolar Spectroscopy (PDS) was used to measure the distance distribution of the IgE complexes formed by crosslinking with a trivalent antigen while cw-ESR was used to characterize the membrane phase behavior upon antigen crosslinking or cholesterol depletion.

(2) We have obtained distances in the range of 3-5 nm for IgE crosslinked in solution by trivalent DNA-DNP_3, these distances can be expected for inter IgE distances upon crosslinking. This measurement was vital to show the potential of PDS to work with sub micro-molar spin label concentration (i.e., conc. of spin labeled IgE ~ 0.5μM).

(3) The PDS signals we obtained from these samples were so "weak" that wavelet denoising method was used to improve the signal to noise ratio. Further, a new SVD based distance reconstruction method was also applied to obtain an artifact-free distance distribution.

(4) We have also studied the effect of cholesterol depletion on plasma membrane vesicles obtained from RBL cells. The cw-ESR results indicate that cholesterol

depletion by methyl-beta-cyclodextrin (MβCD) leads to an increase in the disordered (L_d) phase.

(5) We did not observe any changes to the phase behavior upon crosslinking with multivalent antigen using cw-ESR. So further studies using advanced techniques like 2D-ELDOR[20] spectroscopy is required to attempt to obtain this information. A model system similar to this system was developed and discussed further in chapter 5.

In chapter 5, we have studied the crosslinking of biotinylated peptides in model membranes:

(1) We developed a model membrane system based on the crosslinking of biotinylated gramicidin in membrane. The advantage of this system was that the concentration of gramicidin as well as the composition of the lipids could be varied to enhance the crosslinking effects.

(2) We observed that lipid compositions containing single phase (either L_d or L_o) did not show any appreciable changes upon crosslinking of biotinylated gramicidin.

(3) Further, we see that lipid compositions rich in POPC (typically exhibiting nanoscopic domains) show significant changes, particularly the L_d fraction is increased, while the compositions rich in DOPC (typically macro domains) show no change.

(4) These results are promising and show that this system is well designed to probe changes to the cw-ESR spectra upon crosslinking of peptides in membranes. Additional measurements using different types of peptides such as biotinylated WALP need to be carried out to further characterize this effect.

BIBLIOGRAPHY

(1) Borbat, P. P.; Costa-Filho, A. J.; Earle, K. A.; Moscicki, J. K.; Freed, J. H. Electron Spin Resonance in Studies of Membranes and Proteins. *Science* **2001**, *291* (5502), 266–269.

(2) Schneider, D. J.; Freed, J. H. Spin Relaxation and Motional Dynamics. *Adv. Chem. Phys.* **1989**, *73*, 387–527.

(3) Dzikovski, B.; Freed, J. H. Membrane Fluidity. In *Wiley Encyclopedia of Chemical Biology*; Begeley, T. P., Baird, B., Eds.; John Wiley & Sons, Inc.: Hoboken, NJ, USA, 2008; Vol. 2, pp 728–741.

(4) Misra, S. K.; Freed, J. H. Molecular Motions. In *Multifrequency Electron Paramagnetic Resonance*; Misra, S. K., Ed.; Wiley-VCH Verlag GmbH & Co. KGaA: Weinheim, Germany, 2011; pp 497–544.

(5) Freed, J. H.; Bruno, G. V.; Polnaszek, C. F. Electron Spin Resonance Line Shapes and Saturation in the Slow Motional Region. *J. Phys. Chem.* **1971**, *75* (22), 3385–3399.

(6) Franck, J. M.; Chandrasekaran, S.; Dzikovski, B.; Dunnam, C. R.; Freed, J. H. Focus: Two-Dimensional Electron-Electron Double Resonance and Molecular Motions: The Challenge of Higher Frequencies. *J. Chem. Phys.* **2015**, *142* (21), 212302.

(7) Liang, Z.; Freed, J. H. An Assessment of the Applicability of Multifrequency ESR to Study the Complex Dynamics of Biomolecules. *J. Phys. Chem. B* **1999**, *103* (30), 6384–6396.

(8) Meirovitch, E.; Nayeem, A.; Freed, J. H. Analysis of Protein-Lipid Interactions Based on Model Simulations of Electron Spin Resonance Spectra. *J. Phys. Chem.* **1984**, *88* (16), 3454–3465.

(9) Polimeno, A.; Freed, J. H. Slow Motional ESR in Complex Fluids: The Slowly Relaxing Local Structure Model of Solvent Cage Effects. *J. Phys. Chem.* **1995**, *99* (27), 10995–11006.

(10) Chiang, Y.-W.; Shimoyama, Y.; Feigenson, G. W.; Freed, J. H. Dynamic Molecular Structure of DPPC-DLPC-Cholesterol Ternary Lipid System by Spin-Label Electron Spin Resonance. *Biophys. J.* **2004**, *87* (4), 2483–2496.

(11) Costa-Filho, A. J.; Shimoyama, Y.; Freed, J. H. A 2D-ELDOR Study of the Liquid Ordered Phase in Multilamellar Vesicle Membranes. *Biophys. J.* **2003**, *84* (4), 2619–2633.

(12) Barnes, J. P.; Liang, Z.; Mchaourab, H. S.; Freed, J. H.; Hubbell, W. L. A Multifrequency Electron Spin Resonance Study of T4 Lysozyme Dynamics. *Biophys. J.* **1999**, *76* (6), 3298–3306.

(13) Liang, Z.; Lou, Y.; Freed, J. H.; Columbus, L.; Hubbell, W. L. A Multifrequency Electron Spin Resonance Study of T4 Lysozyme Dynamics Using the Slowly Relaxing Local Structure Model. *J. Phys. Chem. B* **2004**, *108* (45), 17649–17659.

(14) Zhang, Z.; Fleissner, M. R.; Tipikin, D. S.; Liang, Z.; Moscicki, J. K.; Earle, K. A.; Hubbell, W. L.; Freed, J. H. Multifrequency Electron Spin Resonance Study of the Dynamics of Spin Labeled T4 Lysozyme. *J. Phys. Chem. B* **2010**, *114* (16), 5503–5521.

(15) Lou, Y.; Ge, M.; Freed, J. H. A Multifrequency ESR Study of the Complex Dynamics of Membranes. *J. Phys. Chem. B* **2001**, *105* (45), 11053–11056.

(16) Singer, S. J.; Nicolson, G. L. The Fluid Mosaic Model of the Structure of Cell Membranes. *Science* **1972**, *175* (4023), 720–731.

(17) Simons, K.; Ikonen, E. Functional Rafts in Cell Membranes. *Nature* **1997**, *387* (6633), 569–572.

(18) Ge, M.; Gidwani, A.; Brown, H. A.; Holowka, D.; Baird, B.; Freed, J. H. Ordered and Disordered Phases Coexist in Plasma Membrane Vesicles of RBL-2H3 Mast Cells. An ESR Study. *Biophys. J.* **2003**, *85* (2), 1278–1288.

(19) Swamy, M. J.; Ciani, L.; Ge, M.; Smith, A. K.; Holowka, D.; Baird, B.; Freed, J. H. Coexisting Domains in the Plasma Membranes of Live Cells Characterized by Spin-Label ESR Spectroscopy. *Biophys. J.* **2006**, *90* (12), 4452–4465.

(20) Chiang, Y.-W.; Costa-Filho, A. J.; Baird, B.; Freed, J. H. 2D-ELDOR Study of Heterogeneity and Domain Structure Changes in Plasma Membrane Vesicles upon Cross-Linking of Receptors. *J. Phys. Chem. B* **2011**, *115* (35), 10462–10469.

(21) Sengupta, P.; Hammond, A.; Holowka, D.; Baird, B. Structural Determinants for Partitioning of Lipids and Proteins between Coexisting Fluid Phases in Giant Plasma Membrane Vesicles. *Biochim. Biophys. Acta - Biomembr.* **2008**, *1778* (1), 20–32.

(22) Baumgart, T.; Hammond, A. T.; Sengupta, P.; Hess, S. T.; Holowka, D. A.; Baird, B. A.; Webb, W. W. Large-Scale Fluid/fluid Phase Separation of Proteins and Lipids in Giant Plasma Membrane Vesicles. *Proc. Natl. Acad. Sci.* **2007**, *104* (9), 3165–3170.

(23) Hammond, A. T.; Heberle, F. A.; Baumgart, T.; Holowka, D.; Baird, B.; Feigenson, G. W. Crosslinking a Lipid Raft Component Triggers Liquid Ordered-Liquid Disordered Phase Separation in Model Plasma Membranes. *Proc. Natl. Acad. Sci. U. S. A.* **2005**, *102* (18), 6320–6325.

(24) van Meer, G. Invisible Rafts at Work. *Traffic* **2004**, *5* (4), 211–212.

(25) Munro, S. Lipid Rafts: Elusive or Illusive? *Cell*. November 2003, pp 377–388.

(26) Lingwood, D.; Simons, K. Lipid Rafts As a Membrane-Organizing Principle. *Science* **2010**, *327* (5961), 46–50.

(27) Veatch, S. L.; Cicuta, P.; Sengupta, P.; Honerkamp-Smith, A.; Holowka, D.; Baird, B. Critical Fluctuations in Plasma Membrane Vesicles. *ACS Chem. Biol.* **2008**, *3* (5), 287–293.

(28) Marsh, D. Liquid-Ordered Phases Induced by Cholesterol: A Compendium of Binary Phase Diagrams. *Biochim. Biophys. Acta* **2010**, *1798* (3), 688–699.

(29) van Meer, G.; Voelker, D. R.; Feigenson, G. W. Membrane Lipids: Where They Are and How They Behave. *Nat. Rev. Mol. Cell Biol.* **2008**, *9* (2), 112–124.

(30) Feigenson, G. W.; Buboltz, J. T. Ternary Phase Diagram of Dipalmitoyl-

PC/dilauroyl-PC/cholesterol: Nanoscopic Domain Formation Driven by Cholesterol. *Biophys. J.* **2001**, *80* (6), 2775–2788.

(31) Capelluto, D. G. S. *Lipid-Mediated Protein Signaling*; Capelluto, D. G. S., Ed.; Advances in Experimental Medicine and Biology; Springer Netherlands: Dordrecht, 2013; Vol. 991.

(32) Contreras, F.-X.; Ernst, A. M.; Wieland, F.; Brügger, B. Specificity of Intramembrane Protein-Lipid Interactions. *Cold Spring Harb. Perspect. Biol.* **2011**, *3* (6), 1–18.

(33) Costa-Filho, A. J.; Crepeau, R. H.; Borbat, P. P.; Ge, M.; Freed, J. H. Lipid-Gramicidin Interactions: Dynamic Structure of the Boundary Lipid by 2D-ELDOR. *Biophys. J.* **2003**, *84* (5), 3364–3378.

(34) Holowka, D.; Baird, B. Nanodomains in Early and Later Phases of FcεRI Signalling. *Essays Biochem.* **2015**, *57*, 147–163.

(35) Marsh, D. Lipid-Protein Interactions in Membranes. *FEBS Lett.* **1990**, *268* (2), 371–375.

(36) Marsh, D. Electron Spin Resonance in Membrane Research: Protein-Lipid Interactions from Challenging Beginnings to State of the Art. *Eur. Biophys. J.* **2010**, *39* (4), 513–525.

(37) Smirnova, T. I.; Smirnov, A. I. High-Field ESR Spectroscopy in Membrane and Protein Biophysics. In *ESR Spectroscopy in Membrane Biophysics*; Springer US: Boston, MA; pp 165–251.

(38) Mainali, L.; Hyde, J. S.; Subczynski, W. K. Using Spin-Label W-Band EPR to Study Membrane Fluidity Profiles in Samples of Small Volume. *J. Magn. Reson.* **2013**, *226*, 35–44.

(39) Chiang, Y.-W.; Costa-Filho, A. J.; Freed, J. H. Two-Dimensional ELDOR in the Study of Model and Biological Membranes. *Appl. Magn. Reson.* **2007**, *31* (3–4), 375–386.

(40) Chiang, Y. W.; Costa-Filho, A. J.; Freed, J. H. Dynamic Molecular Structure and

Phase Diagram of DPPC-Cholesterol Binary Mixtures: A 2D-ELDOR Study. *J. Phys. Chem. B* **2007**, *111* (38), 11260–11270.

(41) Ge, M.; Freed, J. H. Hydration, Structure, and Molecular Interactions in the Headgroup Region of Dioleoylphosphatidylcholine Bilayers: An Electron Spin Resonance Study. *Biophys. J.* **2003**, *85* (6), 4023–4040.

(42) Subczynski, W. K.; Hyde, J. S.; Kusumi, A. Oxygen Permeability of Phosphatidylcholine--Cholesterol Membranes. *Proc. Natl. Acad. Sci.* **1989**, *86* (12), 4474–4478.

(43) Dzikovski, B. G.; Livshits, V. a; Marsh, D. Oxygen Permeation Profile in Lipid Membranes: Comparison with Transmembrane Polarity Profile. *Biophys. J.* **2003**, *85* (2), 1005–1012.

(44) Subczynski, W. K.; Lomnicka, M.; Hyde, J. S. Permeability of Nitric Oxide through Lipid Bilayer Membranes. *Free Radic. Res.* **2009**, *24* (5), 343–349.

(45) Polnaszek, C. F.; Schreier, S.; Butler, K. W.; Smith, I. C. P. Analysis of the Factors Determining the EPR Spectra of Spin Probes That Partition between Aqueous and Lipid Phases. *J. Am. Chem. Soc.* **1978**, *100* (26), 8223–8232.

(46) Ge, M.; Freed, J. H. Polarity Profiles in Oriented and Dispersed Phosphatidylcholine Bilayers Are Different: An Electron Spin Resonance Study. *Biophys. J.* **1998**, *74* (2), 910–917.

(47) Dzikovski, B.; Freed, J. Spin Labels in the Gel Phase and Frozen Lipid Bilayers : Do TheyTruly Manifest a Polarity Gradient? In *Nitroxides - Theory, Experiment and Applications*; InTech, 2012; pp 167–190.

(48) Dzikovski, B.; Livshits, V.; Freed, J. Interaction of Spin-Labeled Lipid Membranes with Transition Metal Ions. *J. Phys. Chem. B* **2015**, *119* (42), 13330–13346.

(49) Livshits, V. a; Dzikovski, B. G.; Marsh, D. Mechanism of Relaxation Enhancement of Spin Labels in Membranes by Paramagnetic Ion Salts: Dependence on 3d and 4f Ions and on the Anions. *J. Magn. Reson.* **2001**, *148* (2), 221–237.

(50) Smith, A. K.; Freed, J. H. Determination of Tie-Line Fields for Coexisting Lipid Phases: An ESR Study. *J. Phys. Chem. B* **2009**, *113* (12), 3957–3971.

(51) Chiang, Y.-W.; Zhao, J.; Wu, J.; Shimoyama, Y.; Freed, J. H.; Feigenson, G. W. New Method for Determining Tie-Lines in Coexisting Membrane Phases Using Spin-Label ESR. *Biochim. Biophys. Acta* **2005**, *1668* (1), 99–105.

(52) Smith, A. K.; Freed, J. H. Dynamics and Ordering of Lipid Spin-Labels along the Coexistence Curve of Two Membrane Phases: An ESR Study. *Chem. Phys. Lipids* **2012**, *165* (3), 348–361.

(53) Ge, M.; Freed, J. H. Electron-Spin Resonance Study of Aggregation of Gramicidin in Dipalmitoylphosphatidylcholine Bilayers and Hydrophobic Mismatch. *Biophys. J.* **1999**, *76* (1), 264–280.

(54) Dzikovski, B. G.; Borbat, P. P.; Freed, J. H. Spin-Labeled Gramicidin A: Channel Formation and Dissociation. *Biophys. J.* **2004**, *87* (5), 3504–3517.

(55) Lai, A. L.; Freed, J. H. HIV gp41 Fusion Peptide Increases Membrane Ordering in a Cholesterol-Dependent Fashion. *Biophys. J.* **2014**, *106* (1), 172–181.

(56) Ge, M.; Freed, J. H. Two Conserved Residues Are Important for Inducing Highly Ordered Membrane Domains by the Transmembrane Domain of Influenza Hemagglutinin. *Biophys. J.* **2011**, *100* (1), 90–97.

(57) Lai, A. L.; Freed, J. H. The Interaction between Influenza HA Fusion Peptide and Transmembrane Domain Affects Membrane Structure. *Biophys. J.* **2015**, *109* (12), 2523–2536.

(58) Banham, J. E.; Timmel, C. R.; Abbott, R. J. M.; Lea, S. M.; Jeschke, G. The Characterization of Weak Protein-Protein Interactions: Evidence from DEER for the Trimerization of a von Willebrand Factor A Domain in Solution. *Angew. Chemie - Int. Ed.* **2006**, *45* (7), 1058–1061.

(59) Schiemann, O.; Prisner, T. F. Long-Range Distance Determinations in Biomacromolecules by EPR Spectroscopy. *Q. Rev. Biophys.* **2007**, *40* (1), 1–53.

(60) Borbat, P. P.; Freed, J. H. Measuring Distances by Pulsed Dipolar ESR

Spectroscopy: Spin-Labeled Histidine Kinases. *Methods Enzymol.* **2007**, *423*, 52–116.

(61) Park, S.-Y.; Borbat, P. P.; Gonzalez-Bonet, G.; Bhatnagar, J.; Pollard, A. M.; Freed, J. H.; Bilwes, A. M.; Crane, B. R. Reconstruction of the Chemotaxis Receptor-Kinase Assembly. *Nat. Struct. Mol. Biol.* **2006**, *13* (5), 400–407.

(62) Borbat, P. P.; Freed, J. H. Pulse Dipolar Electron Spin Resonance: Distance Measurements. In *Structure and Bonding*; Timmel, C. R., Harmer, J. R., Eds.; Structure and Bonding; Springer Berlin Heidelberg, 2013; Vol. 152, pp 1–82.

(63) Martin, R. E.; Pannier, M.; Diederich, F.; Gramlich, V.; Hubrich, M.; Spiess, H. W. Determination of End-to-End Distances in a Series of TEMPO Diradicals of up to 2.8 Nm Length with a New Four-Pulse Double Electron Electron Resonance Experiment. *Angew. Chemie Int. Ed.* **1998**, *37* (20), 2833–2837.

(64) Pannier, M.; Veit, S.; Godt, A.; Jeschke, G.; Spiess, H. W. Dead-Time Free Measurement of Dipole-Dipole Interactions between Electron Spins. *J. Magn. Reson.* **2000**, *142* (2), 331–340.

(65) Borbat, P. P.; Freed, J. H. Multiple-Quantum ESR and Distance Measurements. *Chem. Phys. Lett.* **1999**, *313* (1–2), 145–154.

(66) Borbat, P. P.; Freed, J. H. Double Quantum ESR and Distance Measurements. In *Biological Magnetic Resonance, Vol. 19, Distance Measurements in Biological systems by EPR*; Berliner, L. J., Eaton, G. R., Eaton, S. S., Eds.; Biological Magnetic Resonance; Academic Press: New York, 2000; Vol. 19, pp 383–459.

(67) Borbat, P. P.; Georgieva, E. R.; Freed, J. H. Improved Sensitivity for Long-Distance Measurements in Biomolecules: Five-Pulse Double Electron–Electron Resonance. *J. Phys. Chem. Lett.* **2013**, *4* (1), 170–175.

(68) Chiang, Y.-W.; Borbat, P. P.; Freed, J. H. The Determination of Pair Distance Distributions by Pulsed ESR Using Tikhonov Regularization. *J. Magn. Reson.* **2005**, *172* (2), 279–295.

(69) Jeschke, G.; Panek, G.; Godt, A.; Bender, A.; Paulsen, H. Data Analysis Procedures for Pulse ELDOR Measurements of Broad Distance Distributions.

Appl. Magn. Reson **2004**, *26* (1–2), 223–244.

(70) Chiang, Y.-W.; Borbat, P. P.; Freed, J. H. Maximum Entropy: A Complement to Tikhonov Regularization for Determination of Pair Distance Distributions by Pulsed ESR. *J. Magn. Reson.* **2005**, *177* (2), 184–196.

(71) Srivastava, M.; Georgieva, E. R.; Freed, J. H. A New Wavelet Denoising Method for Experimental Time-Domain Signals: Pulsed Dipolar Electron Spin Resonance. *J. Phys. Chem. A* **2017**, *121* (12), 2452–2465.

(72) Srivastava, M.; Freed, J. H. A New SVD Based Method to Determine Distance Distributions in Pulsed Dipolar Spectroscopy. *Prep.* **2017**.

(73) Altenbach, C.; Flitsch, S. L.; Khorana, H. G.; Hubbell, W. L. Structural Studies on Transmembrane Proteins. 2. Spin Labeling of Bacteriorhodopsin Mutants at Unique Cysteines. *Biochemistry* **1989**, *28* (19), 7806–7812.

(74) Bhatnagar, J.; Borbat, P. P.; Pollard, A. M.; Bilwes, A. M.; Freed, J. H.; Crane, B. R. Structure of the Ternary Complex Formed by a Chemotaxis Receptor Signaling Domain, the CheA Histidine Kinase, and the Coupling Protein CheW As Determined by Pulsed Dipolar ESR Spectroscopy. *Biochemistry* **2010**, *49* (18), 3824–3841.

(75) Samanta, D.; Borbat, P. P.; Dzikovski, B.; Freed, J. H.; Crane, B. R. Bacterial Chemoreceptor Dynamics Correlate with Activity State and Are Coupled over Long Distances. *Proc. Natl. Acad. Sci.* **2015**, *2* (10), 2455–2460.

(76) Georgieva, E. R.; Ramlall, T. F.; Borbat, P. P.; Freed, J. H.; Eliezer, D. Membrane-Bound α-Synuclein Forms an Extended Helix: Long-Distance Pulsed ESR Measurements Using Vesicles, Bicelles, and Rodlike Micelles. *J. Am. Chem. Soc.* **2008**, *130* (39), 12856–12857.

(77) Samanta, D.; Widom, J.; Borbat, P. P.; Freed, J. H.; Crane, B. R. Bacterial Energy Sensor Aer Modulates the Activity of the Chemotaxis Kinase CheA Based on the Redox State of the Flavin Cofactor. *J. Biol. Chem.* **2016**, *291* (50), 25809–25814.

(78) Joseph, B.; Sikora, A.; Bordignon, E.; Jeschke, G.; Cafiso, D. S.; Prisner, T. F. Distance Measurement on an Endogenous Membrane Transporter in E. Coli Cells

and Native Membranes Using EPR Spectroscopy. *Angew. Chem. Int. Ed. Engl.* **2015**, *54* (21), 6196–6199.

(79) Ge, M.; Budil, D. E.; Freed, J. H. An Electron Spin Resonance Study of Interactions between Phosphatidylcholine and Phosphatidylserine in Oriented Membranes. *Biophys. J.* **1994**, *66* (5), 1515–1521.

(80) Ge, M.; Budil, D. E.; Freed, J. H. ESR Studies of Spin-Labeled Membranes Aligned by Isopotential Spin-Dry Ultracentrifugation: Lipid-Protein Interactions. *Biophys. J.* **1994**, *67* (6), 2326–2344.

(81) Crepeau, R. H.; Saxena, S.; Lee, S.; Patyal, B.; Freed, J. H. Studies on Lipid Membranes by Two-Dimensional Fourier Transform ESR: Enhancement of Resolution to Ordering and Dynamics. *Biophys. J.* **1994**, *66* (5), 1489–1504.

(82) Earle, K. A.; Dzikovski, B.; Hofbauer, W.; Moscicki, J. K.; Freed, J. H. High-Frequency ESR at ACERT. *Magn. Reson. Chem.* **2005**, *43 Spec no*, S256-66.

(83) Hofbauer, W.; Earle, K. A.; Dunnam, C. R.; Moscicki, J. K.; Freed, J. H. High-Power 95 GHz Pulsed Electron Spin Resonance Spectrometer. *Rev. Sci. Instrum.* **2004**, *75* (5), 1194.

(84) Freed, J. H. New Technologies in Electron Spin Resonance. *Annu. Rev. Phys. Chem.* **2000**, *51* (1), 655–689.

(85) Gorcester, J.; Rananavare, S. B.; Freed, J. H. Two-Dimensional Electron–electron Double Resonance and Electron Spin–echo Study of Solute Dynamics in Smectics. *J. Chem. Phys.* **1989**, *90* (10), 5764.

(86) Gorcester, J.; Freed, J. H. Two-Dimensional Fourier-Transform Electron-Spin-Resonance Correlation Spectroscopy. *J. Chem. Phys.* **1988**, *88* (8), 4678–4693.

(87) Gorcester, J.; Millhauser, G. L.; Freed, J. H. Two-Dimensional Electron-Spin Resonance. In *Advances in Pulsed and Continuous Wave Electron Spin Resonance*; Kevan, L., Bowman, M. K., Eds.; Wiley: New York, 1990; pp 119–194.

(88) Gorcester, J.; Freed, J. H. Two-Dimensional Fourier Transform ESR Correlation

Spectroscopy. *J. Chem. Phys.* **1988**, *88* (8), 4678–4693.

(89) Patyal, B. R.; Crepeau, R. H.; Gamliel, D.; Freed, J. H. Two-Dimensional Fourier Transform ESR in the Slow-Motional and Rigid Limits: 2D-ELDOR. *Chem. Phys. Lett.* **1990**, *175* (5), 453–460.

(90) Lee, S.; Budil, D. E.; Freed, J. H. Theory of Two-Dimensional Fourier Transform Electron Spin Resonance for Ordered and Viscous Fluids. *J. Chem. Phys.* **1994**, *101* (7), 5529.

(91) Franck, J. M.; Elnaggar, S. Y.; Dunnam, C. R.; Freed, J. H.; Mattar, S. M. Broadband Pulse Spectroscopy at 95 GHz. *Prep.* **2017**.

(92) Chiang, Y.-W.; Costa-Filho, A.; Freed, J. H. 2D-ELDOR Using Full Sc− Fitting and Absorption Lineshapes. *J. Magn. Reson.* **2007**, *188* (2), 231–245.

(93) Gamliel, D.; Freed, J. H. Theory of Two-Dimensional ESR with Nuclear Modulation. *J. Magn. Reson.* **1990**, *89* (1), 60–93.

(94) Jeener, J.; Meier, B. H.; Bachmann, P.; Ernst, R. R. Investigation of Exchange Processes by Two-Dimensional NMR Spectroscopy. *J. Chem. Phys.* **1979**, *71* (11), 4546.

(95) Freed, J. H. Theory of Saturation and Double Resonance Effects in Electron Spin Resonance Spectra. II. Exchange vs. Dipolar Mechanisms. *J. Phys. Chem.* **1967**, *71* (1), 38–51.

(96) Budil, D. E.; Lee, S.; Saxena, S.; Freed, J. H. Nonlinear-Least-Squares Analysis of Slow-Motion EPR Spectra in One and Two Dimensions Using a Modified Levenberg–Marquardt Algorithm. *J. Magn. Reson. Ser. A* **1996**, *120* (2), 155–189.

(97) Freed, J. H. Electron Spin Resonance. *Annu. Rev. Phys. Chem.* **1972**, *23* (1), 265–310.

(98) Hyde, J. S.; Chien, J. C. W.; Freed, J. H. Electron–Electron Double Resonance of Free Radicals in Solution. *J. Chem. Phys.* **1968**, *48* (9), 4211–4226.

(99) Kleckner, I. R.; Foster, M. P. An Introduction to NMR-Based Approaches for Measuring Protein Dynamics. *Biochim. Biophys. Acta - Proteins Proteomics* **2011**, *1814* (8), 942–968.

(100) Ernst, Richard, R.; Bodenhausen, G.; Wokaun, A. *Principles of Nuclear Magnetic Resonance in One and Two Dimensions*; Oxford University Press, 1987.

(101) Dzikovski, B. *Sample Preparation for Quasioptical High-Field ESR*; 2012; Vol. 22.

(102) Schneider, D.; Freed, J. Calculating Slow Motional Magnetic Resonance Spectra. In *Spin Labeling SE - 1*; Berliner, L., Reuben, J., Eds.; Biological Magnetic Resonance; Springer US, 1989; Vol. 8, pp 1–76.

(103) Dzikovski, B.; Tipikin, D.; Freed, J. Conformational Distributions and Hydrogen Bonding in Gel and Frozen Lipid Bilayers: A High Frequency Spin-Label ESR Study. *J. Phys. Chem. B* **2012**, *116* (23), 6694–6706.

(104) Smirnov, A. I.; Smirnova, T. I.; Morse, P. D. Very High Frequency Electron Paramagnetic Resonance of 2,2,6,6-Tetramethyl-1-Piperidinyloxy in 1,2-Dipalmitoyl-Sn-Glycero-3-Phosphatidylcholine Liposomes: Partitioning and Molecular Dynamics. *Biophys. J.* **1995**, *68* (6), 2350–2360.

(105) Needham, D.; Evans, E. Structure and Mechanical Properties of Giant Lipid (DMPC) Vesicle Bilayers from 20.degree.C below to 10.degree.C above the Liquid Crystal-Crystalline Phase Transition at 24.degree.C. *Biochemistry* **1988**, *27* (21), 8261–8269.

(106) Wu, S. H. W.; McConnell, H. M. Phase Separations in Phospholipid Membranes. *Biochemistry* **1975**, *14* (4), 847–854.

(107) Severcan, F.; Cannistraro, S. Use of PDDTBN Spin Probe in Partition Studies of Lipid Membranes. *Chem. Phys. Lett.* **1988**, *153* (2–3), 263–267.

(108) Berclaz, T.; Geoffroy, M. Spin-Labeling Study of Phosphatidylcholine-Cardiolipin Binary Mixtures. *Biochemistry* **1984**, *23* (18), 4033–4037.

(109) Edidin, M. Rotational and Translational Diffusion in Membranes. *Annu. Rev. Biophys. Bioeng.* **1974**, *3* (1), 179–201.

(110) Gaede, H. C.; Gawrisch, K. Lateral Diffusion Rates of Lipid, Water, and a Hydrophobic Drug in a Multilamellar Liposome. *Biophys. J.* **2003**, *85* (3), 1734–1740.

(111) Subczynski, W. K.; Wojas, J.; Pezeshk, V.; Pezeshk, A. Partitioning and Localization of Spin-Labeled Amantadine in Lipid Bilayers: An EPR Study. *J. Pharm. Sci.* **1998**, *87* (10), 1249–1254.

(112) Pople, J. A.; Schneider, W. G.; Bernstein, H. J. *High-Resolution Nuclear Magnetic Resonance*; McGraw-Hill: New York, 1959.

(113) Leigh, J. S. Relaxation Times in Systems with Chemical Exchange: Some Exact Solutions. *J. Magn. Reson.* **1971**, *4* (3), 308–311.

(114) Bain, A. D. Chemical Exchange in NMR. *Prog. Nucl. Magn. Reson. Spectrosc.* **2003**, *43* (3–4), 63–103.

(115) Farrow, N. A.; Zhang, O.; Forman-Kay, J. D.; Kay, L. E. A Heteronuclear Correlation Experiment for Simultaneous Determination of 15N Longitudinal Decay and Chemical Exchange Rates of Systems in Slow Equilibrium. *J. Biomol. NMR* **1994**, *4* (5), 727–734.

(116) Palmer, A. G. Chemical Exchange in Biomacromolecules: Past, Present, and Future. *J. Magn. Reson.* **2014**, *241* (1), 3–17.

(117) Zheng, J.; Kwak, K.; Asbury, J.; Chen, X.; Piletic, I. R.; Fayer, M. D. Ultrafast Dynamics of Solute-Solvent Complexation Observed at Thermal Equilibrium in Real Time. *Science* **2005**, *309* (5739), 1338–1343.

(118) Subczynski, W. K.; Hyde, J. S. The Diffusion-Concentration Product of Oxygen in Lipid Bilayers Using the Spin-Label T1 Method. *Biochim. Biophys. Acta - Biomembr.* **1981**, *643* (2), 283–291.

(119) Freed, J. H. Theory of Saturation and Double Resonance in Electron Spin Resonance Spectra. VI. Saturation Recovery. *J. Phys. Chem.* **1974**, *78* (12),

1155–1167.

(120) Huisjen, M.; Hyde, J. S. Saturation Recovery Measurements of Electron Spin-lattice Relaxation Times of Free Radicals in Solution. *J. Chem. Phys.* **1974**, *60* (4), 1682–1683.

(121) Lai, C. S.; Froncisz, W.; Hopwood, L. E. An Evaluation of Paramagnetic Broadening Agents for Spin Probe Studies of Intact Mammalian Cells. *Biophys. J.* **1987**, *52* (4), 625–628.

(122) Battino, R.; Rettich, T. R.; Tominaga, T. The Solubility of Oxygen and Ozone in Liquids. *J. Phys. Chem. Ref. Data* **1983**, *12* (2), 163–178.

(123) Shchukarev, S. A.; Tolmacheva, T. A. Solubility of Oxygen in Ethanol-Water Mixtures. *J. Struct. Chem.* **1968**, *9*, 16–21.

(124) Ju, L.-K.; Ho, C. S. Oxygen Diffusion Coefficient and Solubility in N-Hexadecane. *Biotechnol. Bioeng.* **1989**, *34* (9), 1221–1224.

(125) Rols, J. L.; Condoret, J. S.; Fonade, C.; Goma, G. Mechanism of Enhanced Oxygen Transfer in Fermentation Using Emulsified Oxygen-Vectors. *Biotechnol. Bioeng.* **1990**, *35* (4), 427–435.

(126) Battino, R.; Evans, F. D.; Danforth, W. F. The Solubilities of Seven Gases in Olive Oil with Reference to Theories of Transport through the Cell Membrane. *J. Am. Oil Chem. Soc.* **1968**, *45* (12), 830–833.

(127) Subczynski, W. K.; Hyde, J. S. Diffusion of Oxygen in Water and Hydrocarbons Using an Electron Spin Resonance Spin-Label Technique. *Biophys. J.* **1984**, *45* (4), 743–748.

(128) Fischkoff, S.; Vanderkooi, J. M. Oxygen Diffusion in Biological and Artificial Membranes Determined by the Fluorochrome Pyrene. *J. Gen. Physiol.* **1975**, *65* (5), 663–676.

(129) Kusumi, A.; Subczynski, W. K.; Hyde, J. S. Oxygen Transport Parameter in Membranes as Deduced by Saturation Recovery Measurements of Spin-Lattice Relaxation Times of Spin Labels. *Proc. Natl. Acad. Sci.* **1982**, *79* (6), 1854–1858.

(130) Mayor, S.; Rao, M. Rafts: Scale-Dependent, Active Lipid Organization at the Cell Surface. *Traffic* **2004**, *5* (4), 231–240.

(131) Sengupta, P.; Baird, B.; Holowka, D. Lipid Rafts, Fluid/fluid Phase Separation, and Their Relevance to Plasma Membrane Structure and Function. *Semin. Cell Dev. Biol.* **2007**, *18* (5), 583–590.

(132) Hancock, J. F. Lipid Rafts: Contentious Only from Simplistic Standpoints. *Nat. Rev. Mol. Cell Biol.* **2006**, *7* (6), 456–462.

(133) Ge, M.; Field, K. A.; Aneja, R.; Holowka, D.; Baird, B.; Freed, J. H. Electron Spin Resonance Characterization of Liquid Ordered Phase of Detergent-Resistant Membranes from RBL-2H3 Cells. *Biophys. J.* **1999**, *77* (2), 925–933.

(134) Devaux, P. F.; Morris, R. Transmembrane Asymmetry and Lateral Domains in Biological Membranes. *Traffic*. April 2004, pp 241–246.

(135) Konyakhina, T. M.; Goh, S. L.; Amazon, J.; Heberle, F. A.; Wu, J.; Feigenson, G. W. Control of a Nanoscopic-to-Macroscopic Transition: Modulated Phases in Four-Component DSPC/DOPC/POPC/Chol Giant Unilamellar Vesicles. *Biophys. J.* **2011**, *101* (2), L8–L10.

(136) Goh, S. L.; Amazon, J. J.; Feigenson, G. W. Toward a Better Raft Model: Modulated Phases in the Four-Component Bilayer, DSPC/DOPC/POPC/CHOL. *Biophys. J.* **2013**, *104* (4), 853–862.

(137) Wang, S. Undergraduate Thesis: Experimental Observation of Boundary Phospholipids in Lipid Membranes and Their Order, Dynamics, and Quantity between Lo and Ld Domains, Cornell University, 2014.

(138) Heberle, F. A.; Petruzielo, R. S.; Pan, J.; Drazba, P.; Kučerka, N.; Standaert, R. F.; Feigenson, G. W.; Katsaras, J. Bilayer Thickness Mismatch Controls Domain Size in Model Membranes. *J. Am. Chem. Soc.* **2013**, *135* (18), 6853–6859.

(139) Smith, A. K. The Phase Behavior of a Model Plasma Membrane, 2010.

(140) Usery, R. D.; Enoki, T. A.; Wickramasinghe, S. P.; Weiner, M. D.; Tsai, W.; Kim, M. B.; Wang, S.; Torng, T. L.; Ackerman, D. G.; Heberle, F. A.; Katsaras,

J.; Feigenson, G. W. Line Tension Controls Liquid-Disordered + Liquid-Ordered Domain Size Transition in Lipid Bilayers. *Biophys. J.* **2017**, *112* (7), 1431–1443.

(141) Barnes, J. P. P.; Freed, J. H. H. Aqueous Sample Holders for High-Frequency Electron Spin Resonance. *Rev. Sci. Instrum.* **1997**, *68* (7), 2838–2846.

(142) Kaur, P.; Li, Y.; Cai, J.; Song, L. Selective Membrane Disruption Mechanism of an Antibacterial γ-AApeptide Defined by EPR Spectroscopy. *Biophys. J.* **2016**, *110* (8), 1789–1799.

(143) Klauda, J. B.; Roberts, M. F.; Redfield, A. G.; Brooks, B. R.; Pastor, R. W. Rotation of Lipids in Membranes: Molecular Dynamics Simulation, 31P Spin-Lattice Relaxation, and Rigid-Body Dynamics. *Biophys. J.* **2008**, *94* (8), 3074–3083.

(144) Huang, J.; Feigenson, G. W. A Microscopic Interaction Model of Maximum Solubility of Cholesterol in Lipid Bilayers. *Biophys. J.* **1999**, *76* (4), 2142–2157.

(145) Kuzmin, P. I.; Akimov, S. A.; Chizmadzhev, Y. A.; Zimmerberg, J.; Cohen, F. S. Line Tension and Interaction Energies of Membrane Rafts Calculated from Lipid Splay and Tilt. *Biophys. J.* **2005**, *88* (2), 1120–1133.

(146) Holowka, D.; Gosse, J. A.; Hammond, A. T.; Han, X.; Sengupta, P.; Smith, N. L.; Wagenknecht-Wiesner, A.; Wu, M.; Young, R. M.; Baird, B. Lipid Segregation and IgE Receptor Signaling: A Decade of Progress. *Biochim. Biophys. Acta - Mol. Cell Res.* **2005**, *1746* (3), 252–259.

(147) Ravetch, J. V; Kinet, J. P. Fc Receptors. *Annu. Rev. Immunol.* **1991**, *9*, 457–492.

(148) Veatch, S. L.; Chiang, E. N.; Sengupta, P.; Holowka, D. A.; Baird, B. A. Quantitative Nanoscale Analysis of IgE-FcεRI Clustering and Coupling to Early Signaling Proteins. *J. Phys. Chem. B* **2012**, *116* (23), 6923–6935.

(149) Shelby, S. A.; Veatch, S. L.; Holowka, D. A.; Baird, B. A. Functional Nanoscale Coupling of Lyn Kinase with IgE-Fc RI Is Restricted by the Actin Cytoskeleton in Early Antigen-Stimulated Signaling. *Mol. Biol. Cell* **2016**, *27* (22), 3645–3658.

(150) Young, R. M.; Zheng, X.; Holowka, D.; Baird, B. Reconstitution of Regulated Phosphorylation of Fc RI by a Lipid Raft-Excluded Protein-Tyrosine Phosphatase. *J. Biol. Chem.* **2005**, *280* (2), 1230–1235.

(151) Jacobson, K.; Mouritsen, O. G.; Anderson, R. G. W. Lipid Rafts: At a Crossroad between Cell Biology and Physics. *Nat. Cell Biol.* **2007**, *9* (1), 7–14.

(152) Huang, B. Super-Resolution Optical Microscopy: Multiple Choices. *Curr. Opin. Chem. Biol.* **2010**, *14* (1), 10–14.

(153) Shelby, S. A.; Holowka, D.; Baird, B.; Veatch, S. L. Distinct Stages of Stimulated Fcεri Receptor Clustering and Immobilization Are Identified through Superresolution Imaging. *Biophys. J.* **2013**, *105* (10), 2343–2354.

(154) Georgieva, E. R.; Roy, A. S.; Grigoryants, V. M.; Borbat, P. P.; Earle, K. a.; Scholes, C. P.; Freed, J. H. Effect of Freezing Conditions on Distances and Their Distributions Derived from Double Electron Electron Resonance (DEER): A Study of Doubly-Spin-Labeled T4 Lysozyme. *J. Magn. Reson.* **2012**, *216*, 69–77.

(155) Fleissner, M. R.; Bridges, M. D.; Brooks, E. K.; Cascio, D.; Kalai, T.; Hideg, K.; Hubbell, W. L. Structure and Dynamics of a Conformationally Constrained Nitroxide Side Chain and Applications in EPR Spectroscopy. *Proc. Natl. Acad. Sci.* **2011**, *108* (39), 16241–16246.

(156) Sheets, E. D.; Holowka, D.; Baird, B. Critical Role for Cholesterol in Lyn-Mediated Tyrosine Phosphorylation of FcepsilonRI and Their Association with Detergent-Resistant Membranes. *J. Cell Biol.* **1999**, *145* (4), 877–887.

(157) Chen, X.; Resh, M. D. Cholesterol Depletion from the Plasma Membrane Triggers Ligand-Independent Activation of the Epidermal Growth Factor Receptor. *J. Biol. Chem.* **2002**, *277* (51), 49631–49637.

(158) Kabouridis, P. S.; Janzen, J.; Magee, A. L.; Ley, S. C. Cholesterol Depletion Disrupts Lipid Rafts and Modulates the Activity of Multiple Signaling Pathways in T Lymphocytes. *Eur. J. Immunol.* **2000**, *30* (3), 954–963.

(159) Hao, M.; Mukherjee, S.; Maxfield, F. R. Cholesterol Depletion Induces Large

Scale Domain Segregation in Living Cell Membranes. *Proc. Natl. Acad. Sci. U. S. A.* **2001**, *98* (23), 13072–13077.

(160) Mahammad, S.; Parmryd, I. Cholesterol Depletion Using Methyl-β-Cyclodextrin. In *Methods in Membrane Lipids: Second Edition*; 2015; pp 91–102.

(161) Nishimura, S. Y.; Vrljic, M.; Klein, L. O.; McConnell, H. M.; Moerner, W. E. Cholesterol Depletion Induces Solid-like Regions in the Plasma Membrane. *Biophys. J.* **2006**, *90* (3), 927–938.

(162) Veatch, S. L.; Keller, S. L. Separation of Liquid Phases in Giant Vesicles of Ternary Mixtures of Phospholipids and Cholesterol. *Biophys. J.* **2003**, *85* (5), 3074–3083.

(163) Levental, I.; Byfield, F. J.; Chowdhury, P.; Gai, F.; Baumgart, T.; Janmey, P. A. Cholesterol-Dependent Phase Separation in Cell-Derived Giant Plasma-Membrane Vesicles. *Biochem. J.* **2009**, *424* (2), 163–167.

(164) Feigenson, G. W. Phase Behavior of Lipid Mixtures. *Nat. Chem. Biol.* **2006**, *2* (11), 560–563.

(165) Sil, D.; Lee, J. B.; Luo, D.; Holowka, D.; Baird, B. Trivalent Ligands with Rigid DNA Spacers Reveal Structural Requirements For IgE Receptor Signaling in RBL Mast Cells. *ACS Chem. Biol.* **2007**, *2* (10), 674–684.

(166) Srivastava, M.; Georgieva, E. R.; Freed, J. H. A New Wavelet Denoising Method for Experimental Time Domain Signals: Pulsed Dipolar ESR. *Prep.* **2017**.

(167) Zheng, Y.; Shopes, B.; Holowka, D.; Baird, B. Conformations of IgE Bound to Its Receptor Fc Epsilon RI and in Solution. *Biochemistry* **1991**, *30* (38), 9125–9132.

(168) Holowka, D.; Wilkes, M.; Stefan, C.; Baird, B. Roles for Ca 2+ Mobilization and Its Regulation in Mast Cell Functions: Recent Progress. *Biochem. Soc. Trans.* **2016**, *44* (2), 505–509.

(169) Pedersen, U. R.; Leidy, C.; Westh, P.; Peters, G. H. The Effect of Calcium on the

Properties of Charged Phospholipid Bilayers. *Biochim. Biophys. Acta - Biomembr.* **2006**, *1758* (5), 573–582.

(170) Feigenson, G. W. On the Nature of Calcium Ion Binding between Phosphatidylserine Lamellae. *Biochemistry* **1986**, *25* (19), 5819–5825.

(171) Monson, C. F.; Cong, X.; Robison, A. D.; Pace, H. P.; Liu, C.; Poyton, M. F.; Cremer, P. S. Phosphatidylserine Reversibly Binds Cu 2+ with Extremely High Affinity. *J. Am. Chem. Soc.* **2012**, *134* (18), 7773–7779.

(172) Davey, A. M.; Krise, K. M.; Sheets, E. D.; Heikal, A. A. Molecular Perspective of Antigen-Mediated Mast Cell Signaling. *J. Biol. Chem.* **2008**, *283* (11), 7117–7127.

(173) Wallace, B. A. Structure of Gramicidin A. *Biophys. J.* **1986**, *49* (1), 295–306.

(174) Shapovalov, V. L.; Kotova, E. A.; Rokitskaya, T. I.; Antonenko, Y. N. Effect of Gramicidin A on the Dipole Potential of Phospholipid Membranes. *Biophys. J.* **1999**, *77* (1), 299–305.

(175) Ge, M.; Freed, J. H. An Electron Spin Resonance Study of Interactions between Gramicidin A' and Phosphatidylcholine Bilayers. *Biophys. J.* **1993**, *65* (5), 2106–2123.

(176) Tanaka, H.; Freed, J. H. Electron Spin Resonance Studies of Lipid-Gramicidin Interactions Utilizing Oriented Multibilayers. *J. Phys. Chem.* **1985**, *89* (2), 350–360.

(177) Wylie, B. J.; Dzikovski, B. G.; Pawsey, S.; Caporini, M.; Rosay, M.; Freed, J. H.; McDermott, A. E. Dynamic Nuclear Polarization of Membrane Proteins: Covalently Bound Spin-Labels at Protein-Protein Interfaces. *J. Biomol. NMR* **2015**, *61* (3–4), 361–367.

(178) Livnah, O.; Bayer, E. a; Wilchek, M.; Sussman, J. L. Three-Dimensional Structures of Avidin and the Avidin-Biotin Complex. *Proc. Natl. Acad. Sci. U. S. A.* **1993**, *90* (11), 5076–5080.

(179) Wilchek, M.; Bayer, E. A. The Avidin-Biotin Complex in Bioanalytical

Applications. *Anal. Biochem.* **1988**, *171* (1), 1–32.

(180) Strzelczyk, P.; Plazuk, D.; Zakrzewski, J.; Bujacz, G. Structural Characterization of the Avidin Interactions with Fluorescent Pyrene-Conjugates: 1-Biotinylpyrene and 1-Desthiobiotinylpyrene. *Molecules* **2016**, *21* (10), 1270.

(181) Amspacher, D. R.; Blanchard, C. Z.; Fronczek, F. R.; Saraiva, M. C.; Waldrop, G. L.; Strongin, R. M. Synthesis of a Reaction Intermediate Analogue of Biotin-Dependent Carboxylases via a Selective Derivatization of Biotin. *Org. Lett.* **1999**, *1* (1), 99–102.

(182) Neises, B.; Steglich, W. Simple Method for the Esterification of Carboxylic Acids. *Angew. Chemie Int. Ed.* **1978**, *17* (7), 522–524.